IMAGE: A MAP OF THE STARS OF THE ORION CONSTELLATION

JournalPreview

London Journal of Engineering Research

Volume 24 | Issue 7 | Compilation 1.0

Great Britain Journals Press

WWW.JOURNALSPRESS.COM

Journal Content
In this Issue

Great Britain Journals Press

Enhancing Compressed Earth Blocks with Eggshell and Lime: Effects on Mechanical and Physical Properties

Aaron Tony Turkson, Humphrey Danso & Emmanuel Appiah-Kubi

Akenten Appiah-Menka University of Skills Training and Entrepreneurial Development

ABSTRACT

The use of eggshells in building materials has gained interest due to its prospect of enhancing the mechanical properties of concrete and its role as an eco-friendly alternative to traditional materials. Combining waste crushed eggshells and lime in earth blocks has the potential to inform the development of affordable and eco-friendly housing solutions for low-income communities. This study, therefore, examined the mechanical and physical properties of compressed earth blocks (CEBs) stabilised with eggshells and lime. Experiments were conducted on 140 × 100 x 100 mm earth blocks stabilised with 10% constant lime and 0, 0.25, 0.5, 0.75, 1% eggshell contents. CEBs were tested for density, water absorption, tensile strength, compressive strength, erosion, chemical composition, and microstructural on 7, 14, 21, and 28 curing days. At 28 days of curing, the 1% eggshell and 10% lime-stabilised compressed earth blocks recorded compressive strength of 1.331 N/mm2 compared with the unstabilised compressed earth blocks' strength of 1.054 N/mm2, which represents a 21% increase in compressive strength, and the difference was found be statistically significant (p = 0.016).

Keywords: compressive strength, compressed earth blocks (CEBs), eggshell waste, lime, mechanical properties, tensile strength, water absorption, sustainability, stabilization, micros- tructural analysis.

Classification: DDC Code: 620.1

Language: English

Great Britain Journals Press

LJP Copyright ID: 392952
Print ISSN: 2631-8474
Online ISSN: 2631-8482

London Journal of Engineering Research

Volume 24 | Issue 7 | Compilation 1.0

Enhancing Compressed Earth Blocks with Eggshell and Lime: Effects on Mechanical and Physical Properties

Aaron Tony Turkson[α], Humphrey Danso[σ] & Emmanuel Appiah-Kubi[ρ]

ABSTRACT

The use of eggshells in building materials has gained interest due to its prospect of enhancing the mechanical properties of concrete and its role as an eco-friendly alternative to traditional materials. Combining waste crushed eggshells and lime in earth blocks has the potential to inform the development of affordable and eco-friendly housing solutions for low-income communities. This study, therefore, examined the mechanical and physical properties of compressed earth blocks (CEBs) stabilised with eggshells and lime. Experiments were conducted on 140 × 100 x 100 mm earth blocks stabilised with 10% constant lime and 0, 0.25, 0.5, 0.75, 1% eggshell contents. CEBs were tested for density, water absorption, tensile strength, compressive strength, erosion, chemical composition, and microstructural on 7, 14, 21, and 28 curing days. At 28 days of curing, the 1% eggshell and 10% lime-stabilised compressed earth blocks recorded compressive strength of 1.331 N/mm² compared with the unstabilised compressed earth blocks' strength of 1.054 N/mm², which represents a 21% increase in compressive strength, and the difference was found be statistically significant (p = 0.016). At 28 days of curing, the 1% eggshell and 10% lime-stabilised compressed earth blocks' tensile strength was 0.173 N/mm² compared with the unstabilised compressed earth blocks' strength of 0.138 N/mm², which represents a 20% tensile strength increase. The eggshell and lime-stabilised compressed earth blocks also exhibited reduced water absorption of 3.32% compared to unstabilised blocks of 4.62%. SEM analysis revealed the earth particle structure, lime particle crystal shape, crack distribution, and surface properties of the CEBs. EDS analyses further confirmed the presence of key elements like iron, titanium, calcium, silicon, aluminium, oxygen, and carbon in the CEBs. The study concludes that the presence of eggshells and lime in the earth matrix enhanced the properties of the compressed earth blocks. It is recommended that block manufacturers use 1% eggshell and 10% lime to enhance the properties of the compressed earth blocks as this blend provided optimum results.

Keywords: compressive strength, compressed earth blocks (CEBs), eggshell waste, lime, mechanical properties, tensile strength, water absorption, sustainability, stabilization, micros-tructural analysis.

Author α: Department of Construction Technology and Management Education Akenten Appiah-Menka University of Skills Training and Entrepreneurial Development, Kumasi-Ghana. Department of Construction Technology and Management Cape Coast Technical University Cape Coast – Ghana.
σ ρ: Department of Architecture and Civil Engineering Akenten Appiah-Menka University of Skills Training and Entrepreneurial Development, Kumasi- Ghana.

I. INTRODUCTION

Affordable housing is a critical issue in developing countries, where land and construction costs surpass the financial means of many citizens [1]. Adopting alternative and cost-effective construction methods is necessary to address the affordable housing issue. One promising approach is utilizing readily available, eco-friendly materials like compressed earth blocks [2,3]. Compressed earth blocks (CEBs) are building blocks that are produced by compacting soil/earth in an electrical or hydraulic block-making machine, in which a control static or dynamic pressure is applied [4,5]. CEBs are not only cost-effective but also

environmentally friendly, as they do not require the burning of coal or other fuels in their production, unlike conventional fire-burnt clay bricks [3]. CEBs are also aligned with green building principles because they can be sourced on-site, and minimise transportation costs [6-8]. Additionally, the thermal mass of earth-based materials helps regulate indoor temperature, reducing reliance on energy-intensive heating and cooling systems [9-11].

CEBs offer a sustainable alternative to conventional building materials, yet their vulnerability to water-induced erosion poses a significant challenge, particularly in regions with heavy rainfall and high humidity [12]. While studies show that adding natural fibres can improve their water resistance, they are not a perfect solution [12, 13]. Current research on stabilizing earth blocks explores various materials including rice husk ash, fly ash, and cement [14-18]. While cement is effective, it is expensive and not environmentally friendly [19]. Although several studies have used waste and binders to stabilize CEBs, as far as the researchers are concerned, no study has used eggshell waste and lime to stabilize CEBs. There is a gap in the research on using crushed eggshells and lime as stabilisers for CEBs, which requires a study to explore the potential of using crushed eggshells and lime in building materials for construction applications. This study, therefore, explores the potential of using crushed eggshells and lime as stabilisers for CEBs. Eggshells, a common industrial and household waste, are rich in calcium, a valuable element for enhancing the strength and durability of construction materials [20, 21]. Lime, another eco-friendly binder, further contributes to improved performance.

This approach aligns with the goals of sustainable construction by utilizing waste materials and minimizing environmental impact. By investigating the properties of CEBs stabilised with eggshells and lime, this study aims to address the critical need for improved durability and strength in sustainable construction materials. The use of eggshells and lime in CEBs is expected to overcome the limitations such as water-induced erosion, and strength deficiencies in the use of natural fibres in CEBs. Through comprehensive laboratory testing, the study specifically examines the physical properties (density and water absorption) of CEBs stabilised with eggshells and lime; mechanical properties (compressive and tensile strengths) of CEBs stabilised with eggshells and lime; durability properties (erosion resistance) of CEBs stabilised with eggshells and lime; and microstructural and chemical composition (SEM and EDS) of CEBs stabilised with eggshells and lime. The findings have the potential to inform the development of affordable and eco-friendly housing solutions for low-income communities, paving the way for a more sustainable construction industry.

II. LITERATURE REVIEW

2.1 Benefits of Building Houses with Earth

Earth construction is one of the oldest building techniques known to humanity, with a history that spans thousands of years and encompasses a variety of methods adapted to different environmental and climatic conditions [22]. Techniques such as rammed earth and adobe have been integral to vernacular architecture, reflecting a harmonious coexistence between human settlements and the natural environment [23]. Rammed earth, for instance, involves the compaction of natural mineral soils in layers within formwork, creating structures that are durable and have a low environmental impact [24]. The adaptability of earth construction is evident in its global presence, from the Neolithic architecture sites to modern buildings that incorporate green technologies [24]. This adaptability is also highlighted by the diversity of materials and techniques used in different regions, such as cob, sod, thatch, bamboo, and straw bales, each with its characteristics and suitability to specific climates and locales [23].

The ancient methods of earthen construction have evolved to the modern sustainable practices and techniques. In contemporary times, the significance of earth construction has been reinvigorated by the sustainable development movement, which values the use of natural and recycled resources [25, 26]. The low embodied energy of materials like rammed earth, when

compared to conventional construction materials, and the potential for these materials to be wholly recyclable, contribute to their eco-efficiency and appeal in the context of sustainable development [27].

Furthermore, the cultural heritage of earth construction is being preserved and studied not only for its historical value but also for its relevance to modern sustainable building practices [28]. The renewed interest in earth construction is driven by its environmental benefits, such as the use of local materials, low energy requirements for production, and recyclability, as well as its thermal and hygroscopic properties [27]. Earth construction embodies a rich history of human ingenuity and environmental stewardship. Its resurgence in the context of sustainable architecture demonstrates a continued appreciation for its cultural significance and a recognition of its potential to contribute to eco-friendly building practices in the 21st century [29].

2.2 Earth Construction Techniques

There are several techniques for earth construction such as rammed earth (RE), compressed earth blocks (CEBs), adobe blocks, cob, Atakpame, wattle and daub among others. RE is a construction technique that involves the dynamic compaction of soil within temporary forms to create monolithic walls, which are structurally sound and have good thermal mass [30, 31]. CEBs are made by mechanically pressing soil particles into a mould, producing a uniform shape and size for construction purposes, and can be stabilised with a small number of binders or fibres to improve their properties [32]. Adobe blocks are a traditional form of earth construction, where clayey soil is mixed with organic matter, often dung, to enhance bonding and reduce shrinkage, then moulded and dried in the sun [33].

Cob construction is an ancient technique that uses a mixture of earth and straw, similar to adobe, but the material is stacked and lightly compacted by hand or tools to form walls [34]. The Atakpame technique employs threads and pegs to create rectangular walls by methodically applying mud balls, though this technique is less documented in the provided papers. Wattle and daub is a method where woven wooden strands, known as "wattle," are covered with a mixture of soil and straw, known as "daub," to form walls that provide both structural support and insulation [35].

Each of these techniques has its own set of advantages and challenges. For instance, RE is known for its energy efficiency and thermal properties [30], while CEBs offer a cost-effective and sustainable building solution, especially in developing countries [32]. Adobe provides a traditional aesthetic and has been widely used historically, but may require more maintenance [33]. Cob is praised for its shear behaviour and flexibility under load [33], and wattle and daub are recognized for their high thermal insulation capacity [35]. These earth construction techniques offer sustainable alternatives to conventional building materials, with each having unique characteristics that make them suitable for different environmental conditions and cultural contexts. The choice of a particular technique can be influenced by factors such as local soil properties, climate, and the availability of natural fibres or stabilisers. Table 1 provides summary information about the process and characteristics of earth construction techniques.

Table 1: Process and characteristics of earth construction techniques

Earth construction technique	Process	Characteristics
Rammed Earth (RE)	Involves compacting a damp mixture of earth (often with stabilisers like cement or lime) into a formwork to create dense, sturdy walls.	Known for its thermal mass, durability, and unique aesthetic.
Compressed Earth Blocks (CEBs)	Made by compressing a mixture of soil, sand, and sometimes stabilisers into blocks using a hydraulic or mechanical press.	Strong, uniform, and can be produced quickly. They require less energy to produce compared to traditional bricks.
Adobe Blocks	Created by mixing earth (clay, sand, silt) with water and sometimes organic materials like straw. The mixture is then poured into molds and sun-dried.	Adobe bricks are known for their thermal properties and are often used in hot, dry climates.
Cob	Made by mixing earth (clay, sand, straw) and water to create a thick, malleable material that is hand-shaped into walls.	Cob structures are highly durable and have excellent thermal mass. They are also very labor-intensive to build.
Atakpame	A traditional West African technique involving the layering of moist earth mixed with organic materials like straw or palm fronds.	Known for its simplicity and use of locally available materials. It provides good thermal insulation.
Wattle and Daub	Involves weaving a lattice of wooden strips (wattle) and then daubing it with a sticky mixture of soil, clay, sand, and straw.	Provides good insulation and is often used for infill in timber-framed buildings.

2.3 Durability of Earth Construction

The durability of earth construction materials is a critical aspect of their performance, especially given their inherent susceptibility to water and other degrading agents. Earthen materials are known for their hygroscopic nature, which can lead to durability issues rather than strength concerns [36]. The exposure to water, through rain, floods, or capillary absorption, is a significant factor affecting the service life of earthen structures [37]. To address these concerns, it is essential to assess the durability of earthen materials based on their likely exposure to water and to specify tests that safeguard the construction and environmental conditions [36]. Research has shown that traditional and ancestral building techniques, such as the incorporation of biopolymers and the stabilization with lime, have contributed to the enhanced durability of earthen buildings [18]. These techniques have been used to protect the earth's material from water action, allowing old earthen buildings to be preserved over centuries despite harsh weather conditions [37]. Similarly, the addition of lime has been found to increase compressive strength and reduce erosion in accelerated erosion tests, suggesting its effectiveness in improving the water resistance of compressed soil [12, 37].

Contemporary studies have also explored the use of natural additives to improve the engineering properties of earthen-based composites. For instance, the incorporation of short sisal fibres and chitosan has been shown to have a significant influence on the strength and durability properties of earthen-based composites for 3D printing applications [37]. While the specific use of eggshells as an additive is not directly addressed in the provided studies, the general principle of using natural and eco-friendly additives to enhance the durability of earthen materials is supported by research. The durability

of earth construction materials can be significantly improved through the use of appropriate additives and techniques. The use of lime and biopolymers, as well as other natural additives, has been demonstrated to enhance the resistance of earthen materials to water and erosion, thereby extending their service life [18, 38, 39]. It is imperative to continue exploring and adapting these ancient and modern methods to ensure the longevity and sustainability of earth construction in the face of environmental challenges.

2.4 Eggshell Powder Development in Construction

The utilization of eggshell powder (ESP) in building materials has gained interest due to its prospect of enhancing the mechanical properties of concrete and its role as an eco-friendly alternative to traditional materials. Studies have indicated that incorporating ESP into concrete can lead to an increase in both compressive and flexural strength [40-44]. This improvement is attributed to the calcium oxide content in eggshells, which enhances the strength and durability of the concrete [43, 45]. Moreover, the addition of ESP has been shown to lessen the water absorption of concrete, suggesting an increase in density and impermeability [40, 41].

This reduction in porosity is beneficial for the longevity and structural integrity of concrete structures. The optimal replacement level of ordinary Portland cement with ESP is often cited as 15% by volume, which balances the benefits of added strength with the potential decrease in compressive strength at higher replacement levels [40, 42, 44].

In terms of environmental impact, the partial cement replacement with ESP in concrete production is a promising strategy for reducing carbon dioxide emissions associated with cement manufacturing [43, 45, 46]. This approach not only mitigates the environmental footprint of construction activities but also addresses waste management concerns by repurposing eggshell waste. Eggshells have not been explored for their soil stabilization properties. While the literature does not directly address this application, the calcium-rich composition of eggshells suggests potential benefits in improving soil plasticity and reducing shrinkage. The incorporation of eggshell in CEBs production presents a multifaceted advantage, enhancing the strength properties of the blocks while offering a sustainable solution to environmental challenges in the construction industry. However, further research into the soil stabilization properties of eggshells would be beneficial to fully understand their potential in this domain [43, 46].

Eggshells can have a positive impact on the physical, mechanical, and thermal properties of CEBs. Eggshell powder has been found to increase the compressive strength, hardness, and thermal insulation properties of CEBs [47]. Additionally, eggshell ash has been shown to improve the durability of sandcrete blocks against water and weathering [48]. A study on the utilization of various agricultural wastes, including eggshell powder, sawdust powder, and rice husk ash, found that eggshell powder improved the physico-mechanical and durability properties of CEBs [49]. Another study reviewed the influence of eggshell powder on the mechanical properties of expansive soil and found that it improved compressive strength and reduced the soil's swelling potential [47]. Furthermore, a study evaluated the mechanical and microstructural properties of eggshell powder-reinforced concrete and found that it improved the compressive strength and reduced the porosity of the concrete [32]. These findings suggest that eggshells can be a valuable additive in CEB production to improve their physical, mechanical, and thermal properties and enhance their durability.

III. EXPERIMENTAL MATERIALS AND METHODS

3.1 Materials

Earth, waste crushed eggshell, lime, and water were the primary materials used for making the CEBs' specimens used in this study. The earth sample was conveniently sourced from a site at the Akenten Appiah-Menka University of Skills Training and Entrepreneurial Development

(AAMUSTED), Kumasi campus, Ghana. The topsoil was scraped off, and the earth was dug out. The earth was packed into sacks and transported from the site to the Construction Laboratory of AAMUSTED. The earth sample (Fig. 1a) was sun-dried at an average temperature of 27 °C and relative humidity of 72% for two weeks and was sieved through a 19 mm sieve filter to ensure the removal of cobblers and stones before the grading test was conducted, which conformed to BS 1377 [50]. Larger sizes of cobblers and stones in the earth can affect the composition of the CEBs, which will result in the formation of weaker composite materials.

The waste eggshells, the reinforcing material used, were conveniently obtained from the abundant deposits of fried and poached egg vendors in Cape Coast, Ghana. Raw eggshells were boiled, air-dried, and then added to the prepared eggshells, and were sun-dried at an average temperature of 27 °C and relative humidity of 72%. Subsequently, the dried eggshells were crushed and sieved through a BS 14 mm sieve (Fig. 1b).

Calcium hydroxide ($Ca(OH)_2$) lime with 95% CaO was conveniently obtained from the market at Kumasi, Ghana. The hydrated lime sample used is shown in Fig. 1c. Danso and Manu [39] and Karthik and Ramachandraiah [51] identified that the addition of 10% lime to laterite soil considerably increases compressive strength and durability. Water for mixing was obtained directly from the tap in the Construction Laboratory of AAMUSTED, where the experiment was performed. Tap water used was for drinking purposes with a pH value of 6.8.

Fig. 1: Sample raw materials: (a) earth sample, (b) crushed eggshell samples, (c) lime sample

3.2 Experimental Procedure

The crushed eggshells of 0, 0.25, 0.5, 0.75, and 1% by weight of earth and 10% constant lime were added to the earth sample for making the CEBs. The mix design and quantity of materials are presented in Table 2. The required quantity of earth was batched and spread on the mixing pan. The quantity of lime was batched and spread over the earth and was manually mixed thoroughly after which the crushed eggshells were also batched, spread on the earth-lime mixture, and mixed. Water at an optimum moisture content (OMC) of 12% of the weight of the earth was gradually spread on the mixture while mixing until a reasonable uniform consistency was obtained as shown in Fig. 2a. The control mixture was prepared with earth and water without lime and eggshells as was in the study by Danso and Manu [39]. The different mix batches were used to prepare a total of 150 blocks of size 140 × 100 × 100 mm which were moulded with a compressed block-making machine (see Fig. 2b) with 50 kPa compressed pressure. The blocks were kept under a shed and cured by sprinkling water daily (see Fig. 2c) at an average temperature of 27 °C and relative humidity of 72%. Three block replicates were tested on 7, 14, 21, and 28 days for each mix design and curing day for their properties to be determined.

Table 2: Mix design and quantity of materials

Mix design (%)	Quantity of materials (kg)			
	Earth	Eggshell	Lime	Water
0	75.6	-	-	9.072
0.25	75.6	0.189	7.56	9.072
0.5	75.6	0.378	7.56	9.072
0.75	75.6	0.567	7.56	9.072
1	75.6	0.756	7.56	9.072

Fig. 2: Preparation of CEBs: (a) mixing of mortar, (b) moulding of blocks, (c) curing of blocks

3.3 Testing of CEB Specimens

Compressive strength, density, tensile strength, erosion, and water absorption tests were performed to assess the properties of the CEBs. Five replicates were used for each test from each mix batch.

3.3.1 Compressive Strength

The compressive strength test was conducted following the BS EN 772-1 [52] procedure. 60 CEB specimens were tested for the compressive strength. The electrically controlled ADR 4000 compressive strength machine was used for testing the CEB specimens. To maintain consistent loading, CEB specimens were aligned centrally at the test as shown in Fig. 3a. The load was gradually applied until the CEB specimens were crushed. The highest force at which the CEB specimens were crushed was noted and the strength was calculated using Equation 1:

$$fc = \frac{F}{A} \quad \text{.....Equation (1)}$$

where fc = compressive strength in N/mm²; F = highest force at which the CEB specimens crushed in N; A = area of the CEB specimens where the force was applied in mm².

Fig. 3: Testing of CEB specimens: (a) compressive strength, (b) tensile strength, (c) erosion test

3.3.2 Tensile Strength

The tensile strength test was conducted adhering to BS EN 12390-6 [53] procedure. 60 CEB specimens were tested for the tensile strength. The electrically controlled ADR 4000 testing machine was used to test the CEB specimens as shown in Fig. 3b. The CEB specimens were placed on a jig plate on the testing machine, ensuring no bending or twisting occurred. The test machine applied a controlled force on the CEB specimens until it was divided into two. The highest force at which the CEB specimens were divided into two

was noted and the strength was calculated using Equation 2:

$$ft = \frac{2P}{\pi Ld} \quad \text{.....Equation} \quad (2)$$

where ft = tensile strength in N/mm²; P = the highest force where the CEB specimens divided into two in N; L = length of the CEB specimens in mm; and d = width of the CEB specimens in mm.

3.3.3 Erosion Resistance

The drip test method was used to determine the erosion resistance of the 28-day-cured CEB specimens following the procedure of NZS 4298 [54]. 15 CEB specimens were tested for the erosion resistance. The drip test setup was positioned and the CEB specimens were placed at the base at 27° as shown in Fig. 3b. The absorbent Wettex of 16 mm diameter served as a drip to drop the water at a distance of 400 mm onto the slopped CEB specimens for 60 minutes. After 60 minutes, the depth of the pit created in the CEB specimens was measured and the erodability index was determined.

3.3.4 Water Absorption

A water absorption test was carried out on 28-day-cured CEB specimens following the procedure of BS EN 772-11 [55]. 15 CEB specimens were tested for the water absorption. The CEB specimens were oven-dried at 105 °C for overnight. An empty tray was placed on level ground with strips of plywood placed at the bottom. The CEB specimens were weighed and the weights were recorded. The CEB specimens were placed on the plywood strips in the tray and water was gently poured to 10 mm above the plywood strips. The CEB specimens were removed after 20 minutes, weighed and the partially absorbed weight was recorded. Water absorption of the CEB specimens was determined using Equation 3:

$$WA = \frac{M2-M1}{M1} \times 100 \quad \text{.....Equation} \quad (3)$$

where WA = is water absorption by capillary in %; M_1 = weight of the CEB specimens after oven-drying in kg; and M_2 = the weight of partially absorbed CEB specimens in kg.

3.3.5 Density

The density of the CEB specimens was assessed adhering to the BS EN 771-1 [56] procedure. The 45 CEB specimens used for the compressive strength test were first weighed to determine the density of the blocks. The CEB specimens were weighed and oven-dried at 105 °C for overnight. The dried CEBs were weighed and their volume was determined. The density of the CEB specimens was calculated using Equation 4:

$$\rho = \frac{M2-M1}{M1} \times 100 \quad \text{.....Equation} \quad (4)$$

where ρ = is water absorption by capillary in %; M_1 = weight of the CEB when oven-drying in kg; and M_2 = the weight of partially absorbed CEB specimens in kg.

3.3.5 Microscopic Morphology and Elemental Content Examination

A Zeiss scanned electron microscopy (SEM) was used to analyse the eggshells' microscopic morphology and elemental content of the CEB specimen. A CEB specimen was broken into pieces and prepared before the SEM examination. After preparation, it was placed on a holder in the Zeiss SEM machine for microscopic viewing and elemental composition measurement. The viewed images and the chemical elemental composition were captured and analysed.

3.3.6 Analysis of Data

The data obtained were computed and presented in figures and tables with the help of Microsoft Excel software. An ANOVA test was used to assess the significant variations and differences between the test results. To determine the existence of any significant difference in different test groups, Sigma Plot software was used.

IV. RESULTS AND DISCUSSION

The results obtained from the physical properties of earth and eggshell (particle size distribution

test, dry density, water absorption), mechanical properties (compressive and tensile strengths), durability properties (water absorption and erosion), and SEM and EDS analysis tests are presented in detail below.

4.1 Physical Properties

The particle size distribution curve of the lateritic soil and eggshells is illustrated in Fig. 4. The particle size distribution analysis of both eggshells and lateritic soil indicates that a significant portion of the particles are relatively large. For eggshells, 85.77% of the particles are larger than 5 mm as compared with lateritic soil, which is 61.68%. This suggests that both materials consist of coarse particles, with eggshells having a slightly finer distribution compared to lateritic soil. The inclusion of lime which has finer particles will compensate for the less quantities of earth and eggshell fine particles in the mix and also serve as additional binder.

Dry Density: Fig. 5 shows the density of the blocks which was measured throughout the 28-day curing period, with varying eggshell stabiliser concentrations. On day 7 of curing, the density ranged from 1677.949 to 1700.000 kg/m^3 exhibiting a minimal variation between stabiliser percentages. This suggests minimal impact from the eggshell stabiliser at this early curing stage. On day 14 of curing, density readings varied little. The range was 1671.538–1714.487 kg/m^3. Interestingly, the density rose with eggshell stabiliser content, peaking at 1%. On day 21 of curing, density ranged from 1692.667 to 1721.282 kg/m^3. The percentage of eggshell stabilisers increased the density as Zamani et al [57] found. The density ranged from 1704.615 to 1740.256 kg/m^3 on day 28 of curing. As eggshell and lime stabiliser content increased, density increased. These findings indicate that curing time and eggshell and lime stabiliser concentration affect material density. As curing time increased, the density either stabilised or increased slightly. Moreover, the addition of eggshells and lime consistently contributed to higher densities, particularly at later curing stages. The increasing density with higher eggshell and lime content, along with the continued rise or stabilisation in density with curing time, can be attributed to the filling effect and pozzolanic reaction. As the amount of eggshells and lime increases, more particles pack into the voids between the soil particles, leading to a denser matrix [47, 58]. Additionally, lime, a common stabiliser, undergoes a pozzolanic reaction with water, forming calcium silicate hydrate (CSH) gels that further densify the mixture over time [41, 58].

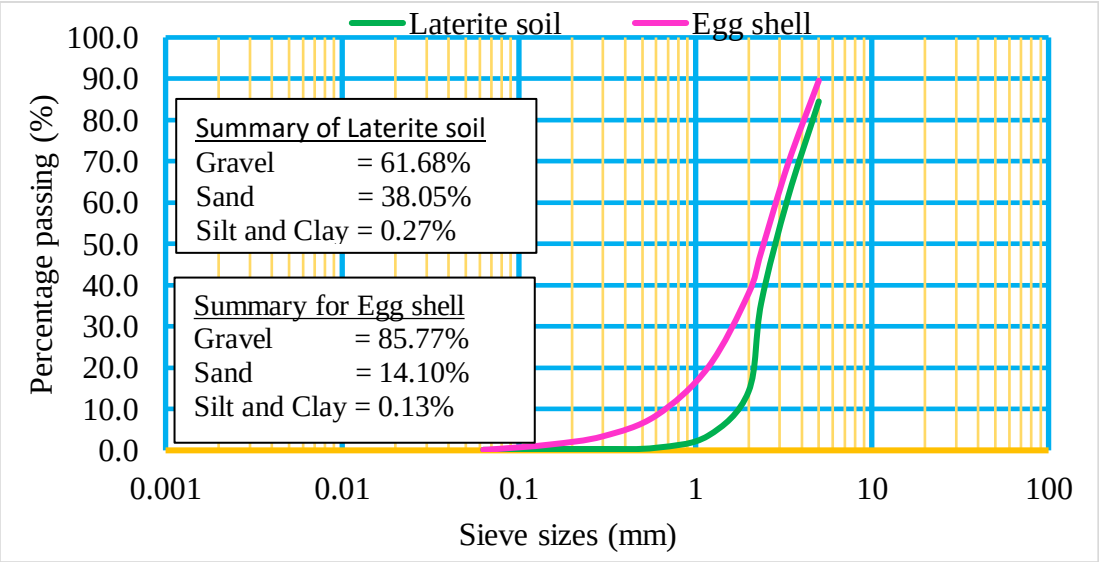

Fig. 4: Particle size distribution of both laterite and eggshell

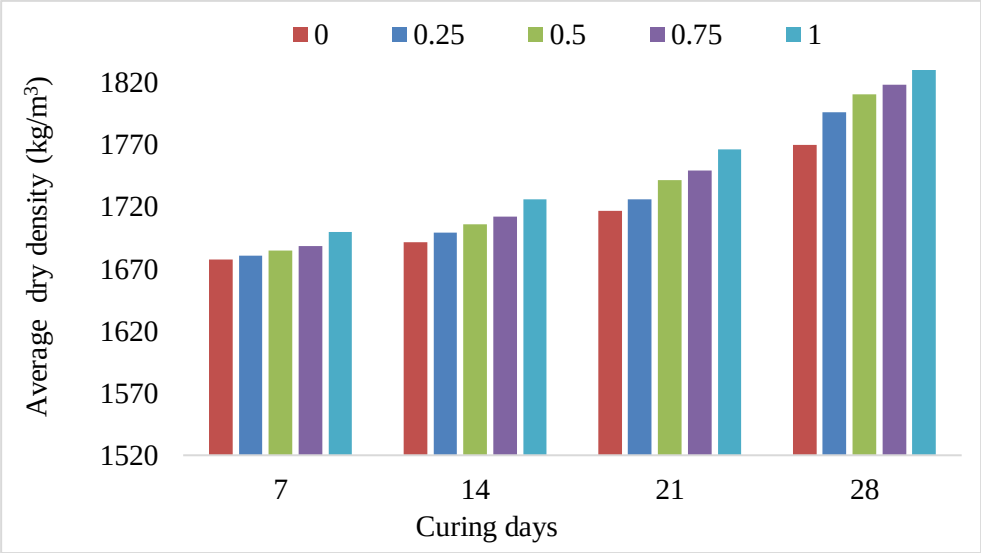

Fig. 5: Density of CEB with eggshell and lime

Water absorption: Fig. 6 illustrates the average water absorption of eggshell and lime samples cured at different times. This study used eggshell content of 0, 0.25, 0.50, 0.75, and 1% with curing days of 7 and 28. The results showed reduced water absorption with increased eggshell and lime content. The water absorption percentages at 28 days of curing, the water absorption were 4.62, 4.27, 3.53, 3.32, and 2.60% for eggshell content of 0, 0.25, 0.5, 0.75, and 1% respectively. This supports prior research on eggshell powder and concrete water absorption [59, 60]. The reduction in water absorption observed with increasing eggshell and lime content can be attributed to the combined effects of particle packing and pores filling. Eggshell powder, with its finer particle size compared to the traditional lime stabiliser, fills the voids between soil particles, reducing the total porosity and thereby water absorption capacity [60]. Additionally, eggshells contain calcium carbonate ($CaCO_3$), which can react with water to form a gel filling even smaller pores [61]. While Danso [12] and Obianyo et al. [62] specifically focused on the mechanical properties of lime-stabilised lateritic soils, their findings on pores filling by hydration support this explanation. The denser microstructure created by eggshell powder, along with its potential pozzolanic reaction (where it reacts with calcium hydroxide to form additional cementitious compounds), significantly reduces water absorption in the CEBs. The difference in water absorption values between the control group (0% eggshell) and the group with the highest eggshell stabiliser content (1%) was significant, with a reduction in water absorption from 4.62 to 2.60%. This represents about 78% water absorption reduction, indicating a clear impact of the eggshell and lime stabiliser in reducing the uptake of water by the CEB. Water absorption sturdily affects the mechanical and durability of CEBs [63].

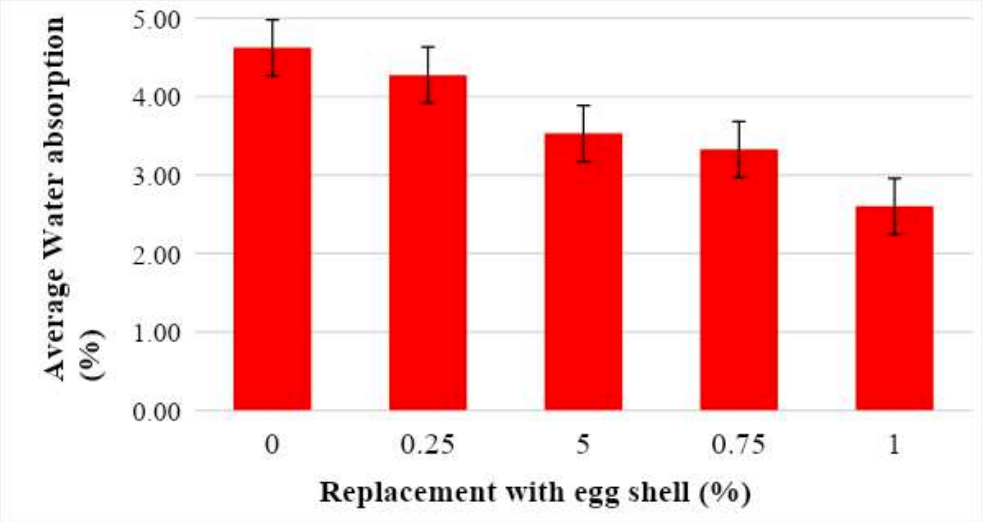

Fig. 6: Water absorption of CEB with eggshell and lime

4.2 Mechanical Properties

Compressive and tensile strength test results were used to assess the mechanical properties of the CEBs stabilised with eggshell and lime.

Compressive strength: Fig. 7 shows the earth blocks stabilised with 0, 0.25, 0.5, 0.75, and 1 % eggshells and lime after curing for 7, 14, 21, and 28 days' result. The result illustrates that as the eggshell content and the lime increased the strength also increased for all the curing ages. CEBs with 1% eggshells and lime achieved the highest compressive strength of 1.331 N/mm² as compared with the control group of 1.054 N/mm² at 28 days of curing, which represents a 21% increase in compressive strength. The compressive strengths of CEBs between 1.054 and 1.331 N/mm² obtained from this study were above the recommended minimum value for use in building applications according to TS 704 [64] recommendation of 1 MPa. The result indicates that the highest eggshell content and the lime achieved the maximum strength, which implies that further addition of the eggshell content could result in additional strength. Similar studies by Kaur et al. [65] and Singh et al. [66] on earth block strength and curing and stabilisers' results indicated that as the curing time increased, the compressive strength of the blocks increased. The improved strength result could be attributed to the eggshell's increased compaction with the earth block [67] and the lime's chemical reaction in the CEBs. The lime acts as a binder in the matrix such that the calcium oxide, silica, and alumina composition propels hydration reaction with the soil particles in order to seal the voids in the composite [39]. The One-Way ANOVA test on results from three replicates of each mix design at 95% confidence interval was conducted on the 28-day compressive strength result for the control and the 1% eggshell and lime CEBs. It was found that the p-value was 0.016 which implies a statistically significant difference between the highest and the lowest compressive strength of the CEBs.

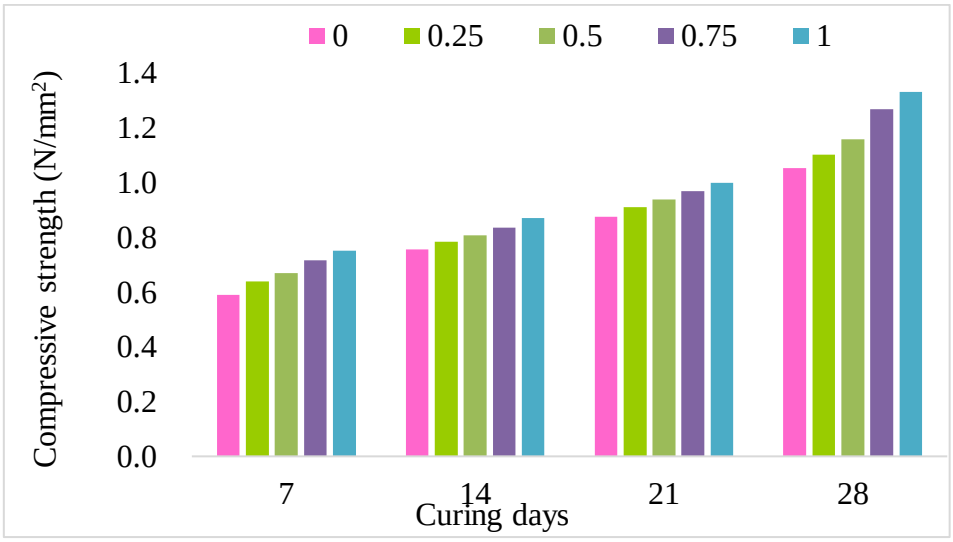

Fig. 7: Compressive strength CEBs with eggshell and lime

Tensile strength: CEBs' resistance to crack development in walls depends on their split tensile strength. This study assessed the average CEBs' split tensile strength for different curing days and eggshell and lime stabiliser concentrations. Fig. 8 shows that CEBs' split tensile strength increases with curing days and eggshell stabiliser content. The result shows a progressive increase in strength from 0.138 N/mm² (0.25% eggshell) to 0.173 N/mm² (1% eggshell) after 28 days of curing. Notably, the group with 1% eggshell stabiliser exhibited a 20% increase in split tensile strength compared to the control group (0.138 N/mm²). The result supports prior studies' results that found that eggshell powder strengthens crushed earth blocks [68, 69]. The increased tensile strength can be attributed to the eggshells' ability to adhere to the soil particles and the lime. Furthermore, the binding characteristics of lime boost chemical reactions in the mixture, which contributes to improved strength development [39]. There was no statistically significant difference in mean values between treatment groups ($p = 0.333$), therefore random sampling variability could explain the discrepancy as indicated by an ANOVA test result.

It could be observed that both compressive strength and tensile strength of the eggshell and lime stabilised CEBs increased with increased quantities of eggshell with 1% eggshell emerging as the highest in terms of mechanical properties. This implies that increasing the 1% eggshell quantities in the CEBs could result in a further increase in the mechanical properties beyond the 1%.

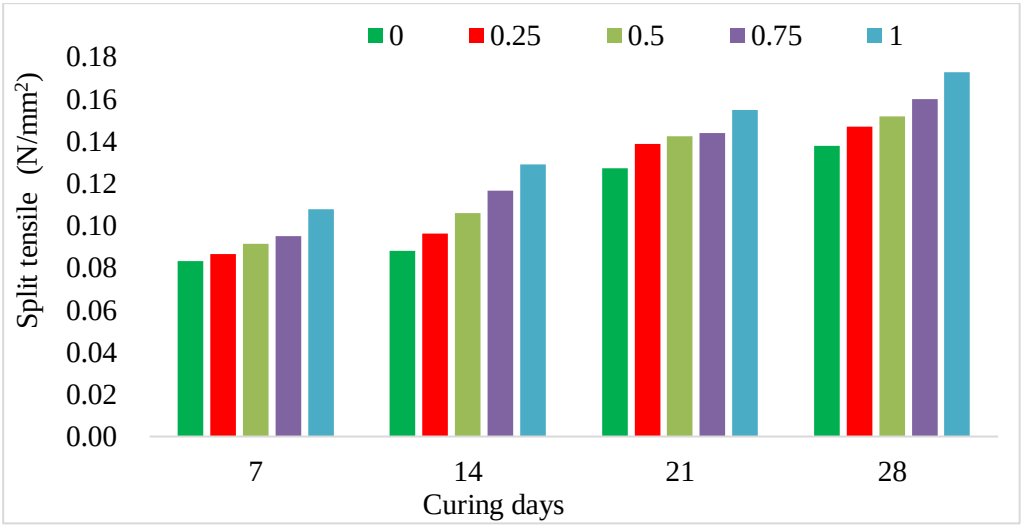

Fig. 8: Split tensile strength of CEBs with eggshell and lime

4.3 Durability Properties

Erosion resistance: The drip test method was used to assess the erosion resistance of CEBs with and without eggshells and lime stabilisers and the result is shown in Table 3. The purpose of this test was to evaluate the CEBs' ability to withstand water (rainfall) when applied externally to wall surfaces. The control samples experienced erosion with depths ranging from 6 to 12 mm and diameters ranging from 15 to 18 mm, which is consistent with findings from Ajayi et al. [68] who reported similar erosion in compressed stabilised laterite blocks. Another study by Danso [12] reported a similar trend of erosion when natural fibres from agricultural waste were used to reinforce CEBs. In contrast, no erosion was observed in any of the samples containing eggshell and lime stabilisers, regardless of the concentration. This suggests that eggshell and lime stabilisers are effective in enhancing the erosion resistance of CEBs, corroborating the findings of Ajayi et al. [70], Danso and Manu [39], Elavarasan et al. [47] and Jannat et al. [49] on the use of eggshell powder, coconut fibres, ash, and lime as soil stabiliser in CEBs.

Table 3: Erosion of CEBs with eggshell and lime

Eggshell Content (%)	0	0.25	0.50	0.75	1
Depth range (mm)	6 - 12	0 - 0	0 - 0	0 - 0	0 - 0
Diameter range (mm)	15 - 18	0 - 0	0 - 0	0 - 0	0 - 0

4.4 SEM and EDS Analysis

Running scanning electron microscopy (SEM) and energy-dispersive X-ray spectroscopy (EDS) analyses on eggshell and lime-compressed earth blocks can provide valuable insights into their microstructural, elemental, and chemical compositions.

CEBs with eggshell and lime morphology: Multidimensional SEM examinations of eggshell and lime CEB samples revealed their microstructure details including surface texture, pore distribution, and mineralized structural arrangement as shown in Figs. 9a and 9b. The blend of earth, lime, and eggshell showed soil particle and aggregation patterns, which reveal structure, lime particle crystal shape, crack distribution, and surface properties.

Crushed eggshells and lime CEB's chemical characteristics: CEB with eggshell and lime chemical compositions were determined using energy-dispersive X-ray spectroscopy. Fig. 9c shows the elemental composition of the CEBs. The main elements revealed are iron (26%), titanium (22%), calcium (20), silicon (14%), aluminium (13%), oxygen (8%), and carbon (6%). The mixture of lime, earth, and eggshell revealed high calcium percentages and had elemental compositions that improved CEB strength and other mechanical properties. CEBs' main binding agent is calcium silicate hydrates that improve strength [71]. Pozzolanic silica fume strengthens and lowers permeability [72]. Aluminium compounds such as tricalcium aluminate affect early strength [73]. Iron compounds, notably ferrite phases, make CEBs strong and colourful [74]. Magnesium compounds affect CEBs strength and durability [75]. Gypsum and other sulphates alter CEB curing time and strength [76]. Phosphate-based additions can boost early strength [77]. Calcium chloride accelerates strength gain [78]. Therefore, it is not surprising that the eggshell and lime CEBs had greater strength analysis than the control blocks without lime and eggshells.

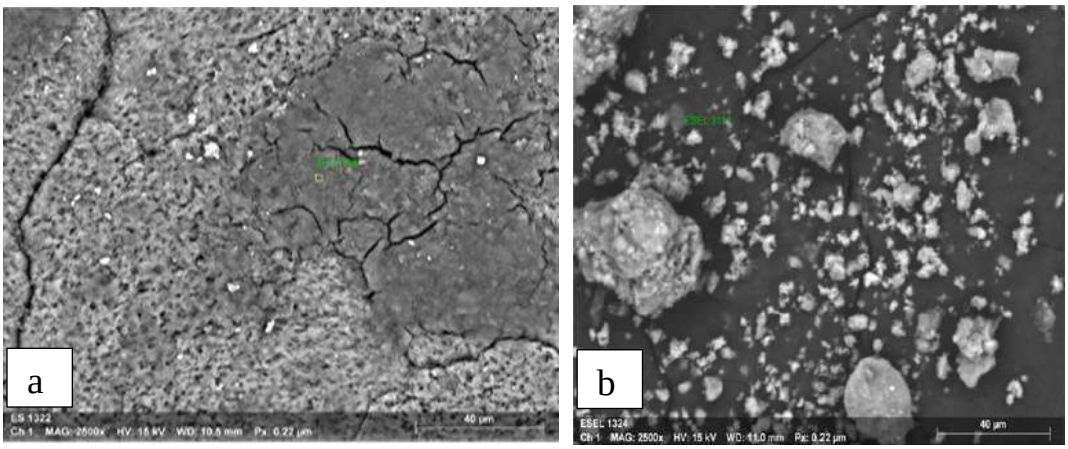

Element	At. No.	Netto	Mass [%]	Mass Norm. [%]	Atom [%]	abs. error [%] (1 sigma)	rel. error [%] (1 sigma)
Carbon	6	18273	9.43	19.58	28.36	1.25	13.22
Oxygen	8	49651	26.54	55.10	59.90	3.16	11.89
Aluminium	13	9049	1.40	2.90	1.87	0.09	6.67
Silicon	14	8954	1.19	2.47	1.53	0.08	6.51
Calcium	20	55722	8.05	16.71	7.25	0.27	3.32
Titanium	22	1607	0.77	1.60	0.58	0.06	7.32
Iron	26	742	0.79	1.63	0.51	0.07	8.27
		Sum	**48.17**	**100.00**	**100.00**		

c

Fig. 9: SEM and EDS images of CEBs with eggshell and lime: (a) surface texture, pores and cracks distribution, (b) mineralized structural arrangement, and (c) elemental composition

V. CONCLUSION

This study demonstrates the significant potential of utilising eggshells and lime as sustainable stabilisers for compressed earth blocks (CEBs). The inclusion of eggshell and lime stabilisers at varying concentrations (0.25%, 0.5%, 0.75%, and 1%) consistently enhanced the physical, mechanical, and durability properties of the CEBs. At 28 days of curing, the 1% eggshell and 10% lime-stabilised compressed earth blocks recorded compressive strength of 1.331 N/mm² compared with the unstabilised compressed earth blocks' strength of 1.054 N/mm², which represents a 21% increase in compressive strength, and the difference was found be statistically significant ($p = 0.016$). At 28 days of curing, the 1% eggshell and 10% lime-stabilised compressed earth blocks' tensile strength was 0.173 N/mm² compared with the unstabilised compressed earth blocks' strength of 0.138 N/mm², which represents a 20% tensile strength increase. The eggshell and lime-stabilised compressed earth blocks also exhibited reduced water absorption of 3.32% compared to unstabilised blocks of 4.62%. SEM analysis revealed the earth particle structure, lime particle crystal shape, crack distribution, and surface properties of the CEBs. EDS analyses further confirmed the presence of key elements like iron, titanium, calcium, silicon, aluminium, oxygen, and carbon in the CEBs. The study, therefore, concludes that the presence of eggshells and lime in the earth matrix enhanced the properties of the compressed earth blocks for construction applications. The overall findings strongly support the use of eggshells and lime as eco-friendly and effective stabilisers for producing acceptable CEBs, presenting a promising avenue for sustainable construction practices. The waste eggshells can be obtained with no cost and therefore promote low-cost construction materials usage. The use of waste eggshells and lime in CEBs has the potential to encourage affordable

and eco-friendly alternative construction material for low-income communities. It is recommended that block manufacturers to improve the properties of the compressed earth blocks should use 1% eggshell and 10% lime. It is further recommended that future studies explore different types of lime, varying the proportions of eggshells, especially beyond 1%, or test the blocks in different environmental conditions. Future studies should also consider long-term durability studies to confirm the effectiveness of the eggshell lime CEBs under real-world conditions.

Declarations

Funding Statement

This research did not receive any specific grant from funding agencies in the public, commercial, or not-for-profit sectors.

Data Availability

Data available on demand.

Declaration of interest's statement

The authors declare no conflict of interest.

Additional Information

No additional information is available for this paper.

REFERENCES

1. S. Rolfe, L. Garnham, J. Godwin, I. Anderson, P. Seaman, C. Donaldson, Housing as a social determinant of health and wellbeing: developing an empirically-informed realist theoretical framework. BMC Public Health 20 (2020) 1138. https://doi.org/10.1186/s12889-020-09224-0
2. J. Bredenoord, Sustainable Building Materials for Low-cost Housing and the Challenges Facing their Technological Developments: Examples and Lessons Regarding Bamboo, Earth-Block Technologies, Building Blocks of Recycled Materials, and Improved Concrete Panels, Journal of Architectural Engineering Technology 06 (01) (2017). https://doi.org/10.4172/2168-9717.1000187
3. A. P. A. Sapna, C. Anbalagan, Sustainable Eco-Friendly Building Material – A Review Towards Compressed Stabilised Earth Blocks and Fire Burnt Clay Bricks. IOP Conference Series: Earth and Environmental Science, 1210 (1) (2023) 012023 https://doi.org/10.1088/1755-1315/1210/1/012023
4. H. Danso, Use of Agricultural Waste Fibres as Enhancement of Soil Blocks for Low-Cost Housing in Ghana, PhD thesis, University of Portsmouth, London (2016).
5. H. Danso, Influence of Compacting Rate on the Properties of Compressed Earth Blocks, Advances in Materials Science and Engineering 2016 (2016). http://dx.doi.org/10.1155/2016/8780368
6. C. Turco, A. C. Paula, E. Teixeira, R. Mateus, Optimisation of Compressed Earth Blocks (CEBs) using natural origin materials: A systematic literature review, Construction and Building Materials 309 (2021) 125140. https://doi.org/10.1016/j.conbuildmat.2021.125140
7. R. Mateus, J. E. P. Fernandes, E. Teixeira, Environmental Life cycle analysis of earthen building materials. In Elsevier eBooks (2020) 63–68. https://doi.org/10.1016/b978-0-12-803581-8.11459-6
8. M. M. Musa, A. N. Zadawa, M. Abubakar, M. A. Dandajeh, A. S. Shehu, Critical success factors for affordable housing projects in Nigeria. Malaysian Journal of Real Estate 17 (2) 2023 80–89. https://doi.org/10.11113/intrest.v17n2.310
9. B. M. Ali, M. Akkaş, The Green Cool Factor: Eco-Innovative HVAC Solutions in Building Design, Applied Sciences 14 (2024) 195 https://doi.org/10.3390/app14010195
10. A. Gamal, O. A. Eleinen, S. Eltarabily, D. Elgheznawy, Enhancing urban resilience in hot humid climates: A conceptual framework for exploring the environmental performance of vertical greening systems (VGS), Frontiers of Architectural Research 12 (6) (2023) 1260–1284. https://doi.org/10.1016/j.foar.2023.09.003
11. H. Danso, Building Houses with Locally Available Materials in Ghana: Benefits and Problems, International Journal of Science and Technology 2 (2) (2013) 225-231.
12. H. Danso, Improving Water Resistance of Compressed Earth Blocks Enhanced with Different Natural Fibres, The Open Construction and Building Technology

Journal 11 (1) (2017) 433–440 https://doi.org/10.2174/1874836801711010433
13. P. Shantanu, S. I. Mohammad, I. H. Mohammad, Suitability of Vetiver straw fibers in improving the engineering characteristics of compressed earth blocks, Construction and Building Materials 409 (2023) 134224, https://doi.org/10.1016/j.conbuildmat.2023
14. O. Oguntola, S. Simske, Continuous Assessment of the Environmental Impact and Economic Viability of Decarbonization Improvements in Cement Production, Resources 12 (2023) 95 https://doi.org/10.3390/resources12080095
15. V. Seevaratnam, D. Uthayakumar, N. Sathiparan, Influence of rice husk ash on characteristics of earth cement blocks, MRS Advances, 5 (54–55) (2020) 2793–2805. https://doi.org/10.1557/adv.2020.294
16. Y. Zhang, S. Jiang, D. Quan, K. Fang, B. Wang, Z. Ma, Properties of Sustainable Earth Construction Materials: A State-of-the-Art Review, Sustainability 16(2) (2024) 670. https://doi.org/10.3390/su16020670
17. A. Raj, T. Sharma, S. Singh, U. Sharma, P. Sharma, R. Singh, S. Sharma, J. Kaur, H. Kaur, B. Salah, S. S. Ullah, S. Alkhatib, Building a Sustainable Future from Theory to Practice: A Comprehensive PRISMA-Guided Assessment of Compressed Stabilized Earth Blocks (CSEB) for Construction Applications, Sustainability 15 (12) (2023) 9374. https://doi.org/10.3390/su15129374
18. O. Ige, H. Danso, Experimental Characterization of Adobe Bricks Stabilised with Rice Husk and Lime for Sustainable Construction, Journal of Materials in Civil Engineering 34 (2) (2022). https://doi.org/10.1061/(ASCE)MT.1943-5533.0004059
19. A. O. Tanash, K. Muthusamy, Concrete Industry, Environment Issue, and Green Concrete: a review, Construction 2 (1) (2022) 01–09. https://doi.org/10.15282/construction.v2i1.7188
20. D. Yang, J. Zhao, W. Ahmad, M. Amin, F. Aslam, K. Khan, A. Ahmad, Potential use of waste eggshells in cement-based materials: A bibliographic analysis and review of the material properties, Construction and Building Materials 344 (2022) 128143. https://doi.org/10.1016/j.conbuildmat.2022.128143
21. K. Khan, W. Ahmad, M. Amin, A. F. Deifalla, Investigating the feasibility of using waste eggshells in cement-based materials for sustainable construction, Journal of Materials Research and Technology 23 (2023) 4059–4074. https://doi.org/10.1016/j.jmrt.2023.02.057
22. J. M. C. Estêvão, A. M. G. S. Braga, Damage evaluation of rammed earth walls subjected to offshore earthquakes. In Springer eBooks (2018) 513–520. https://doi.org/10.1007/978-3-319-70272-8_40
23. M. Hu, Exploring Low-Carbon Design and Construction Techniques: Lessons from Vernacular Architecture, Climate 11 (8) (2023) 165. https://doi.org/10.3390/cli11080165
24. H. Niroumand, M. F. M. Zain, M. Jamil, Modern rammed Earth in Earth architecture, Advanced Materials Research, 457–458 (2012) 399–402. https://doi.org/10.4028/www.scientific.net/amr.457-458.399
25. X. T. Lu, Y. P. Liu, Rammed Earth Construction: a sustainable architecture, Applied Mechanics and Materials 405–408 (2013) 3131–3135. https://doi.org/10.4028/www.scientific.net/amm.405-408.3131
26. G. Treloar, C. Owen, R. Fay, Environmental assessment of rammed earth construction systems, Structural Survey 19 (2) (2001) 99–106. https://doi.org/10.1108/02630800110393680
27. C. Sposito, F. Scalisi, Sustainable architecture: the eco-efficiency earth construction, European Journal of Sustainable Development 6(4) (2017). https://doi.org/10.14207/ejsd.2017.v6n4p246
28. C. Librici, D. V. Oliveira, R. A. M. Silva, Seismic assessment of a vernacular rammed earth building, Report (2017). https://doi.org/10.2749/vancouver.2017.0152
29. J. Van Der Linden, B. Janssens, E. Knapen, Potential of contemporary earth architecture for low impact building in Belgium, IOP Conference Series: Earth and Environmental Science, 323 (1) (2019) 012018

30. I. Hegediš, G. Karaman, A. Čeh, N. Đurić, D. Kukaras, D. Vunjak, Energy Sustainability of Rammed Earth Buildings, Arhiv Za Tehničke Nauke, 2 (17) (2017) 39–48. https://doi.org/10.7251/afts.2017.0917.039h
31. D. D. Tripura, K. D. Singh, Characteristic properties of Cement-Stabilised Rammed Earth blocks, Journal of Materials in Civil Engineering 27 (7) (2015) https://doi.org/10.1061/(asce)mt.1943-5533.0001170
32. C. Ferraresi, W. Franco, G. Quaglia, Concept and Design of Float-Ram: A New Human Powered Press for Compressed Earth Blocks, The American Society of Mechanical Engineers 11 8(2017). https://doi.org/10.1115/imece2017-70384
33. L. Miccoli, U. Müller, P. Fontana, Mechanical behaviour of earthen materials: A comparison between earth block masonry, rammed earth and cob, Construction and Building Materials 61 (2014) 327–339. https://doi.org/10.1016/j.conbuildmat.2014.03.009
34. E. Hamard, B. Cazacliu, A. Razakamanantsoa, J. Morel, Cob, a vernacular earth construction process in the context of modern sustainable building, Building and Environment 106 (2016) 103–119. https://doi.org/10.1016/j.buildenv.2016.06.009
35. S. Cabrera, A. Guillarducci, D. González, M. Suarez, Evaluación del coeficiente de conductividad y transmitancia térmica de elementos constructivos de tierra, Revista Hábitat Sustentable 13 (1) (2023) 08–19. https://doi.org/10.22320/07190700.2023.13.01.01
36. C. Beckett, P. Jaquin, J. Morel, Weathering the storm: A framework to assess the resistance of earthen structures to water damage, Construction and Building Materials 242 (2020) 118098. https://doi.org/10.1016/j.conbuildmat.2020.118098
37. R. Eires, A. Camões, S. Jalali, Enhancing water resistance of earthen buildings with quicklime and oil, Journal of Cleaner Production 142 (2017) 3281–3292. https://doi.org/10.1016/j.jclepro.2016.10.141
38. H. Danso, Influence of Plantain Pseudostem Fibres and Lime on the Properties of Cement Mortar, Advances in Materials Science and Engineering 2020 (2020) 1-9, https://www.hindawi.com/journals/amse/2020/4698603/
39. H. Danso, D. Manu, Influence of Coconut Fibres and Lime on the Properties of Soil-Cement Mortar, Case Studies in Construction Materials 12 (2020) 1-12. https://doi.org/10.1016/j.cscm.2019.e00316
40. G. Vasudevan, S. C. Wei, Utilisation of Eggshell Powder (ESP) as Partial Replacement of Cement Incorporating Superplasticizer, IOP Conference Series: Materials Science and Engineering 840 (1) (2020) 012016, https://doi.org/10.1088/1757-899x/840/1/012016
41. G. Vasudevan, K. Uthayasirppi, M. M. B. Hassim, Strength and Durability Properties Empty Fruit Bunch Ash (EFBA) as Partial Replacement of Cement. In Proceedings of the 6th International Conference on Civil Engineering, ICOCE 2022, Singapore 276 (2022) 49–57. https://doi.org/10.1007/978-981-19-3983-9_5
42. Y. Y. Tan, S. I. Doh, S. C. Chin, Eggshell as a partial cement replacement in concrete development, Magazine of Concrete Research 70 (13) (2018) 662–670. https://doi.org/10.1680/jmacr.17.00003
43. A. Saini, A. K. Singh, A. Tiwari, Study the behaviour of cement mortar containing jute fiber along with partial replacement of cement with eggshell powder. International Journal of Current Engineering and Technology 11(04) (2021) 438–443. https://doi.org/10.14741/ijcet/v.11.4.8
44. B. H. Amanah, W. I. Khalil, Evaluating the use of eggshell waste ash in high strength concrete, Mağallat¨ Al-handasat¨ Wa-al-tiknūlūğiyā 39 (8) (2021) 1321–1327. https://doi.org/10.30684/etj.v39i8.2102
45. L. Mahmood, S. Rafiq, A. Mohammed, A review study of eggshell powder as cement replacement in concrete. Sulaimani Journal for Engineering Sciences 9 (1) (2022) 25–38
46. S. A. Abri, C. R. Rollakanti, K. K. Poloju, A. Joe, Experimental Study on Mechanical Properties of Concrete by Partial Replacement of Cement with Eggshell Powder for Sustainable Construction, Materials Today:

Proceedings 65 (2022) 1660–1665. https://doi.org/10.1016/j.matpr.2022.04.708
47. S. Elavarasan, A. Priya, K. Elango, S. Shahithya, A review on addition of egg shell powder to CSEB blocks, Materials Today: Proceedings (2023). https://doi.org/10.1016/j.matpr.2023.03.718
48. N. C. Consoli, A. Lotero, R. B. Saldanha, H. C. S. Filho, C. J. M. Acosta, Eggshell produced limes: innovative materials for soil stabilization, Journal of Materials in Civil Engineering 32(11) (2020). https://doi.org/10.1061/(asce)mt.1943-5533.0003418
49. N. Jannat, R. L. Al-Mufti, A. Hussien, B. M. Abdullah, A. Cotgrave, Influences of agro-wastes on the physico-mechanical and durability properties of unfired clay blocks, Construction and Building Materials 318 (2022) 126011. https://doi.org/10.1016/j.conbuildmat.2021.126011
50. BS 1377, Methods of test for soils for civil engineering properties, Classification tests, British Standard Institution, London UK (1990).
51. R. Karthik, D. Ramachandraiah, A review of green supply chain management: From bibliometric analysis to a conceptual framework, Journal of Cleaner Production, 181 (2018) 34-52.
52. BS EN 772-1, Methods of test for masonry units, Determination of Compressive Strength, European Standards adopted by British Standards Institution, London UK (2011).
53. BS EN 12390-6, Testing hardened concrete, Tensile Splitting Strength of Test Specimens, European Standard adopted by British Standards Institution, London UK (2009).
54. NZS 4298, Materials and workmanship for earth buildings, New Zealand Standard, Wellington, New Zealand (1998).
55. BS EN 772-11, Methods of Test for Masonry Units, European Standards adopted by British Standards Institution (2011).
56. BS EN 771-1, Specification for masonry units, Clay Masonry Units, European Standard adopted by British Standards Institution (2003).
57. I. Zamani, H. Hamid, M. S. Abd Majid, Stabilised rammed earth using egg shells, lime and cement, Cement & Concrete Composites 27 (8) (2005) 999-1005.
58. S. Anoop, H. Beegom, J. P. Johnson, J. Midhula, S. Prasanth, Potential of Egg shell powder as replacement of Lime in soil stabilization, International Journal of Advanced Engineering Research and Science 4 (8) (2017) 86–88. https://doi.org/10.22161/ijaers.4.8.15
59. B. Cetin, S. B. Keskin, The effect of eggshell powder on the mechanical properties of concrete; Construction and Building Materials 98 (2015) 540-548.
60. W. Jiang, H. Li, H. Zhang, J. Zhou, R. Wang, Effects of eggshell powder on properties of cement-based materials, Construction and Building Materials 250 (2020) 118908
61. S. Makkar, N. C. Rath, B. Packialakshmi, W. E. Huff, G. R. Huff, Nutritional effects of egg shell membrane supplements on chicken performance and immunity, Poultry Science 94 (6) (2015) 1184-1189, https://doi.org/10.3382/ps/pev098.
62. I. I. Obianyo, A. P. Onwualu, A. Soboyejo, Mechanical behaviour of lateritic soil stabilised with bone ash and hydrated lime for sustainable building applications, Case Studies in Construction Materials 12 (2020) e00331, https://doi.org/10.1016/j.cscm.2020.e00331
63. J. T. Darman, J. H. K. Tchouata, G. F. N. Ngôn, F. Ngapgue, B. L. Ngakoupain, Y. T. Langollo, Evaluation of lateritic soils of Mbé for use as compressed earth bricks (CEB), Heliyon 8 (8) (2022) e10147, https://doi.org/10.1016/j.heliyon.2022.e10147
64. TS 704:1985 Solid brick and vertically perforated bricks (the classification, properties, sampling, testing and marking of solid bricks and vertically perforated bricks), Ankara: Turkish Standard Institution. (2001)
65. H. Kaur, V. Sharma, D. R. Khanduja, Mechanical properties of lime and ash stabilised earth blocks, Construction and Building Materials 186 (2018) 849-858.
66. S. Singh, J. S. Chohan, R. Kumar, P. K. Gupta, Stability of compressed earth blocks using sugarcane bagasse ash and wheat straw, Materials Today Proceedings 51 (2022)

993-997. https://doi.org/10.1016/j.matpr.2021.07.023
67. I. K. Adegun, A. O. Oluwajobi, O. J. Akintorinwa, Effect of Eggshell Ash on the Compressive Strength and Water Absorption of Compressed Earth Blocks, Journal of Civil Engineering Research and Practice 6 (1) (2019) 39-47.
68. L. Wang, Y. Cao, S. Du, L. Zhang, Effects of eggshell powder on the mechanical properties of compressed earth blocks, Journal of Building Engineering 26 (2019) 100879 https://doi.org/10.1016/j.jobe.2019.100879
69. M. Turel, B. Turel, A. Korkut, Effect of eggshell powder on the properties of compressed earth blocks, Journal of Building Engineering 43 (2021) 102619 https://doi.org/10.1016/j.jobe.2021.102619
70. O. O. Ajayi, O. D. Adeboye, F. A. Oyawale, Effects of Eggshell Powder on Compressive Strength and Durability of Compressed Stabilised Laterite Blocks, International Journal of Engineering and Advanced Technology 6 (4) (2016) 17-21
71. H. F. W. Taylor, Cement chemistry (2nd Ed.). Thomas Telford, London UK (1997)
72. V. M. Malhotra, K. M. Rame Gowda, C. Q. Li, Properties of high-performance silica fume concretes containing supplementary cementing materials, ACI Materials Journal 103(3) (2006) 186-195
73. H.W.M. Hewlett, L.A. Boorman, M. E. Bramley, Design of reinforced grass waterways, CIRIA Report 116, Construction and Industry Research and Information Association, London UK (1987)
74. S. Mindess, J. F. Young, D. Darwin, Concrete, Pearson Education, Upper Saddle River, NJ (2003).
75. A. M. Neville, Properties of concrete (5th Ed.), Pearson Harlow, UK (2011).
76. P. K. Mehta, P. J. M. Monteiro, Concrete: microstructure, properties, and materials (4th Ed.). McGraw-Hill, New York (2014).
77. M. C. G. Juenger, R. Siddique, Early-age strength enhancement of concretes containing high additions of limestone powder, Construction and Building Materials 186 (2018) 872-885.
78. ACI Committee 227, Guide to the Use of Calcium Chloride in Concrete (ACI 227R-19). American Concrete Institute, Farmington Hills, MI (2019).

This page is intentionally left blank

A Novel Method for Assessing Pirate Attack Risks and Spatial Distribution

Junbo Wang, Beimin Zhang, Shisheng Zhao, Qingtao Wang, Yifan Liu, Song Li & Yuanqiang Zhang

Ningbo Aids to Navigation Department of Donghai Navigation Safety Administration

ABSTRACT

Pirate attacks pose one of the most severe challenges to the safety of maritime navigation. Effectively quantifying the risk of pirate attacks and understanding their spatial distribution through historical records is crucial for planning safe shipping routes. Given the diverse data types and multiple factors involved in assessing pirate attacks recorded in the Global Integrated Shipping Information System (GISIS) database, we propose a spatiotemporal influence factor analysis model based on the K-means clustering algorithm. Features are encoded using an Autoencoder, and the evaluation is conducted using the Entropy Weight Method- Technique for Order Preference by Similarity to Ideal Solution (EWM-TOPSIS). The model then simulates and predicts the geographical distribution of pirate risks. The results indicate that the model effectively captures the geographical distribution patterns of pirate attack incidents and successfully predicts the risk distribution across different sea areas. This approach aids in ship route planning and reduces the risk of pirate attacks.

Keywords: pirate attacks; risk analysis; K-means clustering; Autoencoder; EWM-TOPSIS.

Classification: DDC Code: 004

Language: English

LJP Copyright ID: 392953
Print ISSN: 2631-8474
Online ISSN: 2631-8482

London Journal of Engineering Research

Volume 24 | Issue 7 | Compilation 1.0

A Novel Method for Assessing Pirate Attack Risks and Spatial Distribution

Junbo Wang[α], Beimin Zhang[σ], Shisheng Zhao[ρ], Qingtao Wang[w], Yifan Liu[¥], Song Li[§] & Yuanqiang Zhang[χ]

ABSTRACT

Pirate attacks pose one of the most severe challenges to the safety of maritime navigation. Effectively quantifying the risk of pirate attacks and understanding their spatial distribution through historical records is crucial for planning safe shipping routes. Given the diverse data types and multiple factors involved in assessing pirate attacks recorded in the Global Integrated Shipping Information System (GISIS) database, we propose a spatiotemporal influence factor analysis model based on the K-means clustering algorithm. Features are encoded using an Autoencoder, and the evaluation is conducted using the Entropy Weight Method- Technique for Order Preference by Similarity to Ideal Solution (EWM-TOPSIS). The model then simulates and predicts the geographical distribution of pirate risks. The results indicate that the model effectively captures the geographical distribution patterns of pirate attack incidents and successfully predicts the risk distribution across different sea areas. This approach aids in ship route planning and reduces the risk of pirate attacks.

Keywords: pirate attacks; risk analysis; K-means clustering; Autoencoder; EWM-TOPSIS.

Author α σ ρ ↀ: Ningbo Aids to Navigation Department of Donghai Navigation Safety Administration, Ningbo315470, China.
¥ § χ: Faculty of Maritime and Transportation, Ningbo University, Ningbo315832, China.

I. INTRODUCTION

Maritime transportation plays a pivotal role in the development of the global supply chain. According to the International Maritime Organization (IMO), nearly 90% of the world's trade is conducted by sea [1]. However, the increasing frequency of pirate attacks has become a significant challenge for the maritime industry and one of the most serious and unsettling issues facing the international community [2][3]. Thus, effectively assessing the risk of pirate attacks and predicting the geographical distribution of piracy risk to aid in route planning for ships has become a critical task.

Current research on pirate attacks primarily focuses on three areas: descriptive statistical analysis, analysis of influencing factors, and risk assessment of pirate attacks. In terms of descriptive statistical analysis, Nwalozie analyzed contemporary piracy in Nigeria, the Niger Delta, and the Gulf of Guinea [4]. Denton et al. conducted a statistical analysis of piracy activities in the Gulf of Guinea, showing that stronger and democratic regimes are less likely to encounter piracy [5]. Regan used nonprobability sampling to analyze piracy cases between 1985 and 2018 in 11 countries, based on data from various organizations. Key predictors of piracy frequency were total country population, total fish tonnage, gross domestic product, and government weakness [6].

For analyzing the influencing factors of pirate attacks, Bayesian networks are commonly used for risk assessment and prediction. Jiang et al. utilized a Bayesian network to estimate the likelihood of ships being attacked or hijacked in Southeast Asia, considering the uncertainty of influencing factors [7]. Fan et al. proposed a two-stage technique for order of preference by similarity to an ideal solution (TOPSIS) model based on the Bayesian network. In the first stage, a data-driven Bayesian network identifies causal relationships influencing pirate behaviors. The second stage involves calculating a decision

matrix of strategies using TOPSIS, enhancing the strength of risk prediction and dynamic diagnosis by the Bayesian network [8]. Dabrowski et al. presented a novel generative model based on dynamic Bayesian networks (DBN) to simulate maritime vessel behavior, especially in piracy scenarios, allowing for the evaluation and optimization of behavior models through synthetic data generation and analysis [9].

Regarding the risk assessment of pirate attacks, Gong et al. proposed a two-step analytical framework based on a Random Forest (RF) model, Generative Adversarial Nets (GANs), and Matrix Completion (MC) algorithm to assess the risks of successful piracy attacks [10]. Vaněk et al. developed AGENTC, a data-driven agent-based simulation model of maritime traffic that explicitly models pirate activity and countermeasures. This model simulates the behavior and interactions of thousands of vessels, capturing the complex dynamics of the maritime transportation system under piracy threat and assessing various countermeasures [11]. Jin et al. used data on piracy attacks between 1994 and 2017 to estimate the probability of a vessel being attacked and the success rate of these attacks. Their binary logistic regression model showed that smaller vessels and open registry vessels are more likely to be targeted by pirates [12]. Pristrom et al. proposed a flexible model for assessing piracy and robbery risks in merchant ship operations, analyzing incidents based on major influencing factors such as ship characteristics and geographical locations. An analytical model incorporating Bayesian reasoning was proposed to estimate the likelihood of a ship being hijacked in the Western Indian or Eastern African regions [13].

In summary, current research rarely integrates the spatiotemporal characteristics of pirate attacks, evaluates and analyzes risks, and predicts the geographical distribution of piracy risk. This paper addresses this gap by proposing a novel risk assessment algorithm for pirate attacks that considers spatiotemporal characteristics. Using K-means clustering, Autoencoder, and the Entropy Weight Method-TOPSIS (EWM-TOPSIS), this algorithm can simulate and predict the geographical distribution of piracy risk, providing crucial information for ship route planning and significantly reducing the risk of pirate attacks.

II. MATERIALS AND METHODS

This research begins by extracting pirate attack data from the Global Integrated Shipping Information System (GISIS) database. Using the K-means clustering algorithm, we delineate zones and construct external competition factors, internal attraction factors, quantity factors, and temporal factors. Based on these four related factors, we derive the geographical probability factor. Subsequently, we apply an Autoencoder to encode the features of the four risk impact indicators: geographical probability factor, number of pirates, weapon equipment score, and loss score. Finally, we use the EWM-TOPSIS method to conduct a comprehensive risk assessment and employ the nearest neighbor interpolation method to obtain the simulated and predicted distribution of pirate attack risks across different sea areas. The specific methodology and process flow are illustrated in Figure 1.

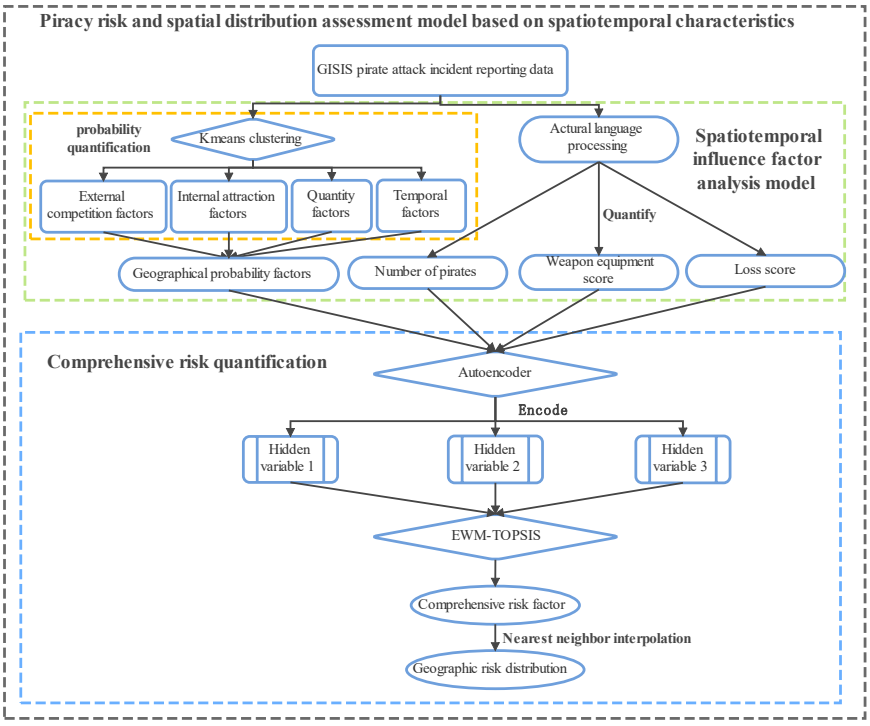

Figure 1: Algorithm flow structure chart

2.1 Analysis of Risk Influencing Factors in Pirate Attack Incidents

The risk of pirate attacks is influenced by several critical factors, including Geographical Probability Factor of Pirate Attacks, Number of Pirates, Weapons, and Losses Caused by the Attacks.

2.1.1 Geographical Probability Factor of Pirate Attacks

Hotspot areas typically indicate a higher density of pirate activities in a specific region during a particular time period, thereby significantly increasing the potential risk of ships encountering pirate attacks in these regions. Additionally, within the same maritime area, multiple types of pirate groups may exist, which can sometimes engage in conflicts or collusion with one another [14]. Therefore, this research constructs a geographical probability factor of pirate attacks to comprehensively quantify these influencing factors.

2.1.2 Number of Pirates

The number of pirates is a crucial factor in assessing the risk of pirate attacks. A larger number of pirates makes it more challenging for ships to effectively defend against attacks, thereby increasing the overall risk. This research incorporates the number of pirates as one of the quantifiable factors in evaluating the risk of pirate attacks, aiming to enhance the accuracy and comprehensiveness of the risk assessment.

2.1.3 Weapons

The type of weapons used by pirates significantly impacts the severity of the risk in pirate attack incidents. Pirates typically employ a variety of weapons, including boats, knives, firearms, and rockets. Both the quantity and technological sophistication of these weapons are critical factors in risk assessment. Therefore, this research constructs a weapon equipment score to comprehensively evaluate the level of pirate armament, thereby providing a more precise quantification of the attack risk.

2.1.4 Losses Caused by Attacks

Pirate attacks can result in various types of losses, including theft of goods, hostage-taking, and casualties. The scale of these losses and the severity of the casualties reflect the increased risk

level of pirate attacks. This research constructs a loss score to quantify the extent of damage and casualties caused by pirate attacks, providing a more accurate assessment of the risk.

2.2 Quantification of Pirate Attack Risk Indicators

2.2.1 Geographical Probability Factors

The occurrence of pirate attacks is not a matter of chance. To quantify the probability of pirate incidents at various geographical locations, this research introduces the geographical probability factor.

- Clustering of Pirate Incident Hotspots Based on K-means Algorithm

K-means is a common unsupervised machine learning clustering algorithm aimed at dividing a dataset into k distinct clusters. Each sample belongs to one cluster, ensuring high similarity within the cluster and low similarity between different clusters [15]. In this research, we use the latitude and longitude data of pirate attacks as input to the K-means algorithm to identify regions with frequent pirate activities. Additionally, to set a reasonable number of pirate activity centers within a maritime area, we evaluate the number of clusters using the Sum of Squared Errors (SSE):

$$SSE = \sum_{i=1}^{k}\sum_{j=1}^{n_i}(x_{ij} - x_i')^2 + (\theta - y_i')^2 \quad (1)$$

Where n_i represents the number of pirate incidents occurring in the *i*-th pirate activity center area. x_{ij} and y_{ij} respectively denote the longitude and latitude of the *j*-th pirate incident point belonging to the *i*-th pirate activity center area. x_i' and y_i' represent the longitude and latitude of the pirate activity center point.

- Calculation of Geographical Probability Factor

Divide the maritime area into *M* grid points in an $r \times r$ grid. Using the trained K-means clustering model, each grid point is assigned to the nearest pirate activity center region. The closer a grid point is to a pirate activity center, the more frequent the pirate activities. Therefore, the internal attraction factor is derived as follows:

$$f_{ij} = \sum_{j=1}^{a_i}\sqrt{\left(u_{ij} - u_i'\right)^2 + \left(l_{ij} - l_i'\right)^2}, i = 1, \cdots, k \quad (2)$$

Where a_i represents the number of grid points contained in the*i*-th pirate activity center area; u_{ij} and l_{ij} respectively denote the longitude and latitude of the *j*-th grid point belonging to the *i*-th pirate activity center area; f_{ij} represents the internal attraction factor of the *j*-th grid point belonging to the *i*-th pirate activity center area.

There exists a competitive relationship between different pirate groups, making pirate incidents less likely to occur in overlapping areas of influence between two pirate groups. Therefore, the calculation formula for the external competition factor is as follows:

$$v_i = \frac{1}{k-1}\sum_{j \neq i}^{k} d_{ij}, i = 1, \cdots, k \quad (3)$$

Where d_{ij} represents the Euclidean distance from the *i*-th pirate activity center point to the *j*-th pirate activity center point; v_i represents the external competitive factor of the*i*-th pirate activity center point. By combining the internal attraction factor and the external competition factor, we derive the comprehensive competition factor:

$$c_{ij} = \exp\left(\frac{f_{ij}}{v_{ij}}\right), i = 1, \cdots k; j = 1, \cdots, a_i \quad (4)$$

Where c_{ij} represents the comprehensive competitive factor of the *j*-th grid point belonging to the*i*-th pirate activity center area.

If a pirate incident has recently occurred in the surrounding area of a grid point, it is likely to face another pirate attack in the near future.

Therefore, this research introduces the quantity factor N_{ij}^q and the temporal factor T_q. The quantity factor is measured by the total number of pirate incidents occurring within the four adjacent grids connected to each grid point for each year

(as shown in Figure 2). Finally, by combining the quantity factor and the temporal factor, we derive the activity factor as follows:

$$\begin{cases} E_{ij} = \sum_{q=b_1}^{b_2} N_{ij}^{q} T_q, i = 1, \cdots k; j = 1, \cdots, a_i \\ T_q = (1-t)^{b_2 - q}, q = b_1, b_1 + 1, \cdots, b_2 \end{cases} \quad (5)$$

Where b_1 and b_2 represent the selected starting and ending years of the pirate attack incidents, respectively; N_{ij}^{q} represents the quantity factor of the j-th grid point belonging to the i-th pirate activity center area in year q; T_q represents the temporal factor in year q; t represents a time hyperparameter; E_{ij} represents the activity factor of the j-th grid point belonging to the i-th pirate activity center area.

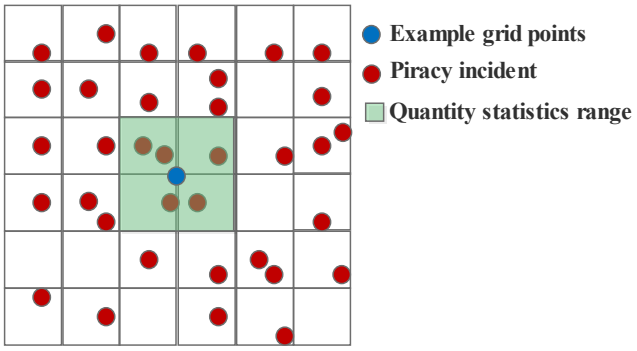

Figure 2: Quantity factor calculation diagram

By combining the comprehensive competition factor and the activity factor, followed by normalization, we obtain the geographical probability factor:

$$\begin{cases} P_{ij} = \dfrac{g_{ij}}{\sum_{i=1}^{k} \sum_{j=1}^{a_i} g_{ij}} \\ g_{ij} = \dfrac{E_{ij}}{1 + c_{ij}}, i = 1, \cdots k; j = 1, \cdots, a_i \end{cases} \quad (6)$$

Where P_{ij} represents the geographical probability factor of the j-th grid point belonging to the i-th pirate activity center area.

Finally, the Cubic Spline Interpolation algorithm is used to interpolate the geographical probability factor for each actual pirate incident location:

$$P_i' = \beta_0 + \beta_1 u_i + \beta_2 l_i + \beta_3 u_i^2 + \beta_4 u_i l_i + \beta_5 l_i^2 + \beta_6 u_i^3 + \beta_7 u_i^2 l_i + \beta_8 u_i l_i^2 + \beta_9 l_i^3 \quad (7)$$

Where $\beta_0, \beta_1, \beta_2, \beta_3, \beta_4, \beta_5, \beta_6, \beta_7, \beta_8, \beta_9$ are the coefficients of the interpolation function, obtained by selecting the 8 nearest neighboring grid points including the target point to be interpolated and setting up a linear equation system for solution. u_i and l_i respectively represent the longitude and latitude of the i-th pirate incident location. $P_i'(i = 1, 2, \cdots, n)$ represents the geographical probability factor of the i-th pirate incident location.

2.2.2 Number of Pirates

Generally, a higher number of pirates indicates a greater risk of pirate attacks. Therefore, this paper uses the number of pirates involved in each incident as one of the key indicators for assessing the risk of pirate attacks.

2.2.3. Weapon Equipment Score

Pirates typically use a variety of weapons, including knives, firearms, boats, and rockets. The quantity and technological sophistication of these weapons are critical indicators of the risk posed

2.2.3. Weapon Equipment Score

Pirates typically use a variety of weapons, including knives, firearms, boats, and rockets. The quantity and technological sophistication of these weapons are critical indicators of the risk posed by pirate attacks. Using the GISIS database, processed through natural language processing, this research extracts relevant descriptions and quantities of weapons from pirate attack reports. We then perform quantitative analysis on this information (as shown in Table 1) and calculate a weapon equipment score for each pirate attack based on the quantity and value of the weapon information:

$$Q_i = \sum_{=1}^{5} W_{ij} A_{ij}, i = 1, \cdots, n \quad (8)$$

Where W_{ij} represents the scoring of the j-th weaponry information for the i-th pirate attack incident location; A_{ij} represents the quantity of the j-th weaponry information for the i-th pirate attack incident location; Q_i represents the Weapon Equipment Score for the i-th pirate attack incident location.

Table 1: Weapons and Equipment Information Scores

Weapons and Equipment Information	Score
Knives	1
Guns	2
Boat	3
Armed	3
Rocket	4

2.2.4. Loss Score

The losses incurred from pirate attacks include theft of goods, hostage-taking, and casualties. The extent of these losses is a critical indicator of the risk associated with pirate attacks. Using the same method as for calculating the weapon equipment score, we perform a quantitative analysis of the loss information from pirate attacks (as shown in Table 2). We then compute the loss score for each pirate attack by integrating the quantity and value of the loss information:

$$L_i = \sum_{i=1}^{5} I_{ij} B_{ij}, i = 1, \cdots, n \quad (9)$$

Where I_{ij} represents the scoring of the j-th loss information for the i-th pirate attack incident location; B_{ij} represents the quantity of the j-th loss information for the i-th pirate attack incident location; L_i represents the Loss score for the i-th pirate attack incident location.

Table 2: Loss Information Score

Loss information	Score
Stolen	1
Wounded	2
Hijacked	2
Fired	3
Raft	4

2.3 Feature Encoding Based on Autoencoder

Autoencoder is a type of neural network model commonly used for feature extraction and data dimensionality reduction [16]. Compared to traditional dimensionality reduction algorithms such as Principal Component Analysis [17] and Factor Analysis [18], autoencoders can capture nonlinear data relationships while performing adaptive feature learning and more effective representation learning. Autoencoders consist of two processes: encoding and decoding. The basic structure includes an input layer, hidden layers, and an output layer (as shown in Figure 3), with the objective of minimizing reconstruction error.

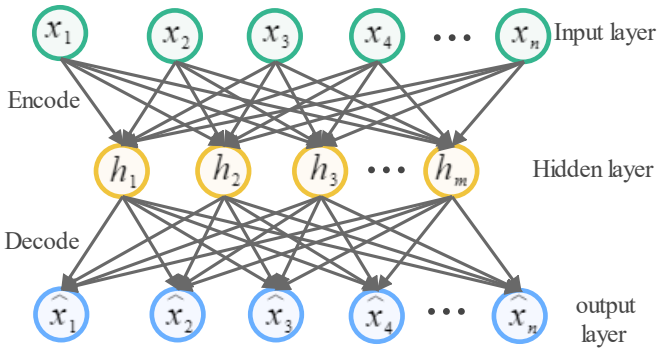

Figure 3: Autoencoder Structure

The first step is to encode the input layer variables into hidden layer variables for dimensionality reduction:

$$H = o(W_1 X + b_1) \tag{10}$$

Where W_1 represents the weight matrix; b_1 represents the bias vector; o represents the activation function; X represents the input layer variables; H represents the hidden layer variables.

Next, the hidden layer variables are decoded back to their original form:

$$\hat{X} = o(W_2 H + b_2) \tag{11}$$

Where W_2 represents the weight matrix; b_2 represents the bias vector; $\hat{X}$ represents the output layer variables.

The formula for calculating reconstruction error is:

$$L(X, \hat{\hat{X}}) = \left\| X - X \right\|_2^2 \tag{12}$$

2.4 Evaluation of Comprehensive Risk Factors Based on EWM-TOPSIS

2.4.1 Weight Calculation Using Entropy Weight Method (EWM)

The entropy weight method (EWM) is an objective weighting algorithm based on information entropy theory [19]. It determines the weights of each indicator based on their information content, thereby avoiding the subjective biases present in subjective weighting methods such as the Analytic Hierarchy Process (AHP), and improving the objectivity and authenticity of evaluation results. The specific steps are as follows.

First, perform indicator normalization. Since the encoded hidden risk indicators are all of the "larger-the-better" type, the inherent process is:

$$p_{ij} = \frac{h_{ij} - \min_i(h_{ij})}{\max_i(h_{ij}) - \min_i(h_{ij})}, i = 1, \cdots, m; j = 1, \cdots, n \tag{13}$$

Where h_{ij} represents the j-th hidden risk indicator of the i-th sample.

Second, calculate the proportion of the i-th sample value under the j-th hidden risk indicator:

$$G_{ij} = \frac{p_{ij}}{\sum_{i=1}^{m} p_{ij}}, i = 1, \cdots, m; j = 1, \cdots, n \tag{14}$$

Third, calculate the entropy value of the j-th hidden risk indicator:

$$\begin{cases} R_j = -e\sum_{i=1}^{m} G_{ij} In(G_{ij}), i = 1,\cdots,m; j = 1,\cdots,n \\ e = In(n) \end{cases} \quad (15)$$

Fourth, calculate the coefficient of variation of the j-th hidden risk indicator:

$$V_j = 1 - R_j, j = 1,\cdots,n \quad (16)$$

Fifth, calculate the weight of the j-th hidden risk indicator:

$$w_j = \frac{V_j}{\sum_{j=1}^{n} V_j}, j = 1,\cdots,n \quad (17)$$

2.4.2 Evaluation of Comprehensive Risk Factors using TOPSIS Method

TOPSIS is an objective comprehensive evaluation method that effectively utilizes the information from the original data to reflect the differences between alternative schemes [20]. In this research, we combine the weights calculated using the Entropy Weight Method (EWM) with TOPSIS to obtain the comprehensive risk factors for pirate attacks. The specific calculation steps are as follows:

$$\frac{p_{ij}}{\sqrt{\sum_{i=1}^{m} p_{ij}^2}}, i = 1,\cdots,m; j = 1,\cdots,n \quad (18)$$

Next, calculate the positive ideal solution and the negative ideal solution:

$$\begin{cases} Z^+ = (z_1^+, z_2^+, \cdots, z_n^+) \\ z_j^+ == \max_i (z_{ij}), i = 1,\cdots,m; j = 1,\cdots,n \end{cases} \quad (19)$$

$$\begin{cases} Z^- = (z_1^-, z_2^-, \cdots, z_n^-) \\ z_j^- = \min_i (z_{ij}), i = 1,\cdots,m; j = 1,\cdots,n \end{cases} \quad (20)$$

Furthermore, calculate the distances from each sample to the positive ideal solution and the negative ideal solution:

$$D_i^+ = \sqrt{\sum_{j=1}^{n} w_j \left(Z_j^+ - z_{ij}\right)^2}, i = 1,\cdots,m \quad (21)$$

$$D_i^- = \sqrt{\sum_{j=1}^{n} w_j \left(Z_j^- - z_{ij}\right)^2}, i = 1,\cdots,m \quad (22)$$

Finally, calculate the comprehensive risk factor:

$$S_i = \frac{D_i^-}{D_i^+ + D_i^-}, i = 1,\cdots,m \quad (23)$$

Where S_i represents the comprehensive risk factor of the *i*-th pirate attack incident.

2.5 Geographical Distribution Simulation and Prediction of Comprehensive Risk Factors Based on Nearest Neighbor Interpolation

Nearest neighbor interpolation is a simple yet effective interpolation algorithm. For a given target location, the algorithm identifies the closest data point from a set of known data points and uses its value as the interpolation result [21]. In this research, we assume the maritime area is divided into $s \times s$ grid points, resulting in a total of N grid points. Using the comprehensive risk factors from known pirate attack locations, we estimate the comprehensive risk factors for each grid point through nearest neighbor interpolation. This approach allows us to simulate and predict the geographical distribution of pirate attack risks within the maritime area.

III. RESULTS

3.1 Dataset

The data for this research is sourced from the GISIS pirate attack incident database, which provides statistics on the number of global pirate attacks from 2006 to 2022 (as shown in Figure 4). It is evident that East Africa, West Africa, the Arabian Sea, and the Strait of Malacca are hotspots for pirate attacks. Specifically, there were 283 incidents in East Africa, 647 in West Africa, 910 in the Arabian Sea, and 518 in the Strait of Malacca. Consequently, these four maritime regions were selected as the focus of our research to evaluate the risk of pirate attacks and to simulate and predict their geographical distribution.

Additionally, the original pirate attack data is highly fragmented. Through further data

preprocessing and natural language processing (including tokenization, stop word removal, lemmatization, and keyword extraction), we extracted the necessary information such as latitude and longitude, number of pirates, weapon details, and loss data for quantifying the risk indicators of pirate attacks.

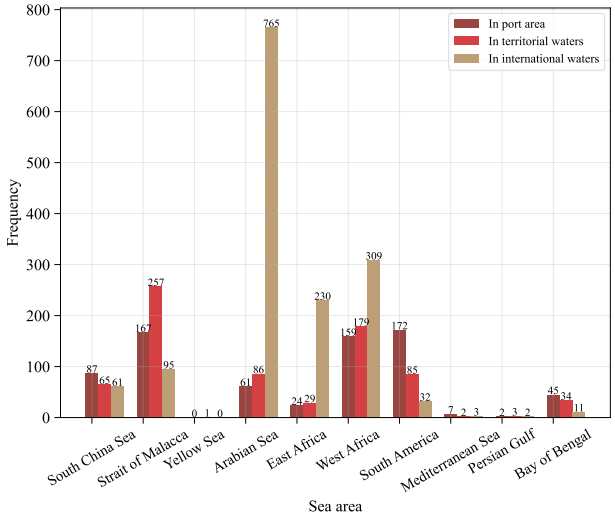

Figure 4: Statistics on the Number of Piracy Incidents in Various Sea Areas

3.2 Classification Results of Central Areas

The determination of the number of central areas k is the basis for conducting the K-means clustering algorithm to partition the pirate attack incidents. The variation of the Sum of Squared Errors (SSE) with different numbers of central zones is shown in Figure 5. It can be observed that SSE decreases as the number of central areas increases. When k exceeds 3, the downward trend of the SSE curve for each region slows down. This point is considered as the "elbow point", indicating the optimal number of clusters. Therefore, in this research, the number of central zones for each maritime areas is set to 3.

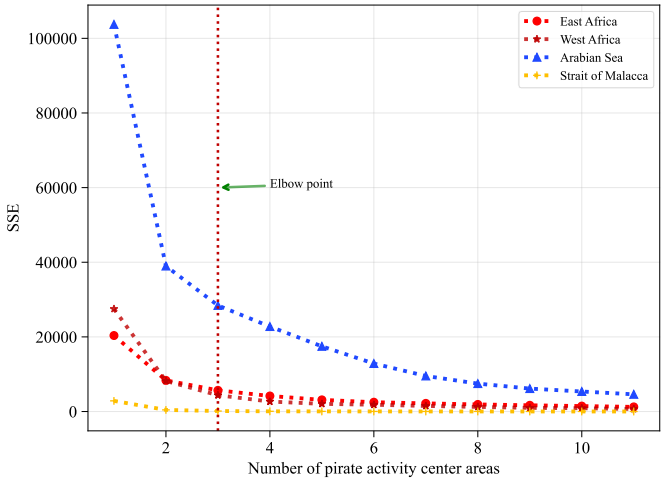

Figure 5: SSE changes in the Number of Central Areas for Different Pirate Attacks

After determining the number of central zones for each maritime region, the K-means clustering algorithm is applied to partition each pirate attack incident into the respective pirate activity center zones (as shown in Figure 6). It can be observed that pirate attack incidents exhibit a certain degree of clustering. The majority of pirate attack incident locations are relatively close to their cluster centroids, indicating the effectiveness of clustering to some extent. Subsequently, the

maritime regions are divided into a total of 400 grid points (20×20 grid), and each grid point is assigned to its respective pirate activity center zone using the trained K-means clustering model.

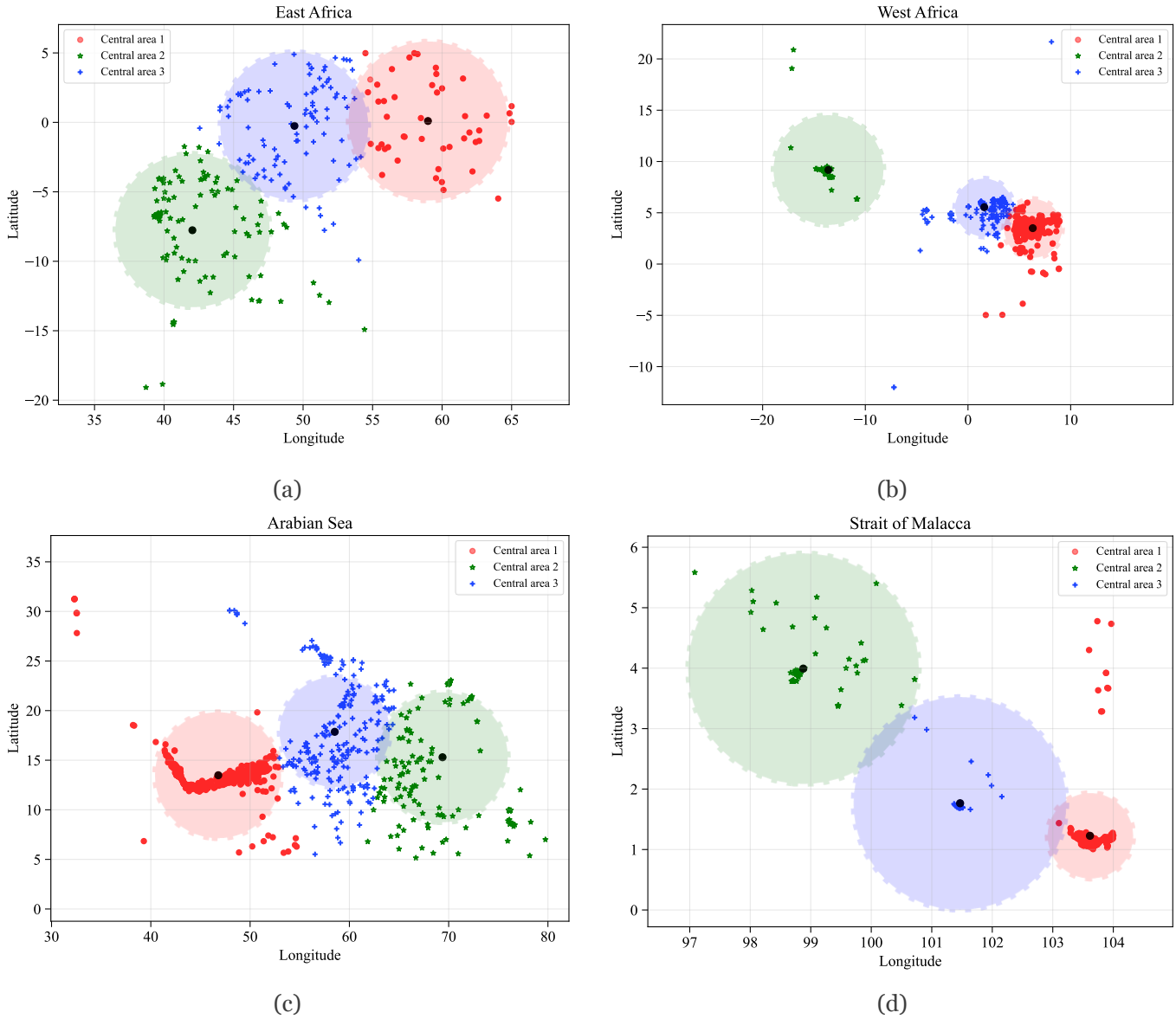

Figure 6: Clustering results of pirate attacks: (a) East Africa, (b) west Africa, (c) Arabian Sea, and (d) Strait of Malacca

3.3 Results of Geographical Probability Factor for Pirate Attack Incidents

Based on the K-means clustering results and the latitude and longitude information of each pirate attack incident, the time hyperparameter t is set to 0.02. Using the proposed algorithm, we can determine the geographical probability factor for pirate incidents at each grid point across different regions. The results are shown in Figure 7. It demonstrates a significant similarity between the geographical probability factor distribution generated by our algorithm and the actual distribution of pirate attack incident locations. This finding strongly suggests that the proposed algorithm effectively captures and measures the geographical distribution patterns of pirate attack incidents.

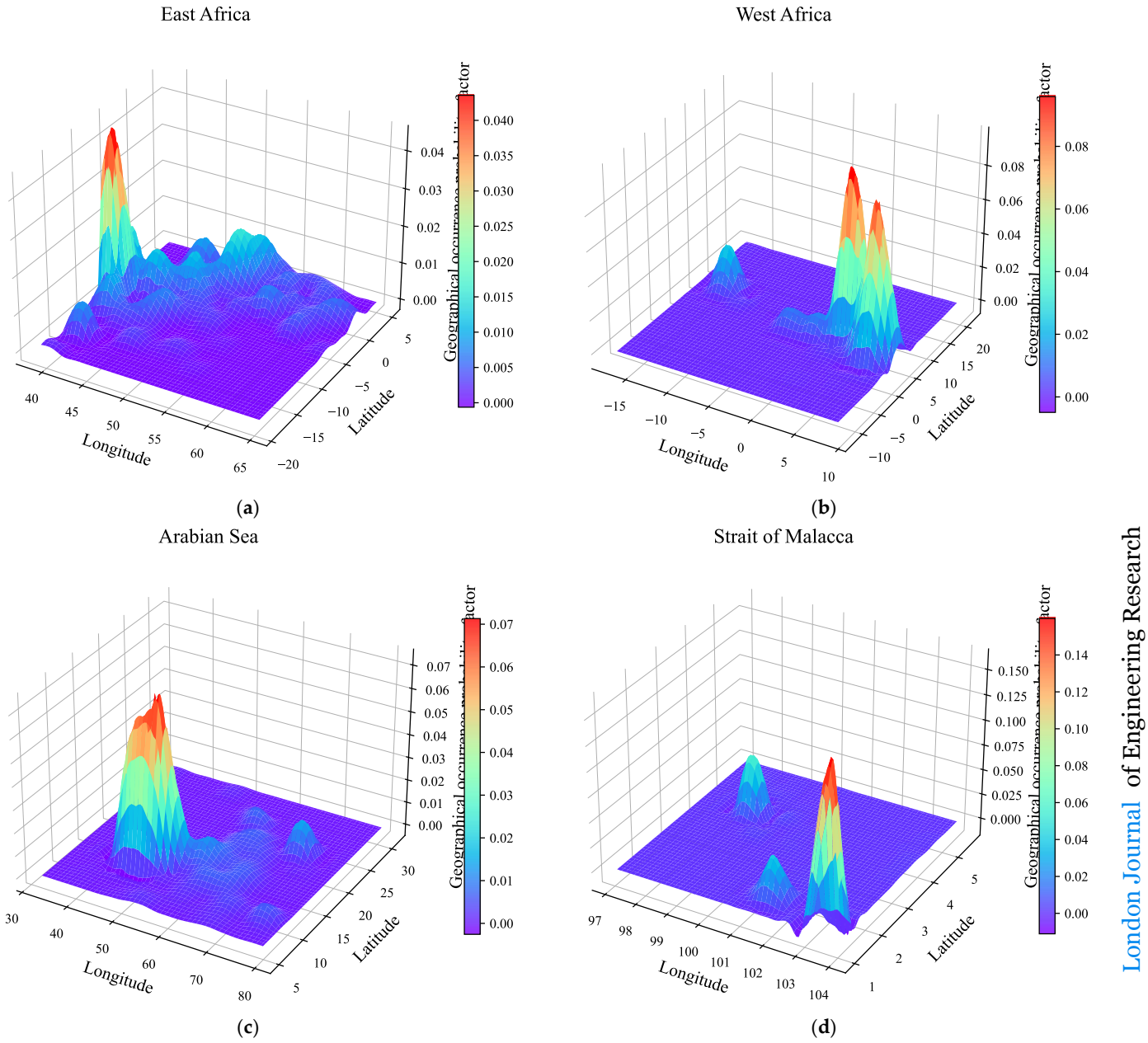

Figure 7: Distribution of geographical probability factors for piracy incidents in various sea areas: (a) East Africa, (b) west Africa, (c) Arabian Sea, and (d) Strait of Malacca

3.4 Results of Indicator Encoding

The Autoencoder model constructed in this research has 5 neurons in the input layer, 3 neurons in the hidden layer, and 5 neurons in the output layer, with Leaky ReLU as the activation function. During the training process of the Autoencoder, the Adam optimizer is used, with a first-order momentum hyperparameter of 0.9, a second-order momentum hyperparameter of 0.999, an initial learning rate of 0.001, 100 training epochs, and a batch size of 4. The training results are shown in Figure 8. the reconstruction error continuously decreases during the training process. This indicates that the model progressively extracts key information from the raw data, enabling the hidden layer variables to more effectively capture the features and structure of the data.

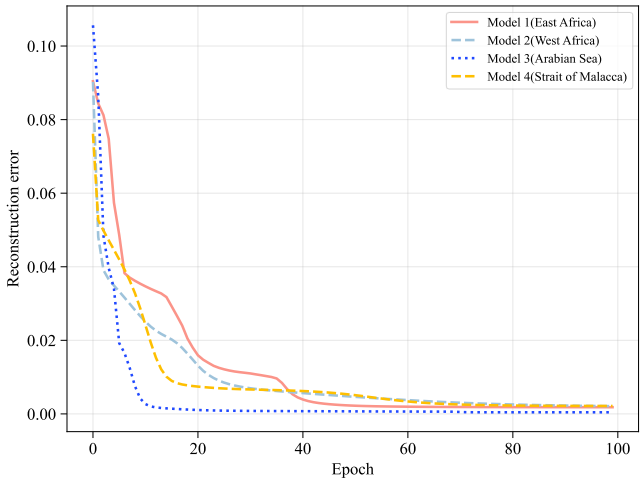

Figure 8: Reconstruction Error Results of Each Model Training

Using the Autoencoder, we encode and learn the representations of four risk indicators: the geographical probability factor of pirate incidents, the number of pirates score, the weapon equipment score, and the loss score. The encoded risk indicators' results are shown in Figure 9. It shows that the risk indicators encoded by the Autoencoder model exhibit more regular distribution characteristics, resembling a step-like distribution. This allows for more effective representation of the risk information associated with each pirate attack incident, facilitating subsequent comprehensive risk evaluation and analysis.

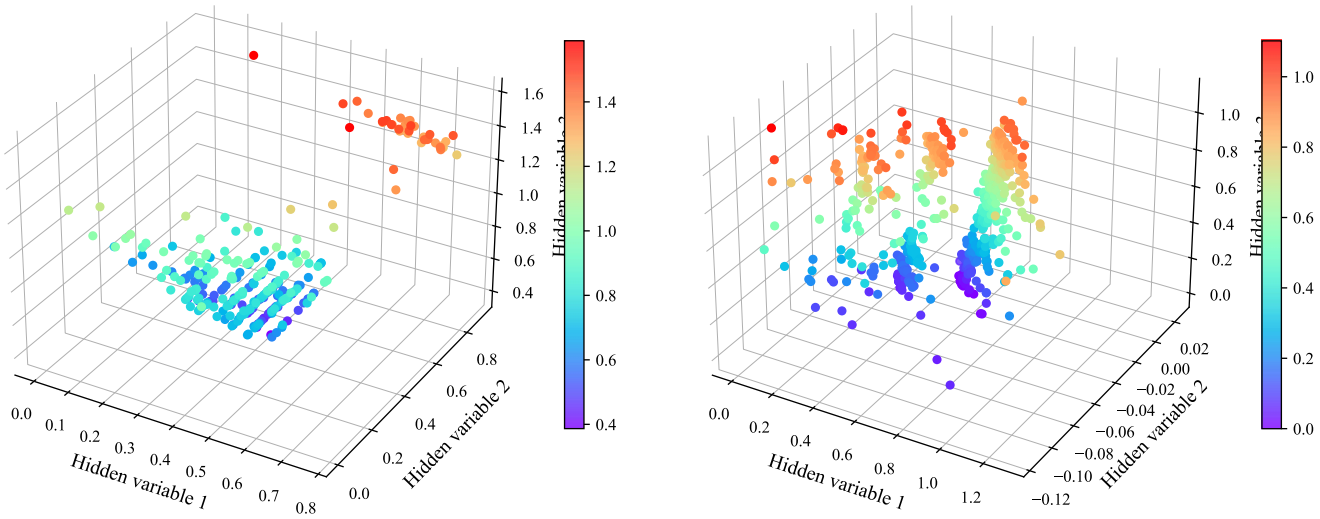

(a) (b)

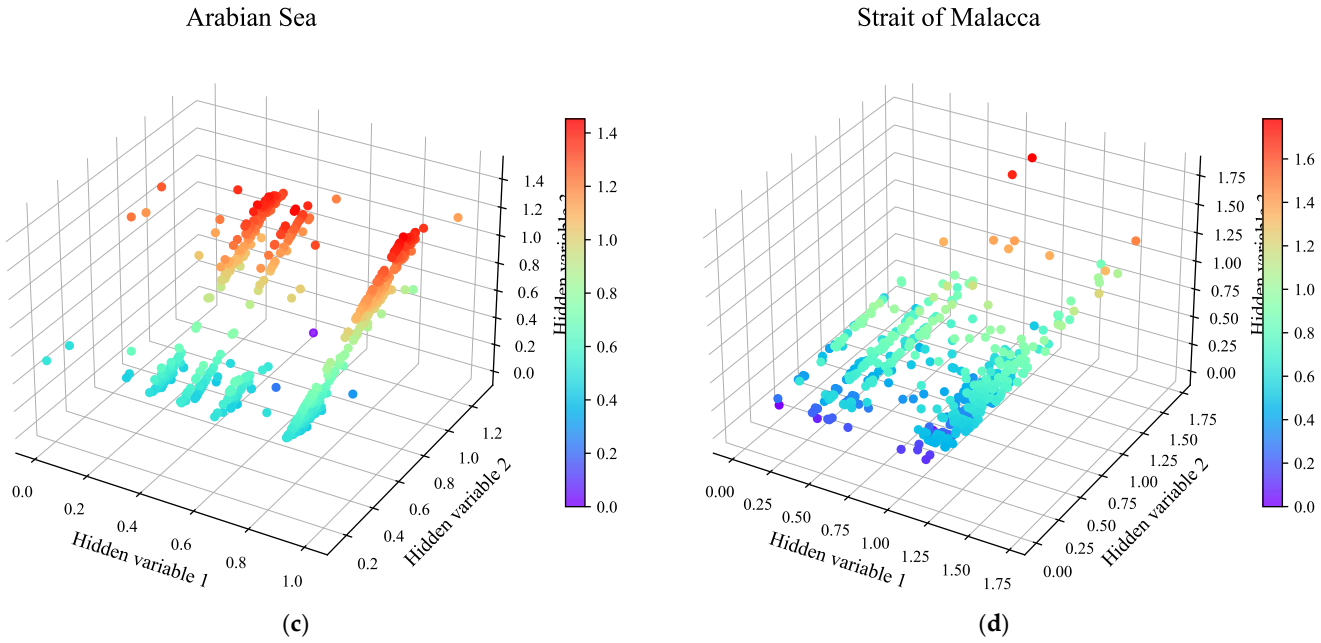

Figure 9: Visualization results of hidden variable characteristics in each sea area: (a) East Africa, (b) west Africa, (c) Arabian Sea, and (d) Strait of Malacca

3.5 Comprehensive Risk Factor Evaluation Results and Comparative Analysis

Using the EWM-TOPSIS method, we scored the hidden risk indicators for each pirate attack incident to obtain the final comprehensive risk factors. Additionally, we compared these results with those obtained using the commonly used Entropy Weight Method combined with Grey Relational Evaluation (EWM-GRE) to analyze the differences between the scoring results. As shown in Figure 10, the EWM-TOPSIS method and EWM-GRE present similar results for the comprehensive risk evaluation of the same pirate attack incidents. However, the EWM-TOPSIS method proves to be more effective in distinguishing the differences between the comprehensive risk factors of various pirate attack incidents.

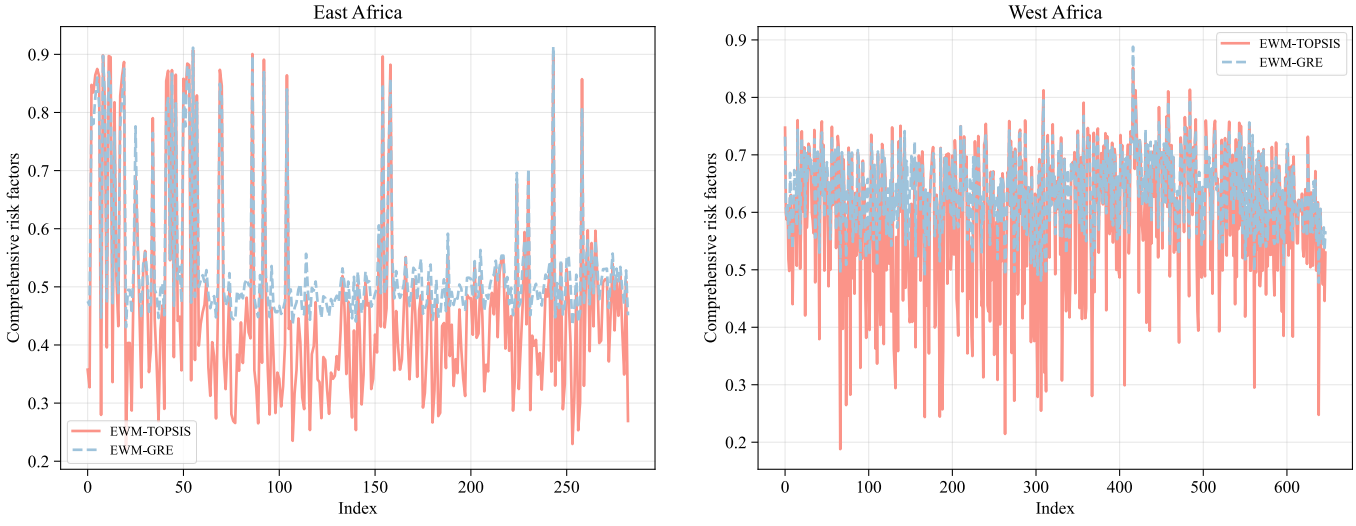

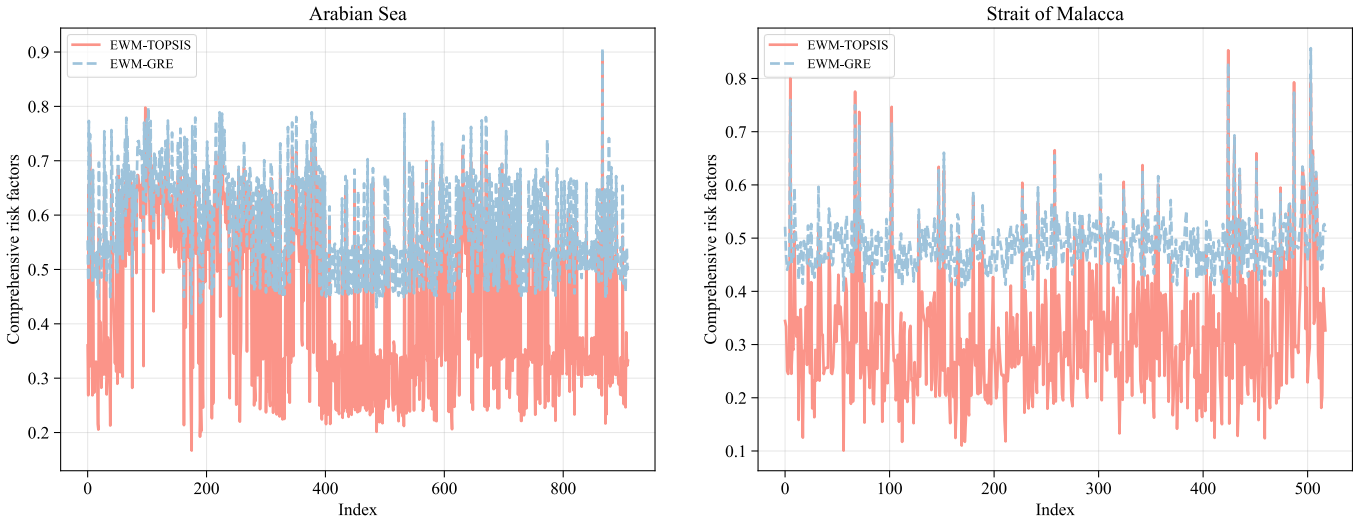

(c) (d)

Figure 10: Analysis of evaluation results of different models in each sea area: (a) East Africa, (b) west Africa, (c) Arabian Sea, and (d) Strait of Malacca

3.6 Simulated Geographical Distribution of Comprehensive Risk Factors

After obtaining the comprehensive risk factors for each pirate attack incident, we further refined the maritime area into a total of 40,000 grid points to achieve more precise geographical risk distribution. Using nearest neighbor interpolation, we simulated and predicted the distribution of comprehensive risk factors across different maritime regions, as shown in Figure 11.

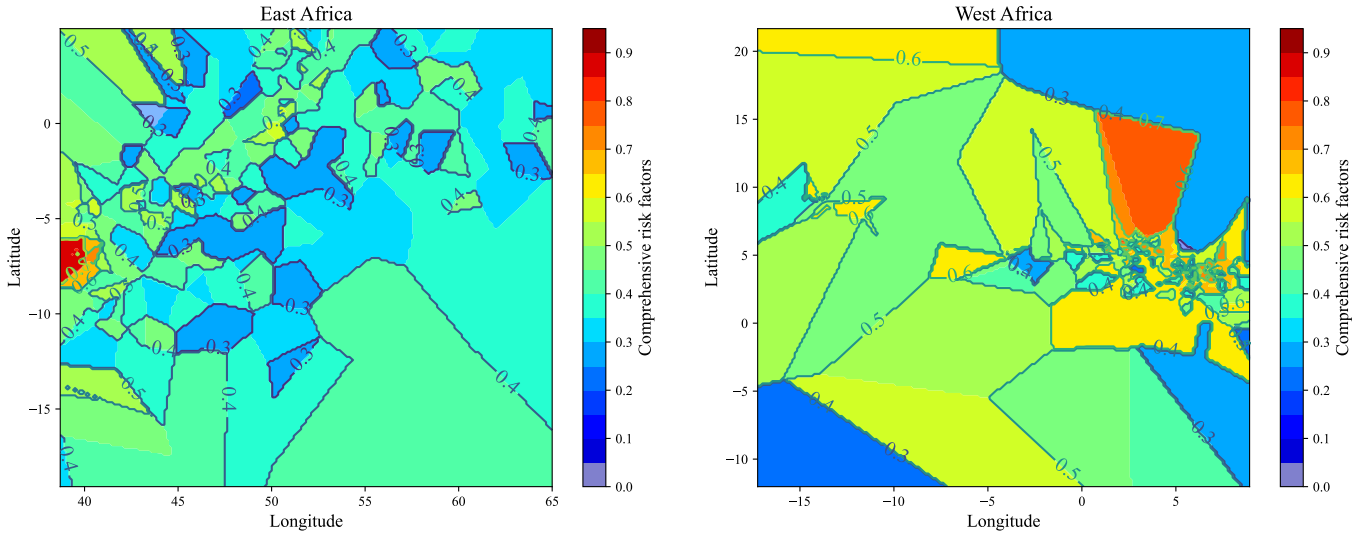

(a) (b)

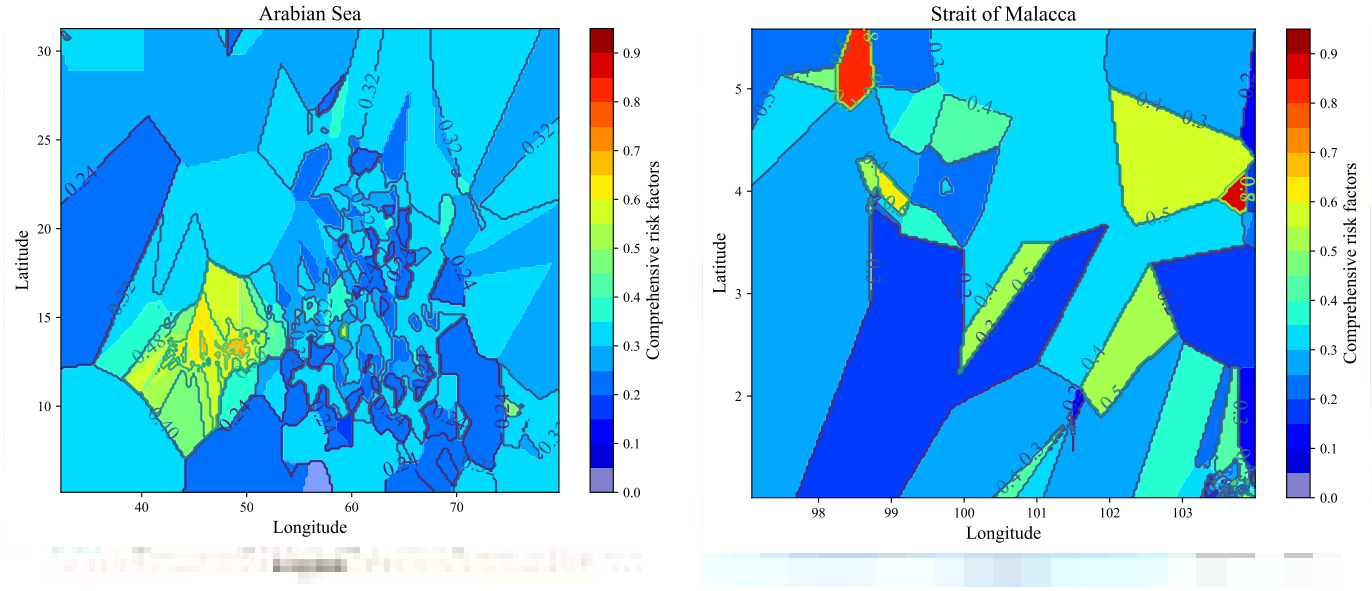

Figure 11: Simulation prediction results of comprehensive risk factor distribution in each sea area:(**a**) East Africa, (**b**) west Africa, (**c**) Arabian Sea, and (**d**) Strait of Malacca.

According to the predicted comprehensive risk factor distribution in Figure 11, the risk of pirate attacks is high in the East African region at 39°E-42°E, 6°S-8°S. In the West African region, the area between 3°E-5°E and 6°N-15°N shows a higher risk of pirate attacks. The Arabian Sea (45°E-70°E, 5°N-15°N) displays significant risks, characterized by an irregular and highly fragmented risk distribution pattern. The Malacca Strait (103°E-104°E, 1°N-2°N) has a very high risk of pirate attacks in certain areas.

In summary, the algorithm proposed in this research successfully simulates and predicts the distribution of comprehensive risk factors for pirates in different maritime areas. These results provide valuable reference information for ship route planning, helping to reduce the risk of pirate attacks and offering broad potential and benefits in practical applications.

IV. DISCUSSION

This paper presents a spatiotemporal feature-based pirate attack risk assessment model, which successfully simulates and predicts the comprehensive risk distribution across different maritime regions. First, by incorporating the spatiotemporal distribution characteristics of pirate attacks, we employ the K-means clustering algorithm to delineate key pirate activity center zones. This allows the construction of a geographical probability factor that captures spatiotemporal feature information, serving as a critical indicator for risk assessment. Additionally, natural language processing techniques are used to further extract and quantify three key pirate attack risk indicators: the number of pirates, weaponry score, and loss score.

Subsequently, an Autoencoder is utilized to encode these risk indicators, resulting in a more structured, step-like distribution of the data, which effectively enhances the representation of pirate attack risk information and improves the accuracy of subsequent risk assessments. Finally, a comprehensive evaluation of pirate attack risks is conducted using the Entropy Weight Method (EWM) combined with the Technique for Order Preference by Similarity to Ideal Solution (TOPSIS), allowing for a precise analysis of risk.

The experimental results demonstrate that the proposed model not only accurately captures the geographical distribution patterns of pirate attacks but also effectively differentiates the risk levels across various pirate incidents. Through a comparative analysis with the EWM-GRE model, the EWM-TOPSIS method shows superior performance in distinguishing risk variations among different pirate attacks. Based on these findings, the nearest neighbor interpolation

method was applied to simulate and predict the comprehensive risk of pirate attacks in four key maritime regions: East Africa, West Africa, the Arabian Sea, and the Strait of Malacca. These results provide valuable reference points for safe route planning in maritime navigation.

This study proposes a pirate attack risk assessment model based on spatiotemporal feature analysis, providing valuable practical references for maritime route planning. First, the study simulates and predicts the distribution of pirate attack risks in four key maritime regions: East Africa, West Africa, the Arabian Sea, and the Strait of Malacca. Based on these precise risk prediction results, shipping companies and vessels can develop safer routes to avoid high-risk areas, thereby effectively reducing the likelihood of pirate attacks. Additionally, the study integrates four critical risk indicators—geographical probability factor, number of pirates, weaponry score, and loss score—offering a comprehensive evaluation of pirate attack risks. This holistic assessment approach significantly enhances the identification and classification of pirate attack risks, enabling governments and international maritime organizations to formulate more accurate preventive measures. By helping the shipping industry mitigate economic losses and improve maritime safety, this model also contributes to the stability and development of global trade.

This study also has certain limitations. First, due to the constraints of the dataset used, only four pirate attack risk indicators were quantified: the geographical probability factor, the number of pirates, the weaponry score, and the loss score. In the future, the exploration of additional pirate attack datasets could enable the extraction of more potential risk indicators, thereby providing more comprehensive data support for subsequent risk assessments.Second, while current neural network models possess strong feature extraction capabilities, their internal mechanisms remain difficult to interpret. In this study, an Autoencoder was used for feature encoding, resulting in a more orderly step-like distribution of the data. However, this method still falls short in explaining the underlying mechanisms of pirate attack risk information, necessitating further research to validate and improve its effectiveness.Finally, the study employed the Nearest Neighbor Interpolation algorithm to simulate the comprehensive risk distribution of pirate attacks across different maritime regions. While this algorithm offers simplicity and high computational efficiency, particularly in scenarios requiring large-scale, real-time risk prediction, it relies solely on the nearest data point. This can lead to discontinuities or abrupt changes at boundary areas, resulting in unrealistic risk distribution gaps. Additionally, the Nearest Neighbor Interpolation method may overlook the potential spatial gradient of pirate attack risks, thus impacting the smoothness and global consistency of the prediction results.

In future research, we plan to first collect and expand the dataset of pirate attack incidents to extract and quantify additional risk indicators, aiming to achieve a more comprehensive and accurate assessment of pirate attack risks. Second, we will delve deeper into the application mechanisms of Autoencoders in feature encoding, analyzing how they produce more orderly, step-like distribution characteristics in the data to enhance the model's interpretability. Third, we will optimize the current interpolation algorithms, focusing on addressing the issues of smoothness and global consistency that arise from using the Nearest Neighbor Interpolation algorithm in the simulation and prediction of comprehensive pirate attack risks. Finally, based on the simulated and predicted comprehensive risk results, we plan to develop a targeted ship route planning system, providing more scientifically informed guidance for the safe navigation of vessels.

V. CONCLUSIONS

The algorithm proposed in this paper effectively captures and measures the geographical distribution patterns of pirate attacks, demonstrating significant similarity to actual occurrences. The main findings and contributions of this research are summarized as follows:

1. Construction of Spatiotemporal Feature Characteristics: By employing the K-means clustering algorithm and introducing the

geographical probability factor, we fully account for the spatiotemporal distribution characteristics of pirate activities, laying a solid foundation for subsequent risk assessment;

2. Enhanced Data Representation: The data processed through the Autoencoder for dimensionality reduction exhibit more structured distribution characteristics, enabling more effective representation of the risk information associated with each pirate attack incident;
3. Effective Risk Assessment: The use of EWM-TOPSIS effectively measures the risk of pirate attacks, facilitating a finer and more accurate differentiation of risk variations between different pirate attack incidents;
4. Geographical Risk Prediction: The algorithm proposed in this paper effectively simulates and predicts the distribution of comprehensive risk factors of piracy across various maritime regions. These simulation results provide crucial reference information for maritime route planning, aiding in the mitigation of piracy attack risks. The prediction of comprehensive risk factors indicates that piracy attack risks are higher in certain areas of the East African maritime region (39°E-42°E, 6°S-8°S) and the Strait of Malacca (103°E-104°E, 1°N-2°N). Additionally, certain areas of the West African maritime region (3°E-5°E, 6°N-15°N) show elevated risks, while the Arabian Sea (45°E-70°E, 5°N-15°N) exhibits significant and irregularly distributed piracy attack risks. This algorithm demonstrates extensive potential and advantages in practical applications.

Funding: This research was funded by Zhejiang Provincial Public Welfare Project of China under Grant No. LGG22E090004, Zhejiang Provincial Natural Science Foundation of China under Grant number LQ21E090006.

Institutional Review Board Statement: Not applicable.

Informed Consent Statement: Not applicable.

Conflicts of Interest: The authors declare no conflicts of interest.

REFERENCES

1. Grzelakowski, A. S.; Herdzik, J.; Skiba, S. Maritime shipping decarbonization: Roadmap to meet zero-emission target in shipping as a link in the global supply chains. *Energies 2022*, *15*, 6150. https://doi.org/10.3390/en15176150.
2. Ehizuelen, M. M. O. Assessing the national and regional effectiveness of countering maritime piracy in the Gulf of Guinea. *GeoJournal 2023*, *88*, 3549-3574. https://doi.org/10.1007/s10708-022-10823-0.
3. Robitaille, M. C. Maritime piracy and international trade. *Defence Peace Econ. 2020*, *31*, 957-974. https://doi.org/10.1080/10242694.2019.1627511.
4. Nwalozie, C. J. Exploring contemporary sea piracy in Nigeria, the Niger Delta and the Gulf of Guinea. *J. Transp.Secur. 2020*, *13*, 159-178. https://doi.org/10.1007/s12198-020-00218-y.
5. Denton, G. L.; Harris, J. R. Maritime piracy, military capacity, and institutions in the Gulf of Guinea. *Terror. Polit. Violenc. 2022*, *34*, 1-27. https://doi.org/10.1080/09546553.2019.1659783.
6. Regan, J. Varied Incident Rates of Global. *Int. Crim. Justice Rev. 2022, 32*, 374-387. https://doi.org/10.1177/1057567720944448.
7. Jiang, M.; Lu, J. The analysis of maritime piracy occurred in Southeast Asia by using Bayesian network. Transport.*Res. E-log. 2020*, *139*, 101965. https://doi.org/10.1016/j.tre.2020.101965.
8. Fan, H.; Lu, J.; Chang, Z.; Ji, Y. A Bayesian network-based TOPSIS framework to dynamically control the risk of maritime piracy. *Marit. Policy Manag. 2023,* 1-20. https://doi.org/10.1080/03088839.2023.2193585.
9. Dabrowski, J. J.; De Villiers, J. P. Maritime piracy situation modelling with dynamic Bayesian networks. *Inform. Fusion 2015, 23*, 116-130.https://doi.org/10.1016/j.inffus.2014.07.001.
10. Gong, X.; Jiang, H.; Yang, D. Maritime piracy risk assessment and policy implications: A two-step approach. *Mar. Policy 2023, 150*, 105547. https://doi.org/10.1016/j.marpol.2023.105547.

11. Vaněk, O.; Jakob, M.;Hrstka, O.; Pěchouček, M. Agent-based model of maritime traffic in piracy-affected waters. *Transport.Res. C-emer. 2013, 36*, 157-176. https://doi.org/10.1016/j.trc.2013.08.009.
12. Jin, M.; Shi, W.; Lin, K. C.; Li, K. X. Marine piracy prediction and prevention: Policy implications. *Mar. Policy 2019*, *108*, 103528. https://doi.org/10.1016/j.marpol.2019.103528.
13. Pristrom, S.; Yang, Z.; Wang, J.; Yan, X. A novel flexible model for piracy and robbery assessment of merchant ship operations. *Reliab. Eng. Syst. Safe. 2016, 155*, 196-211. https://doi.org/10.1016/j.ress.2016.07.001.
14. Daxecker, U.; Prins, B. C. Financing rebellion: Using piracy to explain and predict conflict intensity in Africa and Southeast Asia. *J. Peace Res. 2017, 54*, 215-230. https://doi.org/10.1177/0022343316683436.
15. Govender, P.; Sivakumar, V.; Application of k-means and hierarchical clustering techniques for analysis of air pollution: A review (1980–2019). *Atmos pollut. Res. 2020*, *11*, 40-56. https://doi.org/10.1016/j.apr.2019.09.009.
16. Wang, Y.; Yao, H.; Zhao, S.; Zheng, Y.E.F.Dimensionality reduction strategy based on auto-encoder. Proceedings of the 7th International Conference on Internet Multimedia Computing and Service, Zhangjiajie, Hunan, China, 19-21 August2015. https://doi.org/10.1145/2808492.2808555.
17. Demšar, U.; Harris, P.; Brunsdon, C.; Fotheringham, A. S.; McLoone, S. Principal component analysis on spatial data: an overview. *Annals of the Association of American Geographers 2013, 103*, 106-128. https://doi.org/10.1080/00045608.2012.689236.
18. Yong, A. G.; Pearce, S. A beginner's guide to factor analysis: Focusing on exploratory factor analysis. *Tutorials in quantitative methods for psychology*, *2013*, *9*, 79-94. https://doi.org/10.20982/tqmp.09.2.p079.
19. Li, Z.; Luo, Z.; Wang, Y.; Fan, G.; Zhang, J. Suitability evaluation system for the shallow geothermal energy implementation in region by Entropy Weight Method and TOPSIS method. *Renew. Energ. 2022, 184*, 564-576. https://doi.org/10.1016/j.renene.2021.11.112.
20. Torkayesh, A. E.; Deveci, M.; Karagoz, S.;Antucheviciene, J. A state-of-the-art survey of evaluation based on distance from average solution (EDAS): Developments and applications. *Expert Syst. Appl. 2023, 221*, 119724. https://doi.org/10.1016/j.eswa.2023.119724.
21. Ni, K. S.; Nguyen, T. Q. An adaptable *k*-nearest neighbors algorithm for MMSE image interpolation. *IEEE T.Image Process. 2009*, *18*, 1976-1987. https://doi.org/10.1109/TIP.2009.2023706.

FEA Modelling of the Aluminium Alloy Graphene-Based Composite Plate for the Launch Vehicle External Fuel Tank Structural Application

Mr. Neeraj Gopichand Salunkhe

ABSTRACT

The primary aim of this research is to investigate the structural uses of an aluminium alloy with a composite plate made of graphene in launch vehicle fuel tanks. To evaluate the viability and performance of the composite plate in this application, finite element analysis (FEA) modelling is used. The study aims to analyse the composite plate's mechanical behaviour, thermal characteristics, and structural integrity under various loading scenarios, such as mechanical and thermal loads, stress, and strain. The outcomes of the FEA model are compared with the materials currently used in the external fuel tanks of launch vehicles. A cost analysis of the production process is also carried out to determine whether using the graphene-based composite plate is economically feasible. The study intends to provide light on the benefits, difficulties, and constraints related to the structural components of launch vehicle fuel tanks made of graphene-based composites.

Keywords: finite element analysis (FEA), carbon nanotubes (CNT), liquid oxygen (LOX), liquid hydrogen (LH2), external fuel tank (EFT).

Classification: DDC Code: 620

Language: English

Great Britain Journals Press

LJP Copyright ID: 392954
Print ISSN: 2631-8474
Online ISSN: 2631-8482

London Journal of Engineering Research

Volume 24 | Issue 7 | Compilation 1.0

FEA Modelling of the Aluminium Alloy Graphene-Based Composite Plate for the Launch Vehicle External Fuel Tank Structural Application

Mr. Neeraj Gopichand Salunkhe

ABSTRACT

The primary aim of this research is to investigate the structural uses of an aluminium alloy with a composite plate made of graphene in launch vehicle fuel tanks. To evaluate the viability and performance of the composite plate in this application, finite element analysis (FEA) modelling is used. The study aims to analyse the composite plate's mechanical behaviour, thermal characteristics, and structural integrity under various loading scenarios, such as mechanical and thermal loads, stress, and strain. The outcomes of the FEA model are compared with the materials currently used in the external fuel tanks of launch vehicles. A cost analysis of the production process is also carried out to determine whether using the graphene-based composite plate is economically feasible. The study intends to provide light on the benefits, difficulties, and constraints related to the structural components of launch vehicle fuel tanks made of graphene-based composites. The results of this study have the potential to advance the discipline of aeronautical engineering and establish the framework for upcoming advances in materials science and design optimisation for launch vehicle applications.

Keywords: finite element analysis (FEA), carbon nanotubes (CNT), liquid oxygen (LOX), liquid hydrogen (LH2), external fuel tank (EFT).

Author: MSc Automotive Engineering FH116, Fortress House, CV1 1GF.

I. INTRODUCTION

The aerospace sector is continually looking for novel ways to improve the effectiveness and performance of launch vehicles. To retain structural integrity during launch and space missions, fuel tanks, as a crucial component of these vehicles, require materials that can withstand extreme conditions. Due to its remarkable mechanical qualities, lightweight, and thermal conductivity, graphene-based composites have recently attracted increasing interest in aircraft applications. Finite element analysis (FEA) modelling is the primary study tool to examine the viability of utilising an aluminium alloy with a graphene-based composite plate for structural applications in the fuel tanks of launch vehicles.[1]

The materials currently used to build fuel tanks for launch vehicles have limitations, including weight, corrosion resistance, and mechanical qualities. To overcome these obstacles and deliver improved performance, it is necessary to investigate new materials and technologies. It offers enormous promise to improve structural grades to incorporate graphene, a two-dimensional carbon material, into an aluminium alloy matrix. Graphene has remarkable mechanical, thermal, and electrical properties. This study's primary objective is to evaluate the viability of using a composite plate made of graphene and aluminium for the structural use of fuel tanks in launch vehicles. This study uses FEA modelling to assess the suggested composite material's mechanical behaviour, performance, and durability under various situations, such as heat loads, mechanical stresses, and strain.[2]

This research involves a comprehensive literature review on the FEA modelling of aluminium alloys with graphene-based composites for aerospace structural applications. The study consists of developing a model utilising the FEA technique and validating it against experimental data to ensure accuracy and dependability. Numerous analyses will evaluate the composite material's performance under various loading conditions, including thermal, stress, and strain studies.

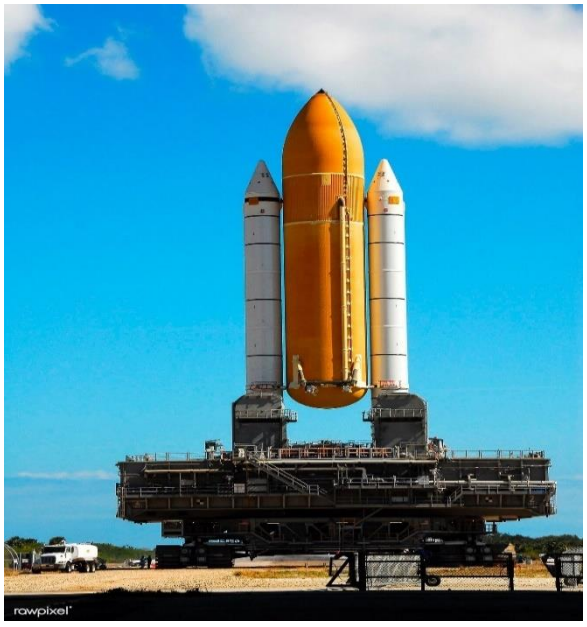

Figure 1: External Fuel Tank of Launch Vehicle Photograph from Pinterest, July 18, 2019, USA[3]

The novel concept of this research is the incorporation of graphene-based composites into the structural design of launch vehicle fuel containers. This novel approach can significantly enhance strength, weight reduction, and corrosion resistance compared to conventional materials. In addition, FEA modelling provides a cost-effective and efficient method for evaluating the feasibility and performance of the proposed composite material before conducting physical tests.

1.1 Problem Description

Launch vehicles are crucial to space exploration, requiring high-performance materials that withstand extreme conditions. Their materials limit the launch vehicle fuel tank's weight, strength, and thermal stability. The above considerations have prompted studying alternate materials that might increase launch vehicle efficiency and safety.

Due to its strength-to-weight ratio, aero planes use aluminium alloys extensively. However, modern space travel requires materials with remarkable properties beyond ordinary alloys. Graphene-based composites' mechanical, thermal, and electrical characteristics make them intriguing materials. Graphene in aluminium alloys may improve launch vehicle fuel tanks. However, this idea raises essential questions. The structural usage of an aluminium alloy and a graphene-based composite plate in launch vehicle fuel tanks is complex and requires a detailed investigation. The modelling and assessment of composite materials under various conditions might benefit from Finite Element Analysis (FEA) models. However, several criteria must be considered to successfully implement this revolutionary material notion. In space exploration, launch vehicles need innovative materials to survive harsh temperatures and operate well. Current launch vehicle exterior fuel tank materials are limited in weight, strength, and thermal stability. This has led to researching alternate materials that may improve launch vehicle efficiency and safety.

The strength-to-weight ratio of aluminium alloys makes them popular in aircraft. However, contemporary space exploration requires materials with superior qualities to previous alloys. Due to their mechanical, thermal, and electrical properties, graphene-based composites seem promising. Incorporating graphene into aluminium alloys might improve launch vehicle fuel tanks, but it poses numerous essential problems.

The viability of using an aluminium alloy and a graphene-based composite plate for launch vehicle fuel tank structural purposes is complex and requires more research. To simulate and evaluate these composite materials under different situations, Finite Element Analysis (FEA) modelling is helpful. To apply this innovative material idea successfully, many factors must be addressed.

1.2 Project Aim

Investigation of the feasibility of using aluminium alloy with a graphene-based composite plate for structural application in the fuel tanks of launch vehicles through FEA modelling.

1.3 Project Objectives

- Literature review of FEA modelling of the aluminium alloy with a graphene-based composite plate for the launch vehicle external fuel tank structural application.
- Developing a model and validating it against experimental data.
- Analysing composite plates under various conditions such as thermal, mechanical loads, stress and strain, etc.
- Analysing the external fuel tank of the launch vehicle under various conditions.
- Comparing results with the current material used for the external tank of the launch vehicle.
- Identifying any challenges or limitations.

II. LITERATURE REVIEW

2.1 Material

- Aluminium metal matrix composites (MMCs) have been thoroughly researched for wear across several operating settings. The authors examined how average load, sliding velocity, sliding distance, and reinforcements impact the composite's wear rate and coefficient of friction (COF). Delamination, adhesive wear, abrasive wear, and fretting are well-studied. Stir casting, powder metallurgy, and friction stir processing have produced aluminium MMCs. Production methods depend on composite material qualities. Stir casting is inexpensive, but friction stir processing increases microstructural and mechanical characteristics. Pin-on-disc wear experiments measured aluminium MMCs' wear rate and COF. SEM examined the worn surface's shape and causes.[4]
- Powder metallurgy, stir casting, and squeeze casting have been studied to distribute 2D graphene nanoplatelets into the matrix uniformly. The hardness, tensile strength, and ductility of Metal Matrix Composites (MMCs) are significantly affected by 2D–graphene nanoplatelets dispersion. The proper distribution of 2D-graphene nanoplatelets can increase grain refinement and stable intermetallic phases, improving metal matrix composite's (MMCs) mechanical properties.[5]
- Multiple investigations have investigated the effects of graphene incorporation into an aluminium matrix. It has been observed that incorporating graphene improves the composite's mechanical properties up to a certain point. Among the reinforcement mechanisms are effective load transfer via Orowan looping of nanoparticles, load transfer from the aluminium matrix to graphene, dislocation strengthening due to coefficient mismatch, and grain refinement. Several fabrication techniques have been investigated, with powder metallurgy being the most common technique for obtaining a decent graphene dispersion within the matrix.[6]

- Despite mechanical exfoliation and chemical reduction, graphene with outstanding properties is still challenging to produce. Authors found that nanocomposites using graphene fillers have higher modulus and tensile strength. Graphene fillers' distribution inside the polymer matrix has also been an issue, driving research to optimise interfacial interactions and achieve homogenous dispersion to reduce agglomeration. To make graphene nanocomposites, researchers have used several methods. To improve graphene compatibility with the polymer matrix, functionalisation is often used. Hybrid fillers, which combine graphene with other nanomaterials like carbon nanotubes or metal oxides, have also been studied to solve graphene's specific restrictions and achieve customisable characteristics. Solution blending, melt mixing, and electrophoretic deposition are also used to incorporate graphene into the polymer matrix.[7]
- Direct Digital Manufacturing (DDM) is one novel process for creating GNP-reinforced aluminium matrix composites that is both unique and efficient. DDM uses considerable plastic strain and frictional and deformation methods to generate heat. This synergistic impact promotes dynamic recovery and recrystallisation, uniformly dispersing Graphene Nanoplatelets (GNPs) and forming ultra-fine microstructures. The technology reduces processing time and improves microstructural manipulation. DDM works in many metal matrix composites, demonstrating its versatility and potential. Despite the favourable results of DDM on other metal matrix composites, GNP-reinforced aluminium matrix composite investigations are expected. Direct Digital Manufacturing (DDM) study on the effects of processing factors on these composites' microstructure and mechanical properties must be included. Although specialised studies have explored the mechanical properties of composites, there needs to be more studies on improving strength-ductility, which is critical in real-world applications. This research is relevant to the study's aims. Direct Digital Manufacturing (DDM) of aluminium matrix composites containing Graphene Nanoplatelets (GNP) may solve GNP dispersion and interfacial bonding issues. This work addresses literature gaps and analyses processing parameters to improve composite strength-ductility efficiency and mechanical performance.[8]
- Hot extrusion is the primary method for compacting graphene nanosheets and aluminium particles into a billet. Hot rolling then improves the composites' microstructure and mechanical properties. Extrusion-MPHR hybrid deformation improves graphene nanoplatelet dispersion and interfacial bonding, enhancing mechanical properties. GNS content, extrusion parameters, and hot rolling circumstances have been studied in composites' microstructure and mechanical properties. Interfacial reaction products, such as Al_4C_3, at the interface between aluminium and graphene nanosheets and their impact on the composite material, have also been studied. However, hybrid deformation's unique effect on graphene nanosheet dispersion and interface bonding must be better understood. Graphene nanoplatelets aluminium composites are progressing, although certain areas need additional research and development. First, hybrid deformation's effects on composite grain boundary network distribution and interfacial structure should be studied more. To optimise composites' mechanical properties, these changes must be understood. Despite GNS/Al composite strengthening studies, load transfer strengthening efficiency and interaction with the interfacial structure must be thoroughly evaluated. Interfacial transition zones might increase load transmission during hybrid deformation. A quantitative appraisal needs to be improved.[9]
- A prevalent technique is mechanical stir casting, which entails mixing multi-walled carbon nanotubes and Mg (wettability agent) with molten A356 alloy and solidifying. Wu, Chang, Gurkan, and Cebeci utilised the Taguchi method, a robust experimental design, to optimise composite development parameters. They discovered that the quantity of multi-walled carbon nanotubes, magnesium, and duration of mechanical agitation significantly affected the composite's mechanical properties. The role of mechanical agitation in dispersing multi-walled carbon nanotubes within the matrix has been extensively investigated. Wang et al. and Alhawari et al. discovered that

mechanical agitation enhanced the homogenous distribution of reinforcement materials within an aluminium matrix. In addition, Mg is frequently used as a wettability agent to improve the hydration and interfacial bonding between multi-walled carbon nanotubes and the aluminium matrix. Bakr et al. reported that adding 0.75 % Mg to the liquid enhanced its wettability. Although significant progress has been made in fabricating and characterising multi-walled carbon nanotubes -A356 composites, certain limitations persist. Determining multi-walled carbon nanotubes and Mg content within the matrix continues to be complicated. Moreover, although several studies have investigated the effects of multi-walled carbon nanotube content, mechanical agitation, and Mg on mechanical properties, a comprehensive optimisation strategy is still required to achieve an optimal combination of these parameters.[10]

- The distinctive qualities of graphene, such as its two-dimensional flaky structure and substantial surface area, have been highlighted. These qualities make graphene an appealing reinforcing material for aluminium matrices. Graphene reinforcement particles are distributed uniformly despite some investigations reporting grain boundary aggregation at more significant graphene weight percentages. The composites were successfully constructed using hot extrusion and microwave processing processes, which allowed them to satisfy the requirements for structural usage in the super lightweight external fuel tank. This study's specific objectives are to examine the process by which graphene adheres to the aluminium matrix and to assess the impact of various graphene weight percentages on the microstructure and mechanical characteristics of the composite.[2]
- Many authors have focused on developing corrosion-resistant coatings for aluminium alloys. Polymer electrolyte oxide (PEO) coatings have gained popularity because of their hardness, thickness, and corrosion resistance. Graphene nanomaterials in coatings have been widely studied for corrosion protection. Graphene's electron-rich structure and colossal surface area make it a promising corrosion inhibitor for metal substrates. Plasma electrolytic oxidation (PEO) coatings have been tested for corrosion resistance utilising graphene. Electrochemical impedance spectroscopy (EIS) and potentiodynamic polarisation curve measurements are routinely used to assess coating corrosion behaviour. The scanning Kelvin probe (SKP) has also been used to compare the Volta potential of coated and uncoated materials, providing microelectrochemical insights into corrosion. Graphene-incorporated PEO coatings' corrosion resistance has been studied. The study has several undiscovered regions. First, no literature compares graphene concentrations and their effects on PEO coating corrosion resistance. Graphene's processes for improving PEO coatings' corrosion resistance still need clarification. Scalability and industrial viability must also be investigated.[11]
- The authors have applied FSAM to aluminium-lithium alloys, specifically 2060 Al-Li, the third-generation alloy. FSAM, a solid-state additive manufacturing method, avoids melt-based AM difficulties. The authors used laser-assisted powder bed fusion (L-PBF) to build Al-14Li alloy blocks with fissures and inclusions. They used wire arc additive manufacturing (WAAM) to deposit AA2050 Al-Li alloy with microstructural variations. They examined the laser melting dimension (LMD) of 2A97 Al-Li alloy and found non-uniform microstructures and poor mechanical characteristics. FSAM can produce structurally efficient magnesium alloy components and 7N01-T4 Al alloy with finer and more uniform microstructures and moderately enhanced automatic features. Traditional melt-based AM techniques generally have coarse microstructures and internal flaws due to the melting-solidification cycle. FSAM avoids metallurgical defects during melting and solidification in solid-state additive manufacturing. Compact and fine FSAM granules improve mechanical characteristics. FSAM also causes dynamic recrystallisation during intense plastic deformation and heat input, producing fine equiaxed granules between 2 and 5 m in the nugget zone.[12]

- However, despite these advancements, several voids in the existing literature must be addressed. First, more research should be conducted on the combined influence of copper, alumina, and graphene on the properties of aluminium composites. Although individual studies have examined the effects of these components, a comprehensive comprehension of their synergistic interactions still needs to be improved. Fixing this gap is essential for optimising aluminium composites that use multiple reinforcements. More research needs to be conducted on the effects of secondary processes, specifically hot rolling, on the microstructure and properties of aluminium composites. Much research has concentrated solely on the powder metallurgy technique, ignoring the potential improvements that can be attained through subsequent processing stages. It is essential to investigate the effects of hot rolling as a secondary procedure to optimise the properties of aluminium composites and reveal the mechanisms underlying the improvements.[13]
- While individual reinforcements have been exhaustively examined, research on hybrid composites that combine multiple mounts is limited. Sometimes, the optimal combination of reinforcement particles and their respective volume fractions for attaining the most significant wear performance is not well-defined. Wear behaviour under varied loads and sliding conditions: The wear behaviour of Al-Si composites under varying loads and sliding velocities requires additional research. Inadequate study of wear mechanisms: It is essential to identify the factors contributing to wear resistance and degradation by thoroughly investigating wear mechanisms in various composites.[14]
- Most synthesis methods use dangerous substances or excessive energy, harming the environment. Assessing and managing these impacts is essential for using graphene-based devices. Industrial graphene production is challenging. Scalable, cost-effective technologies like FJH need optimisation and validation to satisfy commercial expectations. Refuse materials for graphene production are untested. Research should find suitable carbonaceous sources and evaluate their environmental impact.[15]
- Carbon nanotube yarns have demonstrated repeatable, stable resistance behaviour and low density, making them appropriate for real-time monitoring of composite deformation and fracture propagation. Moreover, incorporating carbon nanotube fibres into an epoxy matrix preserves their flexibility, preventing permanent fractures even after substantial deformations. Authors have also investigated multi-objective optimisation to determine the optimal graphene nanoplatelet distribution pattern and material profile for attaining desirable structural performance goals. CNT-steel composites have demonstrated potential for applications in high-pressure and high-temperature environments requiring anticorrosive and mechanically robust materials. In addition, the improvement of CNT web performance for mode I interlaminar fracture toughness has been identified as a potential area for future research, which may involve amino-functionalization. The use of carbon nanotubes in cementitious composites has the potential to overcome the functional limitations of conventional conductive additives; however, additional research is necessary to assure durability and stability. In addition to experimental characterisation, numerical analysis has been used to examine fracture behaviour, fissure initiation and propagation, and microstructural damage in CNT and graphene composites.[16]
- Nanocomposites reinforced with CNTs and graphene have been studied for their mechanical properties and fracture response. Authors have used different polymer matrices to examine many carbon nanotubes (CNT), graphene production, and nanocomposite synthesis methods. Tensile strength, Young's modulus, and fracture toughness have been studied using experimental and computational methods. Authors have studied how carbon nanotube (CNT) and graphene concentration, dispersion, and alignment affect nanocomposites' mechanical characteristics. Since the matrix-CNT-graphene interfacial bonding determines mechanical properties, considerable study has focused on it. Examining nanocomposites' fracture behaviour has included CNT defects, inclusions, and agglomeration. They have used numerical modelling methods to predict nanocomposites' mechanical properties and fracture tendencies. FEA, MD, and micromechanics

models are used. Tensile testing, fracture toughness, and interlaminar fracture tests have supported computational results.[16]

- Aluminium-graphene nanoplatelet (GNP) composites have been manufactured using numerous methods. Powder metallurgy and hot extrusion evenly distribute graphene nanoplatelets (GNPs) in the aluminium matrix. Spark plasma sintering, hot accumulative roll bonding, and hot rolling have been researched for making these composites. Composites' mechanical and thermal properties have been studied using various processing methods. The series, parallel, Maxwell, Son-Frey, and Russell models have been used to estimate thermal conductivity in these composites. These models assess composites' effective thermal conductivity by considering volume percentage, shape, matrix and reinforcing thermal conductivities. Experimental studies on aluminium composites' mechanical and thermal properties, incorporating graphene nanoplatelets (GNPs), have neglected finite element modelling of heat conductivity. There are few limited element analysis studies predicting these composites' thermal properties. Given the research gap, finite element analysis may be able to accurately estimate the thermal conductivity of aluminium composites, including distributed graphene nanoplatelets (Harichandran et al., 2022).[17]
- Stir casting is popular because it evenly distributes reinforcements and bonds the matrix and particles. Stir casting has better reinforcement distribution than other methods, improving mechanical characteristics. Researchers altered weight percentages to determine how SiC and B4C affect aluminium composite characteristics. Studies show a trade-off between mechanical parts and ductility as the B4C level enhances hardness and tensile strength but decreases elongation %.[18]
- Based on a literature analysis, graphene nanoplatelets (GNPs) can improve mechanical characteristics in aluminium matrix composites. Correct GNP dispersion during mechanical alloying can improve mechanical behaviour together with sintering optimisation. Composites with extended milling periods and higher GNP concentrations should be more complex. The research also optimises processing settings, investigates graphene shapes, and creates composites for real-world applications to fill gaps in the literature.[19]
- Extensive research has demonstrated the potential of GNFs as reinforcing agents in various materials; the investigation of GNFs as supporting agents in metals or aluminium alloys, especially aluminium alloys, still needs to be completed.[20]
- The synthesis method and reinforcement material substantially affect Al nanocomposite reinforcing mechanisms and mechanical properties. For Al_2O_3 and Al-GNP nanocomposites, particle size is a crucial factor in determining their strength and durability. In addition, impurities and the bonding quality between the matrix and reinforcement may play a significant role in the nanocomposite's overall strength.[21]

2.2 FEA on Composite Plate

- Numerous ANSYS studies have examined rectangular plate buckling analysis. Hassan and Kurgan evaluated shell and solid plate models to measure buckling prediction accuracy. They stressed the importance of lattice density and found that shell models, notably Shell281, are more realistic for thinner plates. Solid models of solid-shell components, such as Solsh190, were recommended for bigger vessels because they match 3D elasticity theory answers.[22]
- Authors have employed various modelling strategies and numerical tools for delamination buckling analysis. The delamination behaviour is simulated using a two-sublimate model in Ansys with eight-node composite shell elements. The two sub-laminates are coupled, and the delaminated region's nodes are left uncoupled. This method provides a practical technique for modelling delaminated composite panels and demonstrates excellent agreement with theoretical predictions and prior research. Despite significant advancements in delamination buckling analysis, certain voids remain. A significant omission is the consideration of eccentricity in loading, particularly for thin panels with close-to-surface delamination. The study in Section 5.2 highlights the significance

of this factor and demonstrates that eccentricity substantially affects the distribution of buckling load and strain energy release rate. In addition, while previous research has focused on narrow near-surface delamination, mid-plane delamination has received less attention. This investigation compares the buckling behaviour in both situations.[23]

2.3 FEA on External Fuel Tank of Launch Vehicle

- Authors have tried many methods to integrate LH2 fuel tanks. Petroleum container stress distribution and deformation under different loading circumstances have been assessed using FEA. Stress intensities and structural integrity have been examined for flat, concave, and convex-concave catwalk geometries. Thermal analysis has also been crucial to study, focusing on heat transport inside fuel tanks during flight to keep LH2 in its liquid/gas phase and prevent excessive boil-off. Studies have used advanced thermal insulation and ventilation systems to maintain vessel structural integrity under fluctuating pressure and temperature. Studies have found that scaffold configurations with compressive loads may be unstable. Understanding the collapse behaviours and strengthening the catwalk require more research. Access holes might spill petrol in deformed areas.[24]
- Space launch vehicle container structural analysis and design have been thoroughly researched to assure prelaunch safety and reliability. The buckling and nonlinear behaviour of thin-walled structures, especially under mechanical and thermal pressures, have been essential areas of study. The Space Shuttle Standard-Weight Tank (SWT) and Superlight Weight Tank (SLT) have been examined for structural response. Launch vehicle containers are simulated using finite-element analysis (FEA). FEA can accurately anticipate buckling modes and nonlinear reactions by representing complicated geometries, loading circumstances, and material characteristics. Limit-point and bifurcation buckling studies have also been employed to capture the containers' critical behaviour under various loading situations.[25]
- The aerospace industry uses analytical and empirical data-based conceptual design methodologies. These approaches suit initial design assessments but may not capture complicated subsystem relationships. Instead, Chiesa et al.'s integrated technique considers structural and aerodynamic considerations early in the design process. Finite element analysis improves vehicle performance under diverse loading circumstances, improving take-off mass predictions and design precision. Reusable space rockets require extensive structural analysis despite conceptual design advances. Many studies need to pay more attention to the complex interdependencies between subsystems, resulting in erroneous mass estimations and design inefficiencies. Chiesa et al.'s integrated technique addresses this by using structural analysis early in conceptual design. Their approach focuses on a class of launch vehicles like Venture Star, which might be applied to various configurations and mission parameters.[26]
- Vacuum-jacketed plans with aluminium tanks give better thermal insulation and structural strength. Sandwiched structures using aerogel insulation take use of aerogels' low heat conductivity. Despite their low thermal conductivity, studies show that aerogels are too weak to store cryogenic propellant. Finite element analysis has examined cryogenic vessels' structural behaviour. Using MATLAB and Abacus, researchers have learned about insulation systems and tank designs thermal performance. Research gaps still need to be addressed despite cryogenic tank design breakthroughs. Insulation with low thermal conductivity and high mechanical strength is lacking. Structural integrity and thermal efficiency are still issues. Cryogenic propellant storage heat transfer optimisation is another need. Prolonged flights require avoiding propellant boil-off, although liquid cryogenics are small.[27]

IV. METHODOLOGY

4.1 Process Flowchart

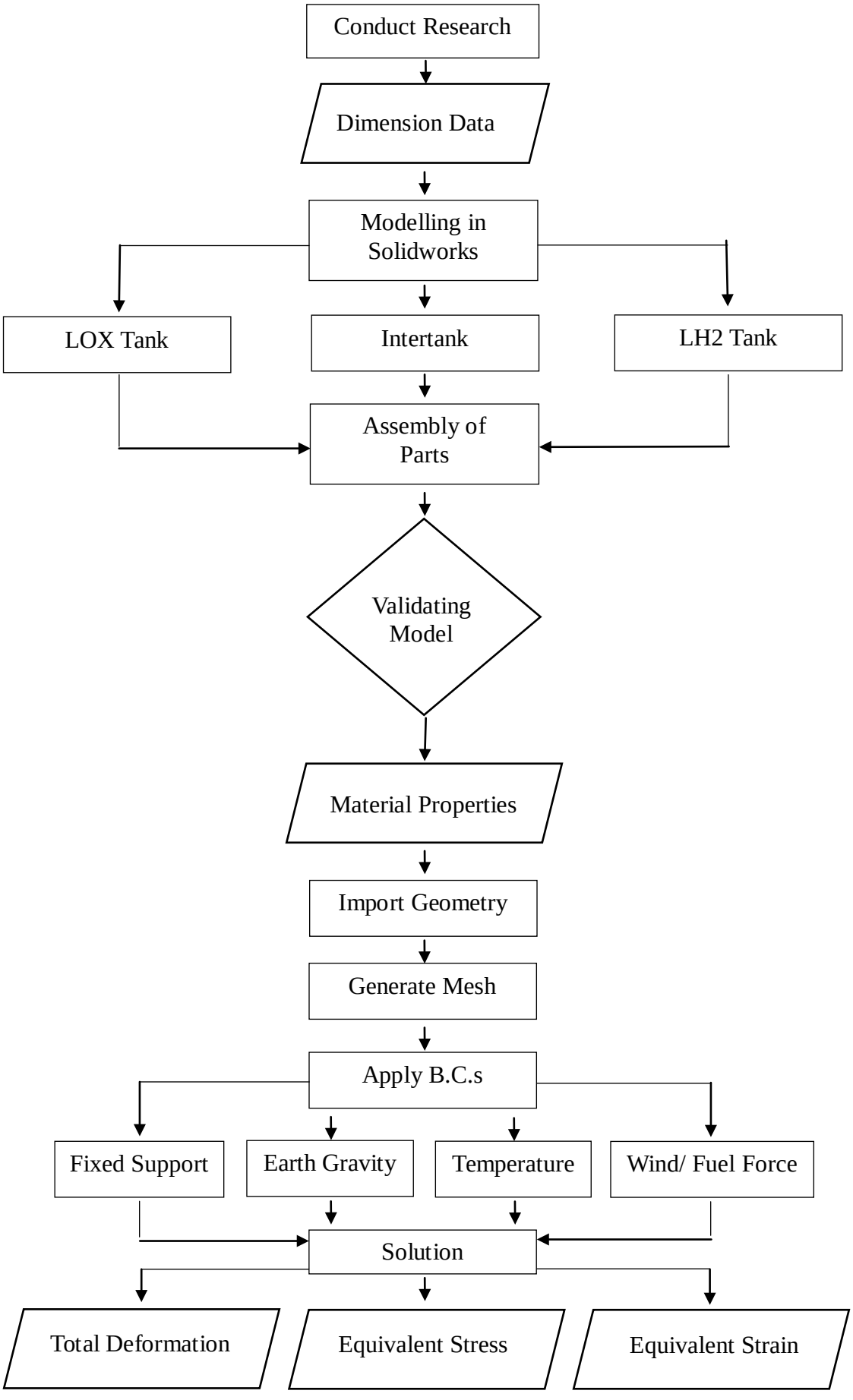

The flowchart above illustrates the procedural steps undertaken to obtain a solution. Gaining an understanding of the sequential progression of the process would be beneficial. The initial step is researching the external fuel tank of the launch vehicle. The dimensional data will be inputted throughout the modelling of the external fuel tank. The subsequent step involves modelling three components: the LOX tank, Intertank, and LH2 tank. The method of assembling all parts occurs next to the design phase. The model that has been constructed is subjected to a validation process to ascertain the level of perfection in its design. The subsequent procedure is conducted via Ansys software. The input of the material characteristics will be shown. The next step entails the importation of geometric data. Subsequently, the mesh will be generated. The next step involves the application of boundary conditions, including fixed support, the influence of earth gravity (weight), wind/fuel force, and air temperature/fuel temperature. The answer will be expressed in terms of total deformation, equivalent stress, and equivalent elastic strain. The above diagram illustrates the fundamental sequence of steps in the procedure. The prescribed flowchart conducts the analysis.

4.2 Model Development

4.2.1 External Fuel Tank of Launch Vehicle

Launching the space shuttle into orbit necessitates a substantial quantity of fuel, exceeding 2 million litres, consumed during each launch. Additionally, a pretty voluminous tank is required to contain this fuel. The most significant and massive component of a fully fueled space shuttle is the externally mounted fuel tank, commonly referred to as an ET by the National Aeronautics and Space Administration. This tank has a rust-coloured appearance and possesses a bullet-like form.

The external tank, with dimensions of 46.9 metres in length and 8.4 metres in diameter, serves as the primary support structure for the shuttle during its launch phase. It is crucial in absorbing the substantial thrust of around 2.7 million kilograms created during the blast-off process. The primary function of the external tank, however, is to supply pressurised fuel to the three hydrogen-burning main engines of the shuttle during the eight-and-a-half-minute journey into space. The engines have a propellant consumption rate of 242,000 litres per minute.

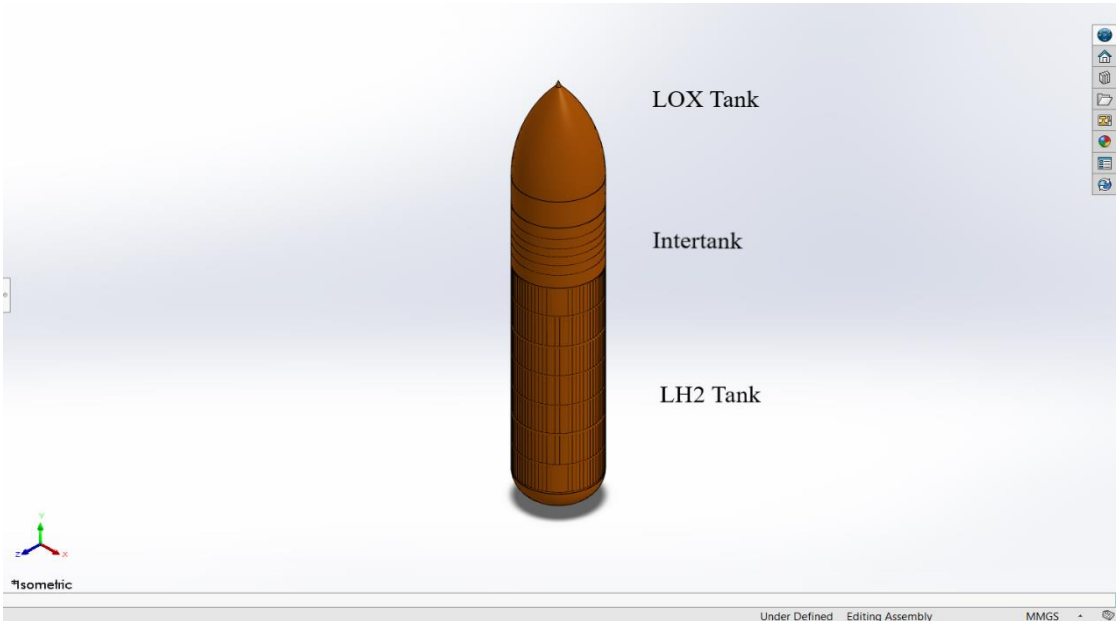

Figure 2: Model of External Fuel Tank of Launch Vehicle

Transporting such a substantial amount of fuel into outer space presents considerable challenges. Specifically, almost one-quarter of the total launch weight of the shuttle, which amounts to 2 million

kilograms (or 4.4 million pounds), is solely attributed to the importance of the fuel. However, contributing to the intricacy is the atypical composition of the power, which has only a distant resemblance to the petrochemicals commonly employed in the majority of motor vehicles.

The exterior tank is comprised of liquid hydrogen and liquid oxygen, which are extremely cold liquids that must be maintained at temperatures much below freezing, even in the typically warm climate prevalent in the Florida launch location of the shuttle. The external tank has many layers of specialised foam insulation to prevent ice formation on its outside surface in the hours before the launch. During the launch, ice present on the shuttle can detach and potentially cause harm to the spacecraft.[28]

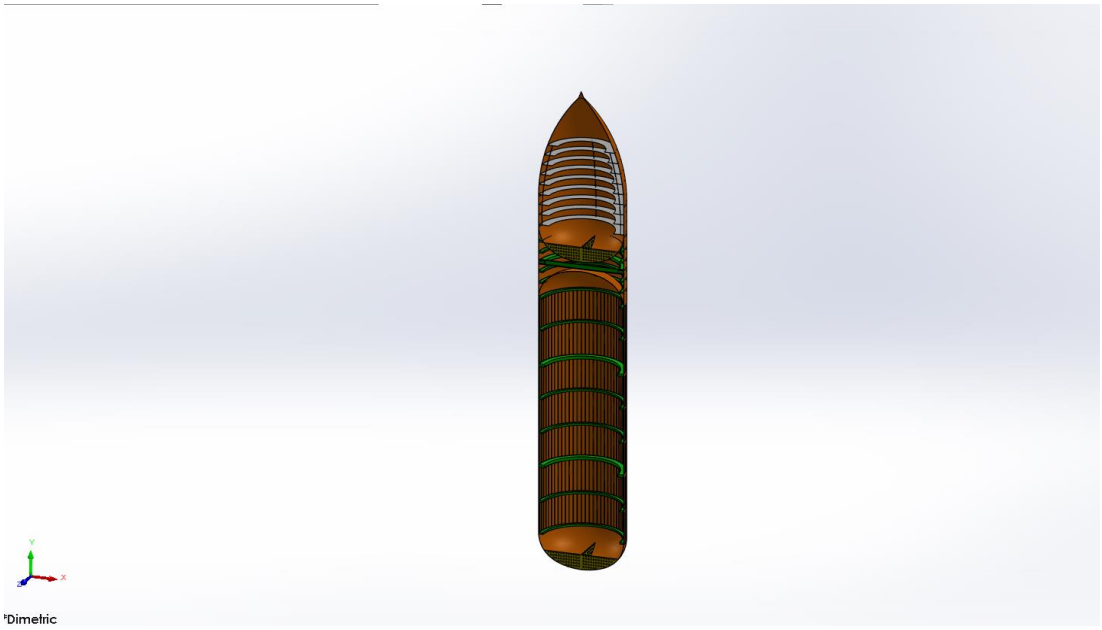

Figure 3: Sectional Diagram of External Fuel Tank of Launch Vehicle

There are three main parts of the external fuel tank of the launch vehicle:

4.2.1.1 Liquid Oxygen Tank (LOX Tank)

Technical Specifications: [29]

- Length = 16.6 m (16,600 mm)
- Diameter = 8.4 m (8,400 mm)
- Operation pressure: 34.7–36.7 psi (239–253 kPa) (absolute)
- Thickness = 25 mm

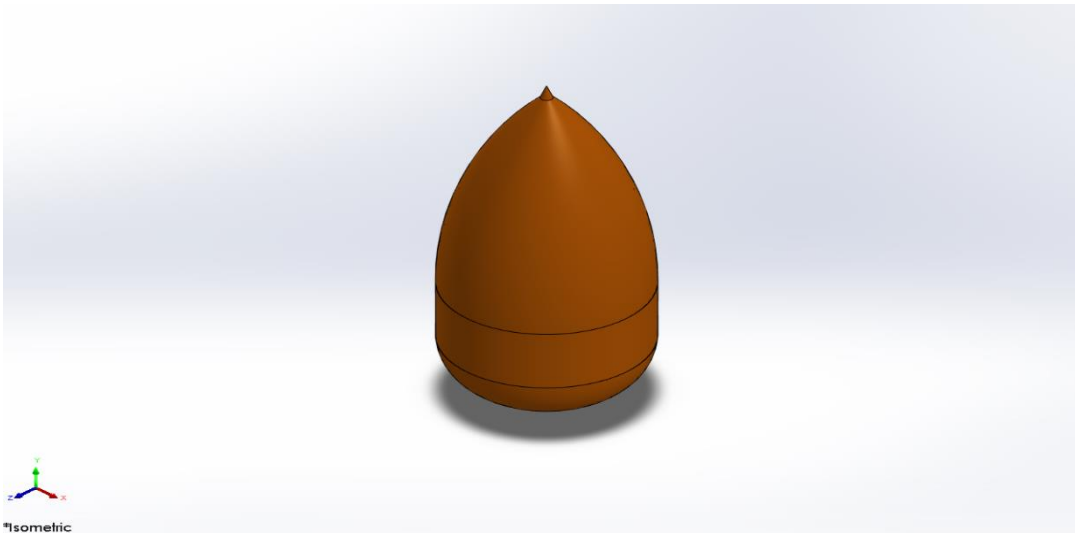

Figure 4: Liquid Oxygen Tank

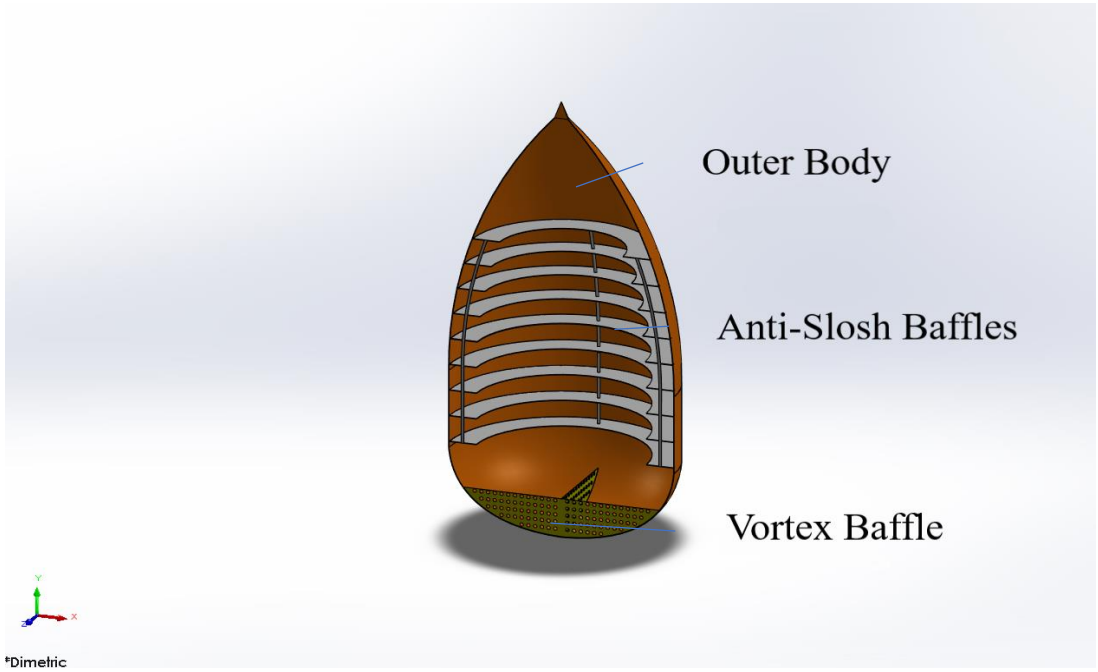

Figure 5: Sectional Diagram of Liquid Oxygen Tank

4.2.1.2 Intertank

Technical Specifications:[29]

- Length: 22.6 ft (6,900 mm)
- Diameter: 27.6 ft (8,400 mm)
- Thickness: 25 mm

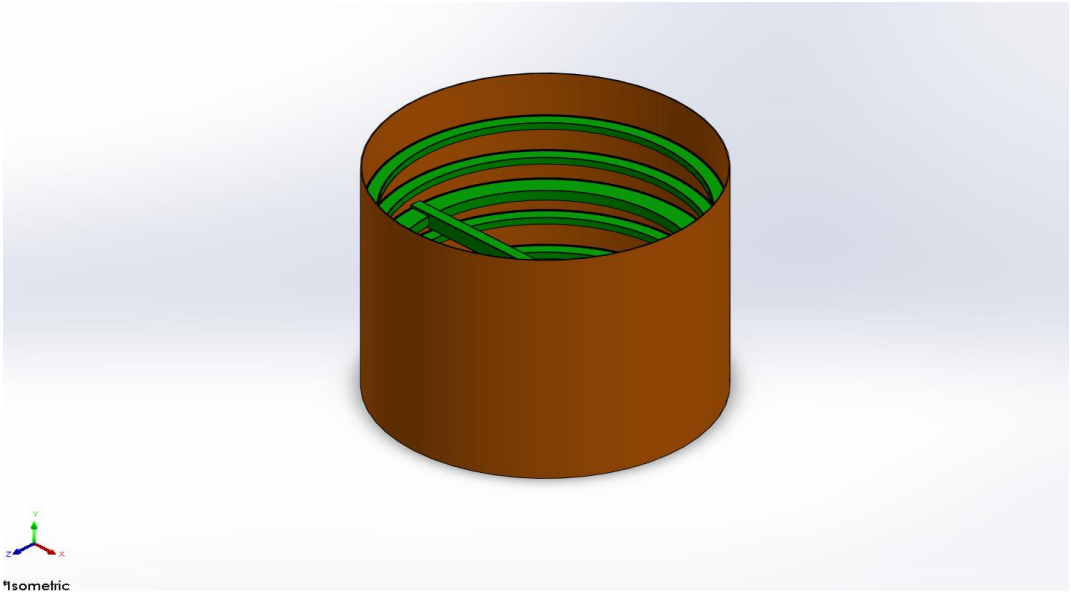

Figure 6: Intertank

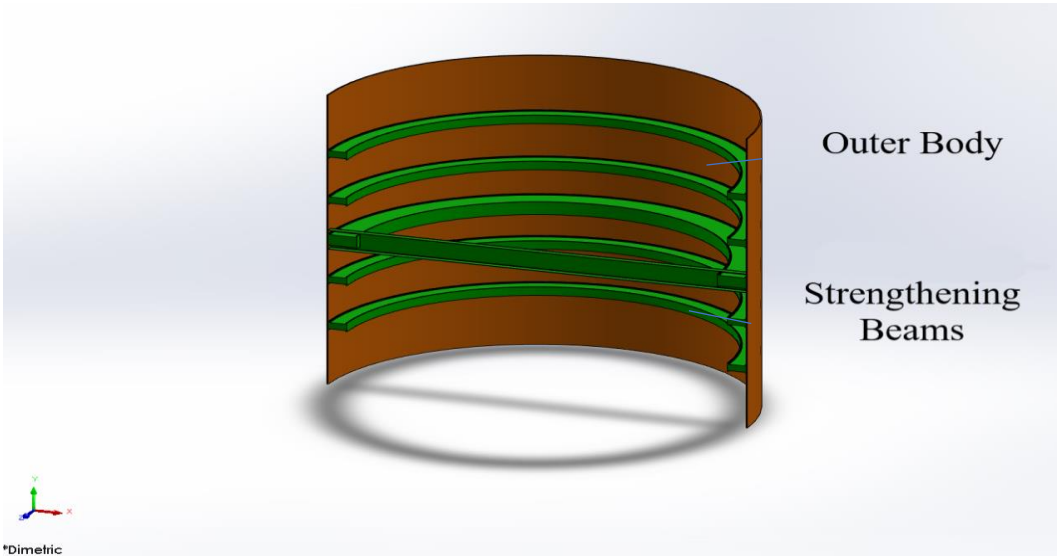

Figure 7: Sectional Diagram of Intertank

4.2.1.3 Liquid Hydrogen Tank (LH2 Tank)

Technical Specifications:[29]

- Length: 97.0 ft (29,600 mm)
- Diameter: 27.6 ft (8,400 mm)
- Operation pressure: 32–34 psi (220–230 kPa) (absolute)
- Operation temperature: −423 °F (−253 °C)
- Thickness: 25 mm

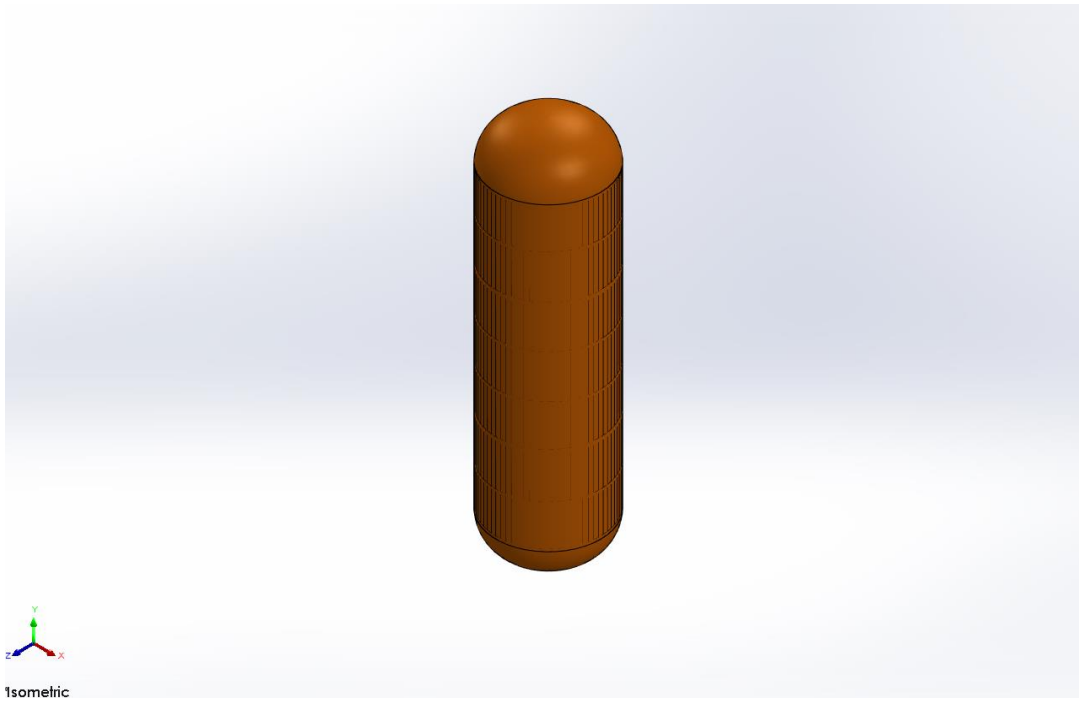

Figure 8: Liquid Hydrogen Tank

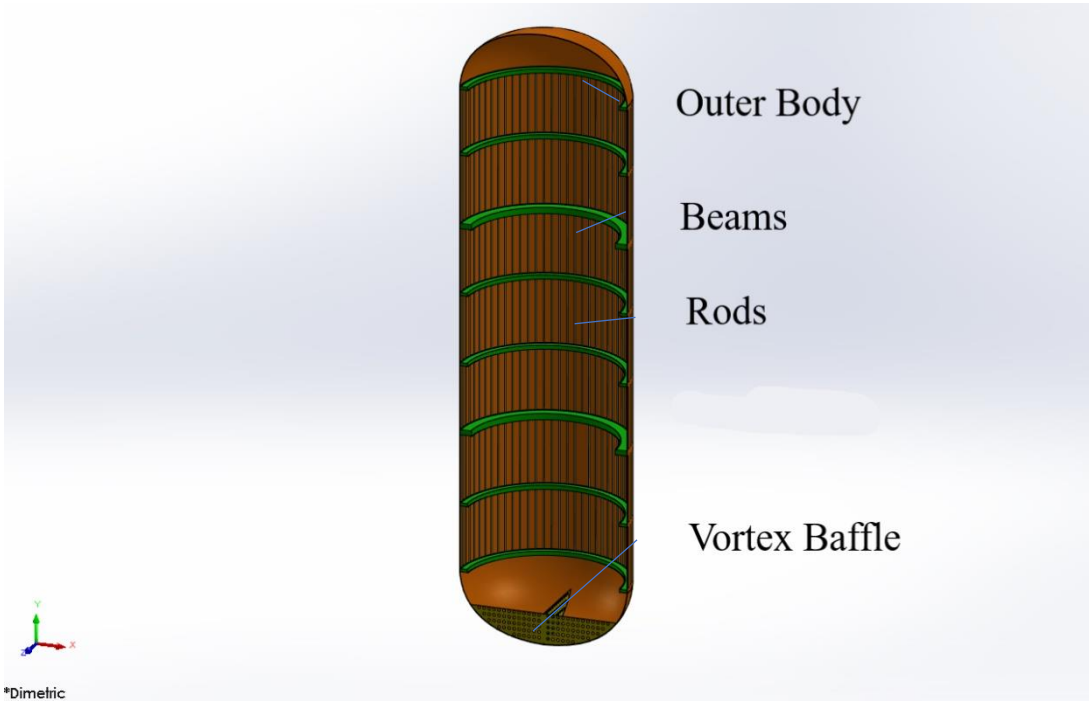

Figure 9: Sectional Diagram of Liquid Hydrogen Tank

4.3 Material Properties

Material – 2195 Aluminium alloy with 0.5% wt. Graphene

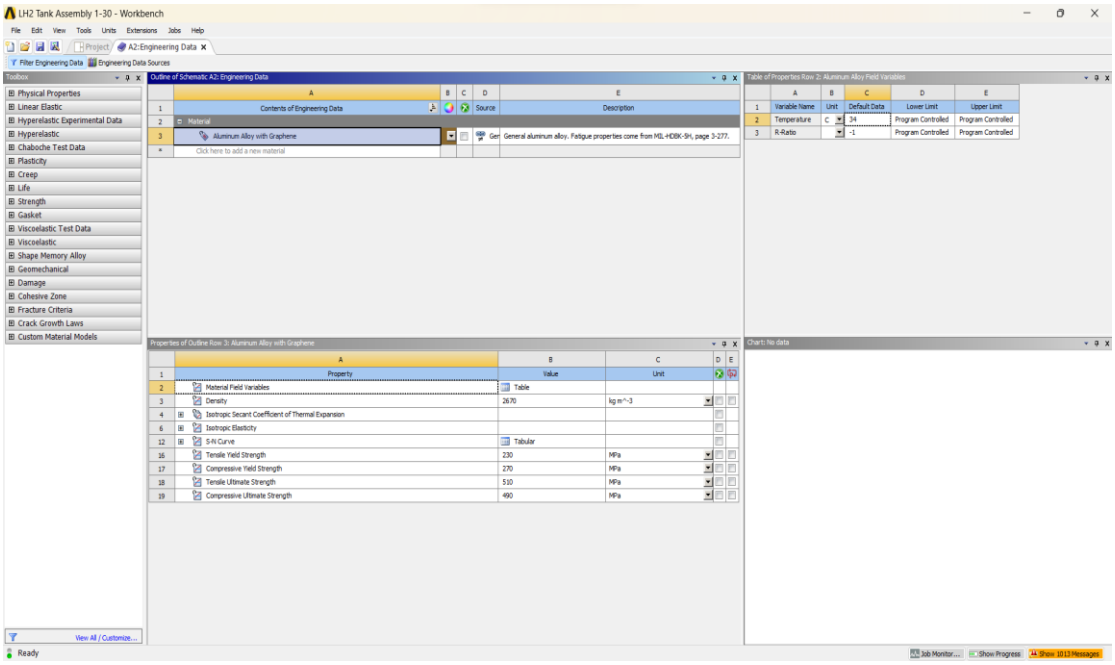

Figure 10: Material Properties

The composition of aluminium alloy 2195 consists of 4.2% copper (Cu), 1.1% lithium (Li), 0.35% magnesium (Mg), 0.35% silver (Ag), 0.15% zirconium (Zr), 0.15% iron (Fe), and 0.10% silicon (Si), with the rest portion being comprised of aluminium. This constitutes the majority of the alloy. The aerospace industry employs this material extensively, such as propellant tanks, gores sheets, forgings, maintenance hole covers, and feed line extrusions. The microstructure of alloy 2195 exhibits grains that possess an elongated morphology oriented orthogonally to the forging direction. The identification of aluminium-lithium alloys may be accomplished by observing the presence of very long grains oriented in the rolling direction. This characteristic is a distinctive attribute of the alloy.[30]The influence of the crystallographic microstructure of alloy 2195 on its formability is evident. A significant Bs 101h121i element may lead to diminished formability, as shown by previous research—the occurrence of planar slip results in the deformation of the component. Conversely, a thermomechanical processing condition that yields a grain size characterised by greater equitability and fineness and a much weaker Bs texture can enhance formability.[31]The microstructural evolution of alloy 2195 under substantial strain deformation was investigated by researchers using a hot isothermal plane strain compression (PSC) testing method, which included a single shot. The flow curves recorded during PSC exhibited a moderate decrease in stiffness at elevated temperatures, along with a downward deviation of the flow curve at a strain rate of $1s^{-1}$. A study on optical microstructures revealed that specimens subjected to deformation at lower temperatures (300 °C and 350 °C) exhibited compressed grains. In contrast, samples deformed at higher temperatures (400 °C and 450 °C) displayed stress-free grains characterised by wavy grain borders. The use of electron backscattered diffraction in the analysis revealed the occurrence of dynamic recrystallisation in samples that underwent deformation at elevated temperatures and reduced strain rates. In a broader context, manipulating temperature and strain rate during thermo-mechanical processing offers the potential to modify the properties of aluminium alloy 2195, explicitly allowing for grain size regulation.[32]

4.4 FEA on Composite Plate

The static analysis is done on the 500x500x25 mm composite plate. There are several reasons to analyse composite plates.

- Finite Element Analysis (FEA) is a computational method that enables the prediction of the structural response of a composite plate subjected to various loading circumstances, including mechanical loads, temperature variations, and external forces. Making accurate predictions is crucial in developing and optimising structures to ensure they perform their intended tasks effectively.
- Conducting physical experiments on composite materials may be both time-consuming and costly. Finite Element Analysis (FEA) enables engineers to visually model various situations, saving time and cost by eliminating the need for repeated design iterations.
- Finite Element Analysis (FEA) allows for optimising composite plate designs by examining different materials, geometries, and configuration combinations. This process determines the efficient and effective method of meeting the specified performance objectives.

Von Mises Stress:

The von Mises stress is a metric used to quantify the magnitude of the equivalent stress experienced by a material during plastic deformation. The significance of this phenomenon is in its ability to provide criteria for accurately anticipating the beginning of yielding or failure in materials that exhibit ductility. The von Mises stress is a measure considering the combined influence of everyday and shear stresses. It is often used in engineering contexts to evaluate various components' structural soundness and safety. The von Mises stress is very advantageous in scenarios characterised by the isotropic yield behaviour of a material, whereby the material's response to stress is consistent regardless of the particular orientation of the applied pressure. In plasticity theory and finite element analysis, it is customary to use a method to ascertain the critical stress thresholds at which plastic deformation occurs.[33]

Von Mises Strain:

The Von Mises strain is a metric that quantifies a material's deformation or strain when subjected to external stress. The principle used is the von Mises yield criteria, which posits that a substance will undergo plastic deformation or yield whenever the von Mises stress is above a certain threshold. The von Mises strain is determined by evaluating the significant pressures, representing the highest and lowest strains encountered by the material along distinct orientations.

The von Mises strain is a scalar quantity that denotes the magnitude of pressure experienced by a material, considering the combined effect of many strain components. The measurement considers the cumulative impact of standard and shear stresses, assessing the material's total deformation. Structural analysis shows that this phenomenon proves advantageous when the material is exposed to intricate stress conditions.

It is used to evaluate the propensity for plastic deformation and failure of a material by using the von Mises strain calculation. The assessment aids in the determination of the structural integrity and dependability of construction when subjected to various loading scenarios.

Mesh:

The mesh generation process has significant importance in finite element analysis (FEA) since it involves the division of the study continuum into discrete pieces or finite elements. The mesh functions as a discretised portrayal of the geometry, enabling the computation of approximate solutions to the governing equations. The mesh may be produced either manually or automatically. In manual meshing, the analyst generates the mesh by explicitly specifying the elements and nodes, considering the geometric characteristics and the desired degree of refinement. This methodology provides enhanced manipulation of the mesh quality and may be especially advantageous in accurately representing stress

patterns at points of geometric discontinuity. In contrast, automated meshing entails using software tools to produce the mesh, using predetermined criteria such as element size, element type, and mesh density. This methodology exhibits enhanced speed and efficiency, mainly when dealing with intricate geometrical structures. Nevertheless, human meshing offers a higher degree of control compared to automated methods. The selection of mesh density or element size is paramount due to its impact on the analysis's precision and computing efficiency. Using a finer mesh in computer simulations yields more precise outcomes but costs more processing resources and time. Hence, it is common to strike a balance between precision and efficiency. In essence, mesh creation involves partitioning the analysis domain into discrete finite elements. The process may be executed manually or automatically, and the selection of mesh density plays a crucial role in attaining precise and effective outcomes in finite element analysis.[34]

Applying loads and solution phase:

Applying Loads: Loads are essential in finite element analysis (FEA). It involves defining the external forces, pressures, displacements, or constraints that act on the model. These loads represent the real-world conditions the structure or component will experience during operation. The loads can be applied in various forms, such as point, distribution, pressure, thermal, or displacement constraints. The choice of load type depends on the specific analysis requirements and the behaviour of the structure under consideration. For example, point loads can represent concentrated forces or moments applied at particular locations in structural analysis. In contrast, distributed loads can represent uniform or varying loads applied over an area or along a line. Pressure loads can mean fluid or gas pressures acting on the surface of a structure, and thermal loads can represent temperature gradients or heat transfer effects. The loads should be applied in the same units as the specified model geometry and material properties. It is essential to accurately define the magnitude, direction, and location of the loads to obtain meaningful results from the analysis.

The solution phase in finite element analysis involves solving equations representing the model's behaviour under the applied loads. This is typically done using numerical methods and iterative algorithms. The solver takes the input from the pre-processor, including the mesh, material properties, and applied loads, and calculates the unknowns of the problem, such as displacements, stresses, strains, temperatures, or any other desired output. The solver uses the finite element method (FEM) to discretise the model into more minor elements and then assembles the element equations into a global system. These equations are then solved to obtain the solution for the unknowns. The solution process involves iterating through the equations until convergence is achieved, ensuring that the calculated values satisfy the equilibrium and compatibility conditions of the model. The convergence criteria are typically based on the desired accuracy and the convergence behaviour of the solution. Once the key is obtained, post-processing techniques are used to analyse and interpret the results. This may involve generating contour plots, deformed shapes, stress distributions, or other relevant visualisations to understand the model's behaviour under the applied loads.

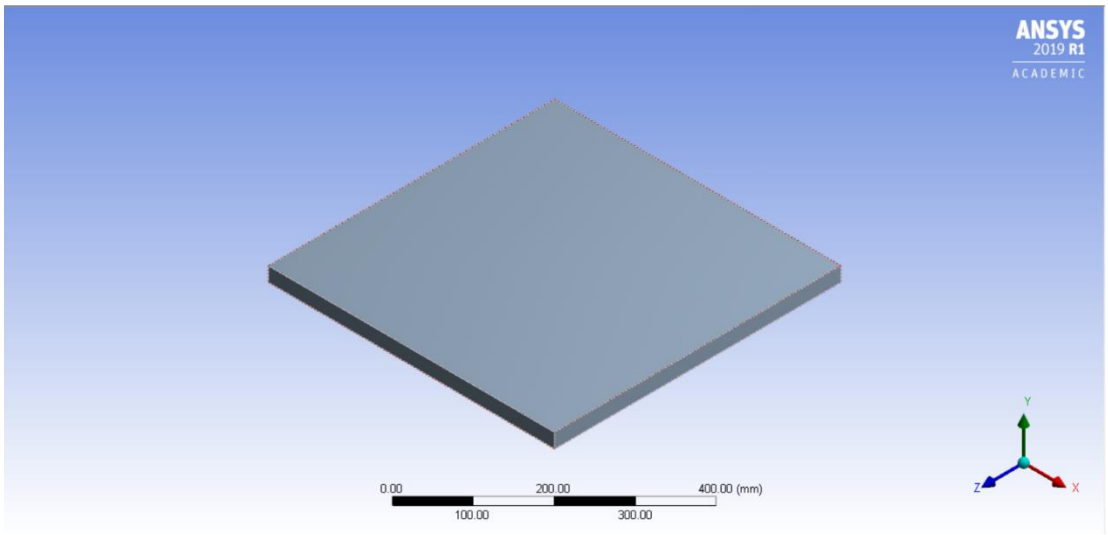

Figure 11: 500x500x25 mm Plate

In order to obtain the most precise results, it is essential to maintain exact mesh settings. Mesh size is kept at 5 mm.

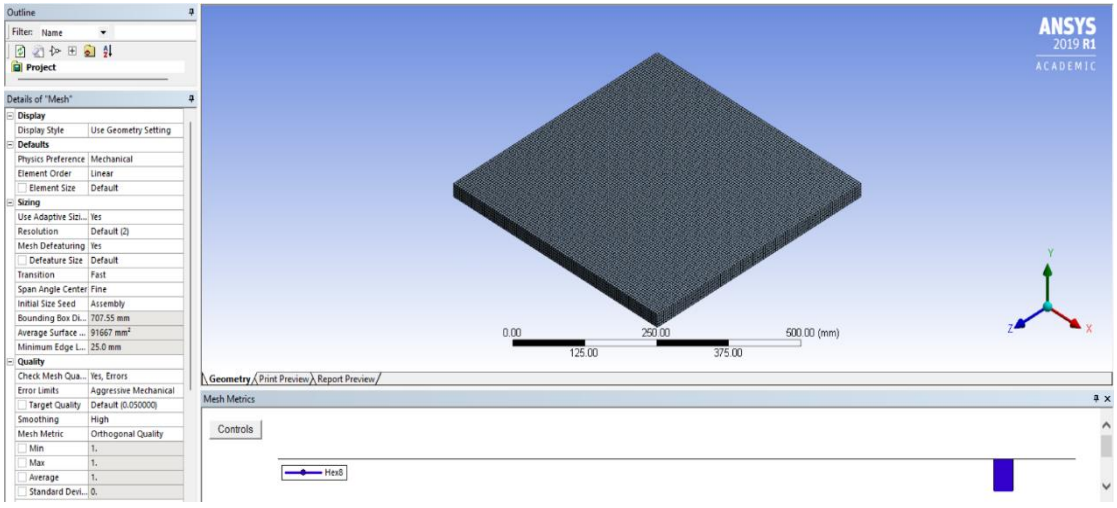

Figure 12: 500x500x25 mm Plate Mesh Settings

- Boundary Conditions for FEA Analysis

Wind Force Calculation

The launch can be considerably impacted by wind. The prevailing wind conditions on that particular day may influence the rocket's trajectory. Powerful gusts of wind can alter the missile'. The movement of wind exhibits variability in direction. However, in the launch context, it is advisable to conceptualise the wind as a horizontal vector perpendicular to the aircraft's vertical trajectory. In light of this circumstance, engaging in calculations and implementing model modifications is imperative to accommodate the disturbance.[35]

For all the analysis, it is assumed that the launch will happen in Cornwall City, and wind will flow in the -Z Direction as the geometry is symmetric.

Wind Force Calculation[36]

Highest Temperature in Cornwall = 34°C
Wind Speed in Cornwall = 22 MPH = 9.835 m/s

Density of air at sea level = 1.229 kg/m^3
Area of the plate hitting by air = Width x Thickness = 0.5 x 0.025 = 0.0125 m^2
Mass of the air = Density x Area = 1.229 x 0.0125
Mass of the air = 0.0153 kg/m
Acceleration = (Windspeed)^2 = (9.835)^2 = 96.727 m/s^2
Force = Mass x Acceleration
Wind Force = 0.0153 x 96.727
Wind Force = 1.4799 N

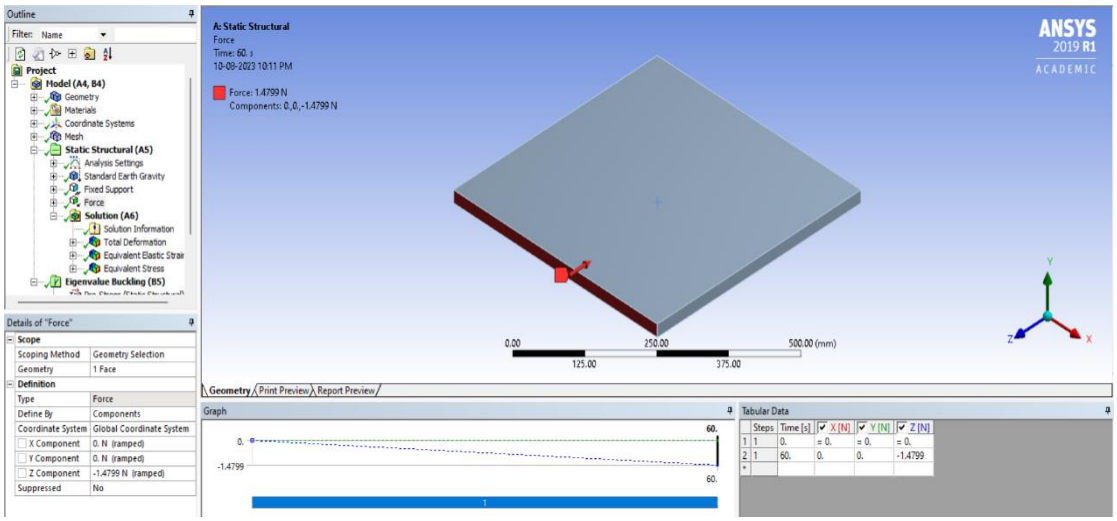

Figure 13: Wind Force on 500x500x25 mm Plate

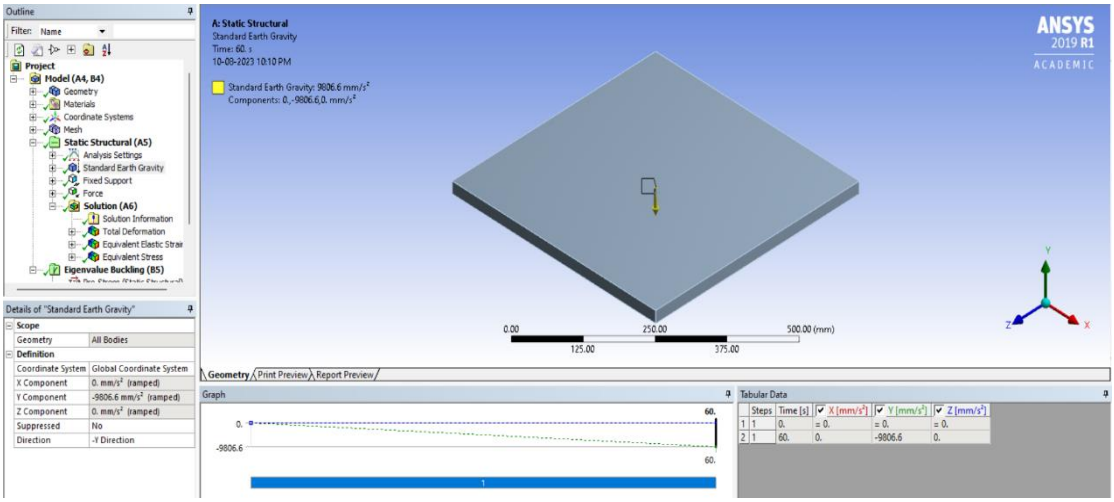

Figure 14: Earth Gravity on 500x500x25 mm Plate

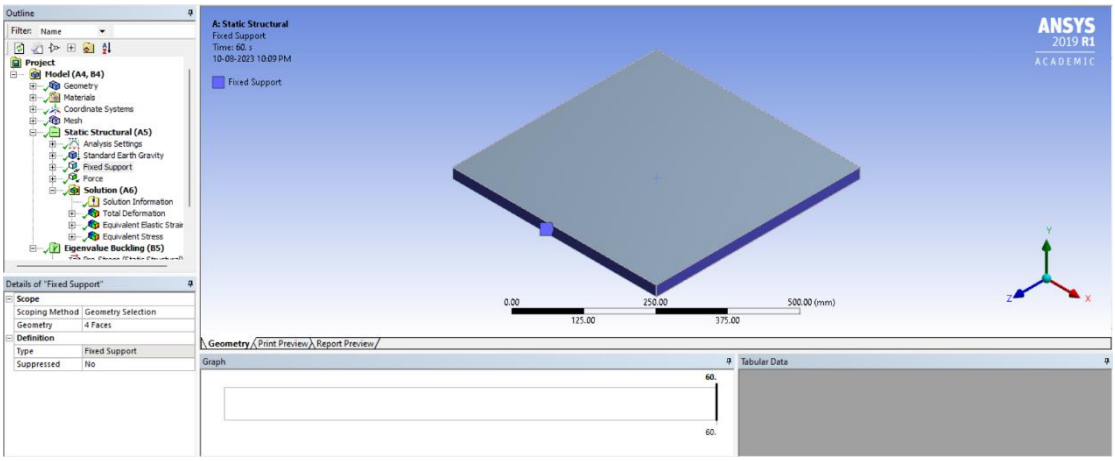

Figure 15: Fixed Support for 500x500x25 mm Plate

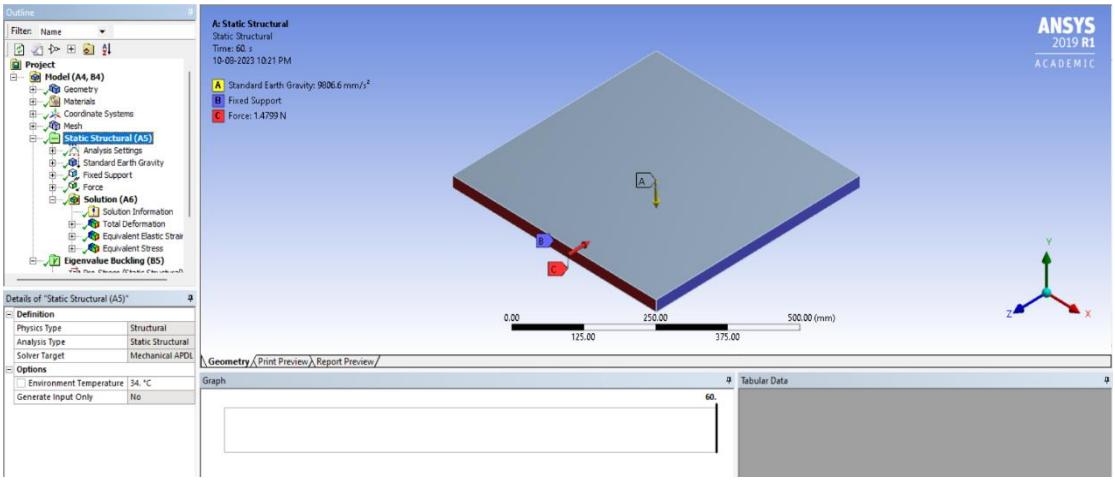

Figure 16: Temperature is taken for 500x500x25 mm Plate

4.5 FEA on External Fuel Tank of Launch Vehicle

Finite Element Analysis (FEA) is pivotal in evaluating intricate systems' structural integrity and safety, such as launch vehicles and their accompanying external fuel tanks. The external fuel tank of a launch vehicle is of critical importance since it supplies the necessary propellant for the rocket's engines.

- The launch vehicle's external fuel tank possesses a substantial propellant, rendering it a vital element of the launch vehicle. The structure must have the ability to endure the diverse range of loads and stresses encountered throughout different stages of the launch process, including liftoff, atmospheric pressures, and vibrations. Finite Element Analysis (FEA) is a valuable tool engineers use to effectively simulate and analyse the response of tanks to various loads. This process is crucial in ensuring the tank maintains its structural integrity and safety throughout its mission.
- To optimise their payload capacity, launch vehicles must possess minimal weight. Finite Element Analysis (FEA) enables engineers to comprehensively examine various material selections, designs, and combinations to identify the most favourable equilibrium between structural integrity and weight. The optimisation process has the potential to provide substantial cost savings through the reduction of material requirements while ensuring the preservation of safety margins.
- Finite Element Analysis (FEA) offers valuable insights into possible sources of failure inside the Electronic Funds Transfer (EFT) system. Engineers possess the capability to discern stress concentrations, places that are susceptible to buckling, and several other probable failure causes.

This information assists in the identification of design adjustments aimed at eliminating or mitigating these flaws before the launch, hence minimising the potential for catastrophic failure.

- Before constructing the external fuel tank, engineers can verify the soundness of their designs by employing Finite Element Analysis (FEA) simulations. The validation above method evaluates the tank's capacity to withstand the projected loads and stresses encountered during the launch. Identifying design problems early in development can prevent expensive redesigns and delays.[24]

4.5.1 Liquid Oxygen Tank

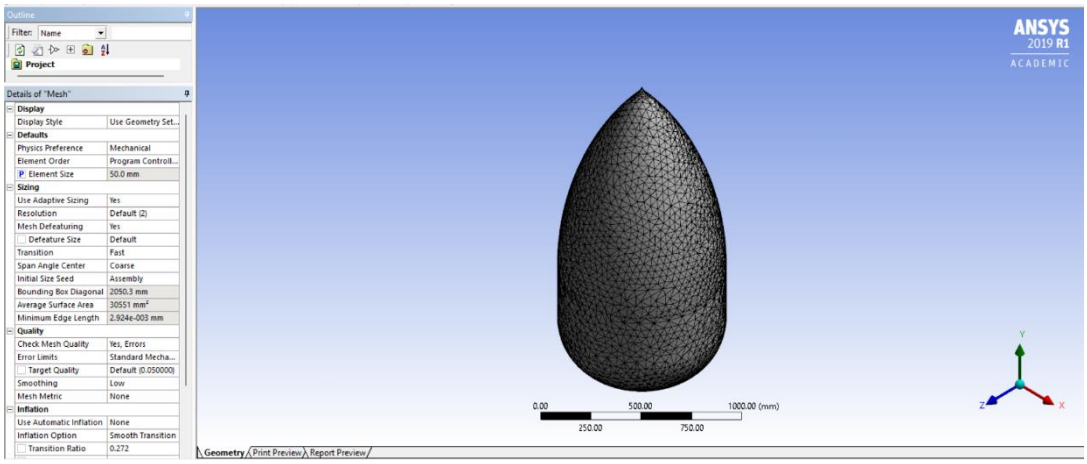

Figure 17: LOX Tank Mesh Settings

- Boundary Conditions for FEA Analysis

Wind Force Calculation[36]

Highest Temperature in Cornwall = 34°C
Wind Speed in Cornwall = 22 MPH = 9.835 m/s
Density of air at sea level = 1.229 kg/m^3
Area of the plate hitting by air = 747.9741 m^2
Mass of the air = Density x Area = 1.229 x 747.9741
Mass of the air = 919.26 kg/m
Acceleration = (Windspeed)^2 = (9.835)^2 = 96.727 m/s^2
Force = Mass x Acceleration
Wind Force = 919.26 x 96.727
Wind Force = 88916.79 N
Due to the RAM limitations and the massive size of the model, it has been scaled down by 1:10.
Wind Force = 88916.79 / 10
Wind Force = 8891.679 N

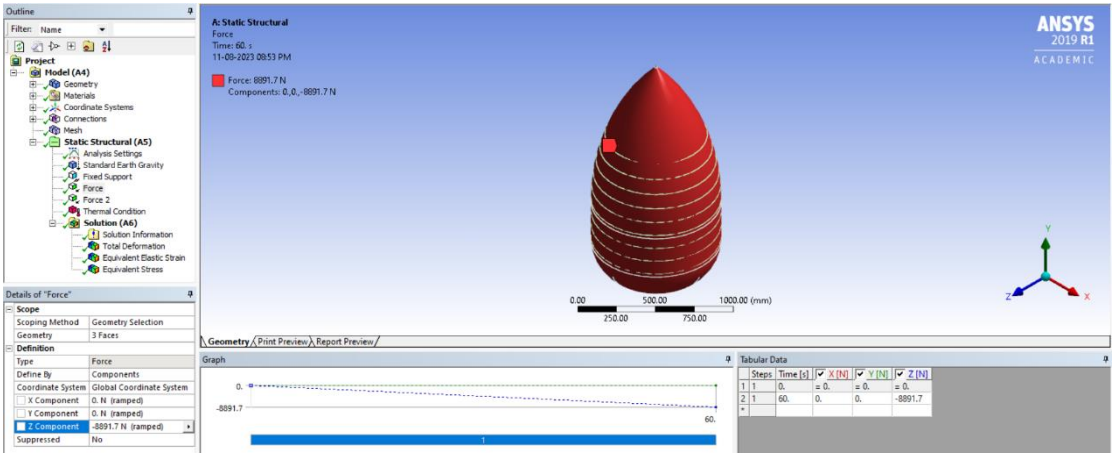

Figure 18: Wind Force on LOX Tank

- Fuel Weight Calculation

The External Fuel Tank of the Space Shuttle is a prominent illustration. As per NASA's findings, the extraterrestrial entity was equipped with distinct chambers designated for storing liquid hydrogen and liquid oxygen fuel. The Space Shuttle's main engines utilised these propellants to create thrust during launch. Fuel combustion resulted in a notable reduction in the tank's weight, causing a displacement in the overall centre of mass of the entire assembly, including the orbiter, solid rocket boosters, and the external tank. This change's management was necessary to ensure the maintenance of steady flying.

In the initial phases of ascent, the launch vehicle encounters the highest magnitudes of aerodynamic forces and is subject to the influences of thrust and gravity. The thrust-to-weight ratio of a vehicle is influenced by the reduction in mass resulting from fuel consumption. A more excellent thrust-to-weight ratio facilitates enhanced acceleration of the vehicle. Engineers meticulously compute and optimise the ratio above to guarantee a secure and effective ascension.

Moreover, the weight of the gasoline impacts the structural factors that need to be considered for the tank. The tank must possess the necessary structural integrity to endure the forces generated by the residual fuel, both in the first stage of ascent and during the acceleration period. The alteration influences the tank's structural integrity in internal pressure resulting from gasoline use. Managing the dynamic pressure change is crucial to avert tank buckling or failure.[37]

The density of Liquid Oxygen = 1.141 kg/L = 1.141 g/mL[38]
Amount of Liquid Oxygen in Tank = 145000 Gallons [39]
Kilograms = Gallons x 3.7854 x Density
Kilograms = 145000 x 3.7854 x 1.141
Fuel Force = 626277.45 N
Fuel Force = 626277.45 / 10
Fuel Force = 62627.745 N
Fuel temperature = - 147. 222^{o}

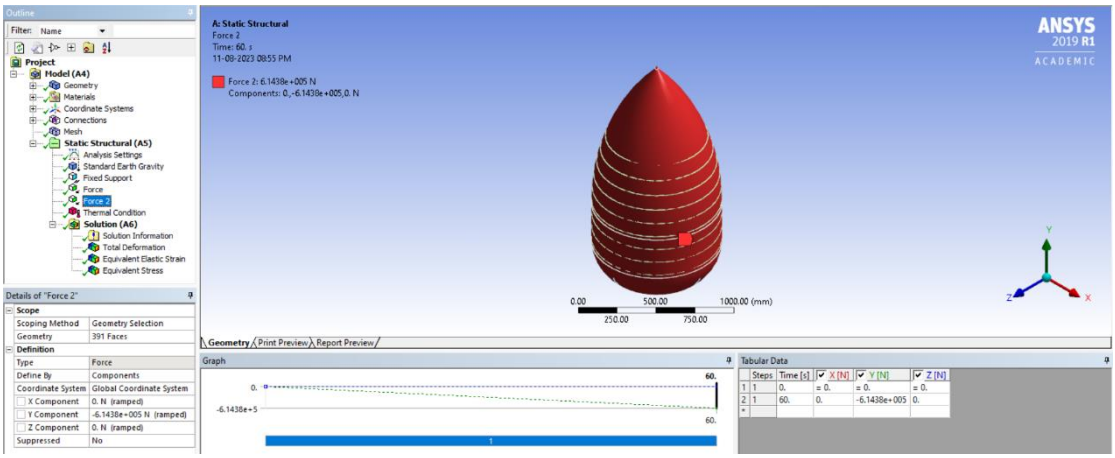

Figure 19: Fuel Force on LOX Tank

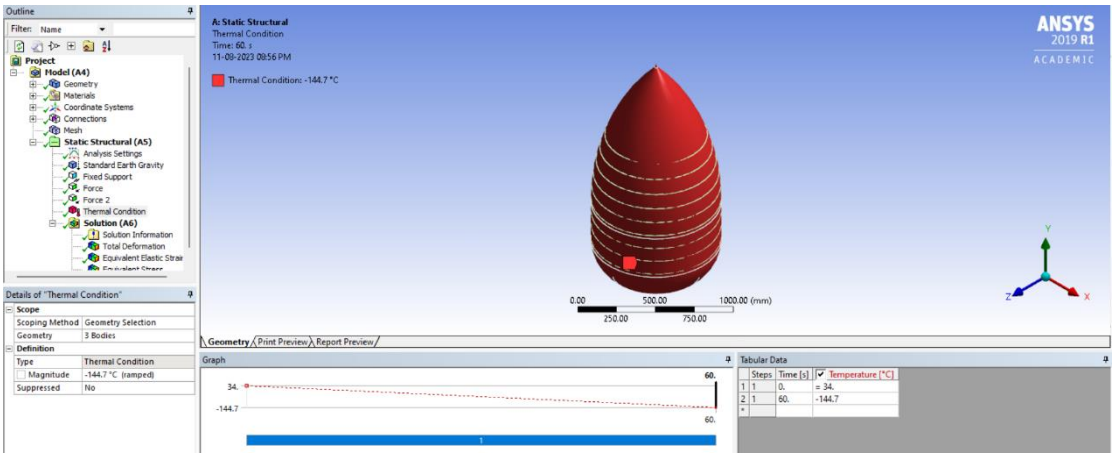

Figure 20: LOX Fuel Temperature

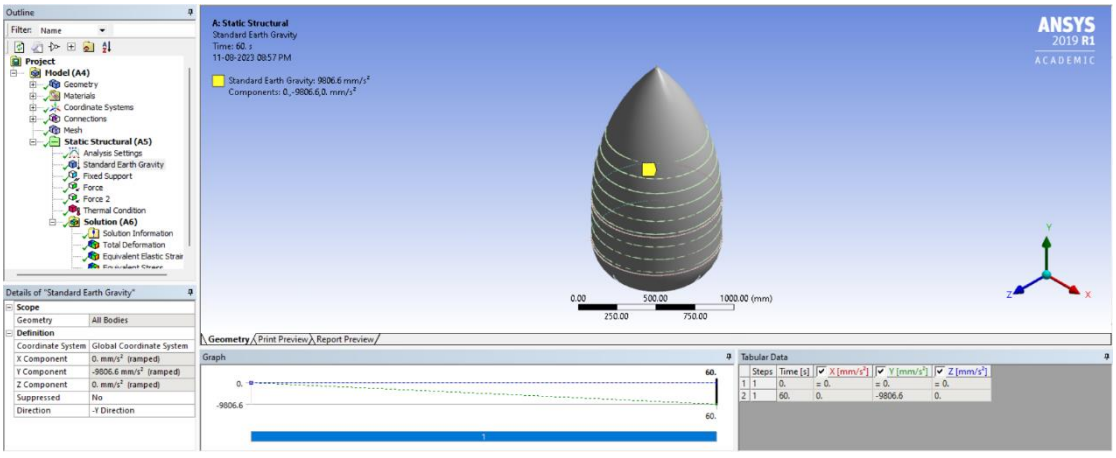

Figure 21: Earth Gravity on LOX Tank

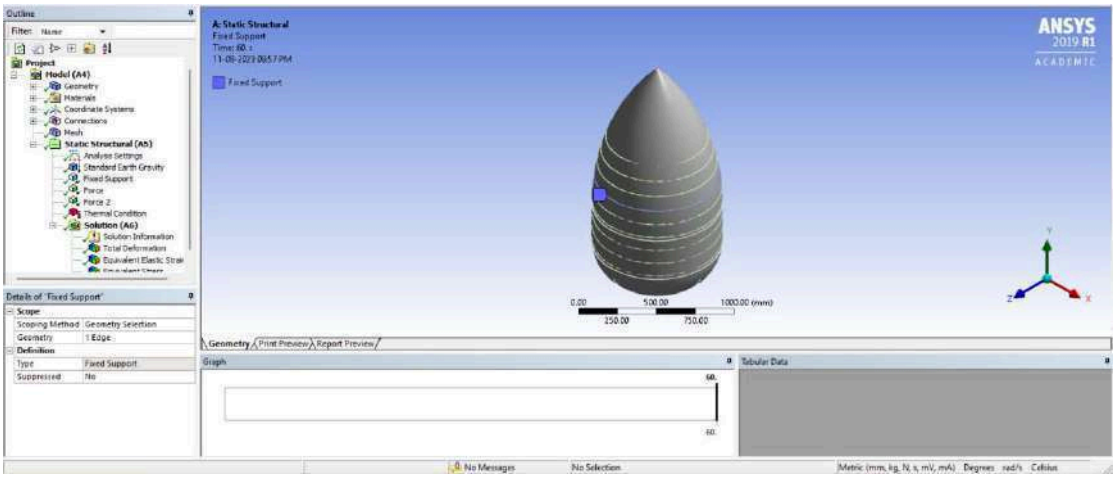

Figure 22: Fixed Support for LOX Tank

4.5.2 Intertank

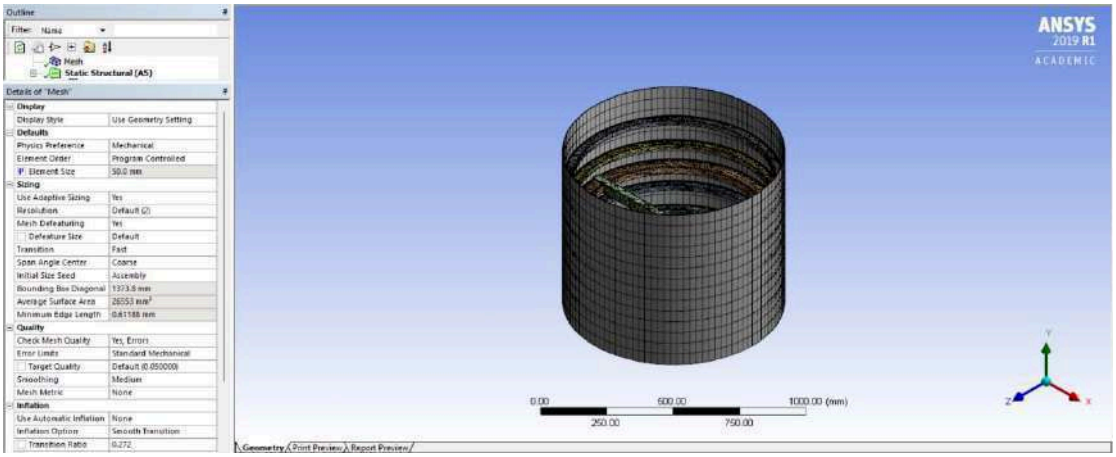

Figure 23: Intertank Mesh Settings

- Boundary Conditions for FEA Analysis

Wind Force Calculation[36]

Highest Temperature in Cornwall = 34°C
Wind Speed in Cornwall = 22 MPH = 9.835 m/s
Density of air at sea level = 1.229 kg/m^3
The area of the plate hitting by air = 182.087 m^2
Mass of the air = Density x Area = 1.229 x 182.087
Mass of the air = 223.785 kg/m
Acceleration = (Windspeed)^2 = (9.835)^2 = 96.727 m/s^2
Force = Mass x Acceleration
Wind Force = 223.785 x 96.727
Wind Force = 21646.044 N
Due to the RAM limitations and the massive size of the model, it has been scaled down by 1:10.
Wind Force = 21646.044 / 10
Wind Force = 2164.6044 N

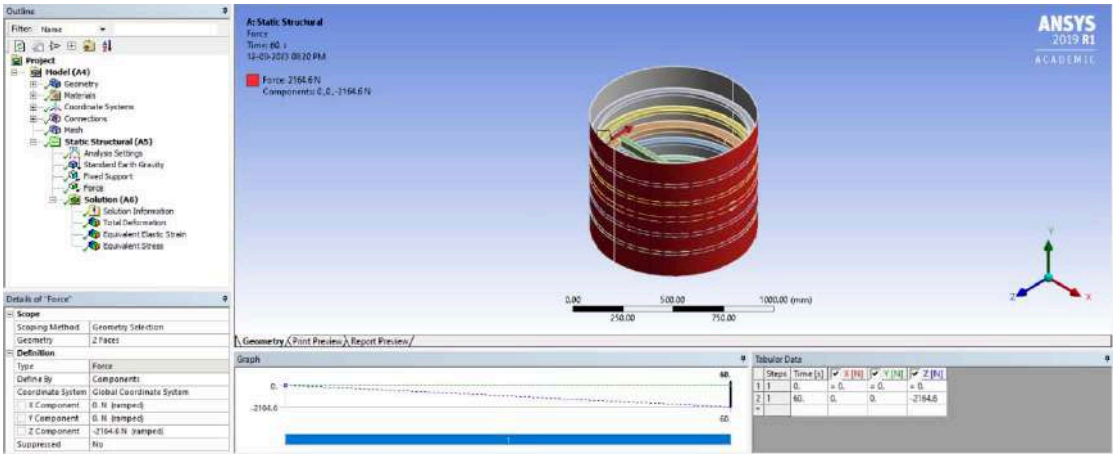

Figure 24: Wind Force on Intertank

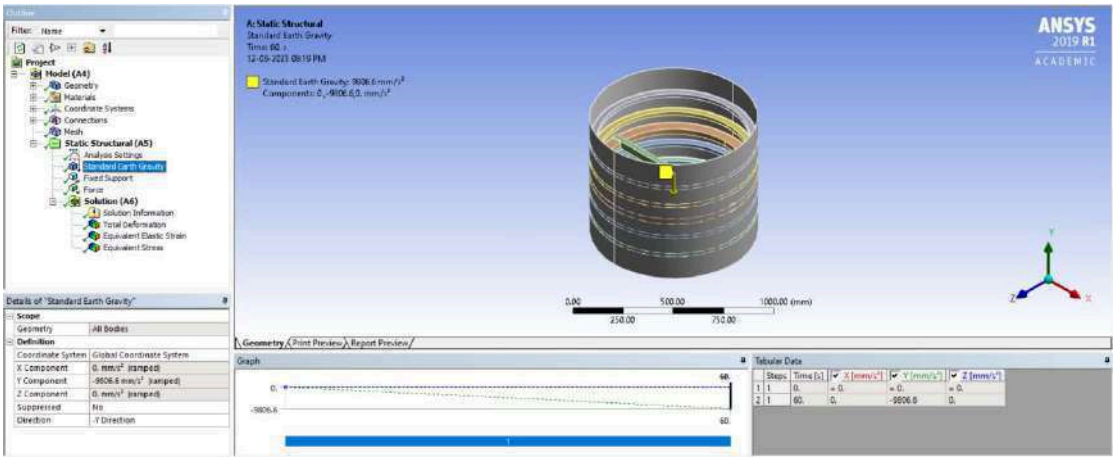

Figure 25: Earth Gravity on Intertank

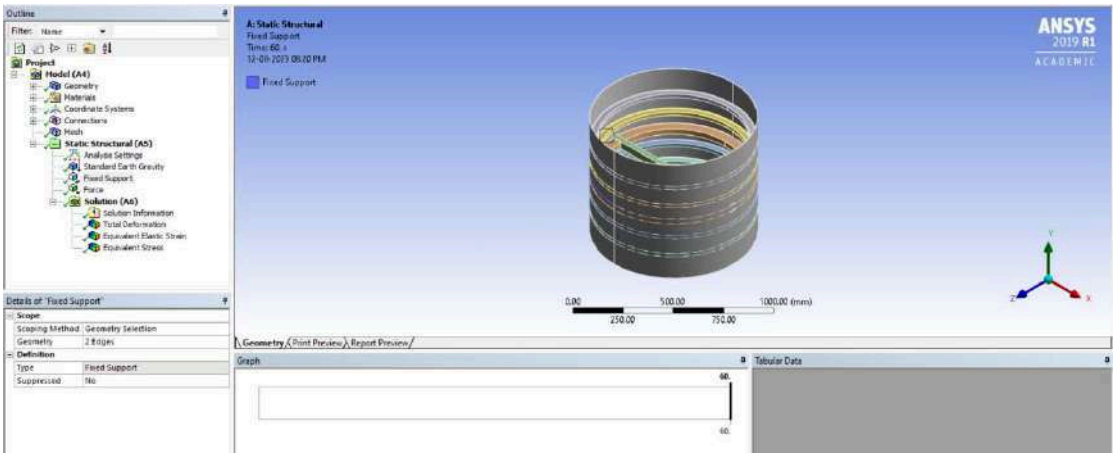

Figure 26: Fixed Support for Intertank

4.5.3 Liquid Hydrogen Tank

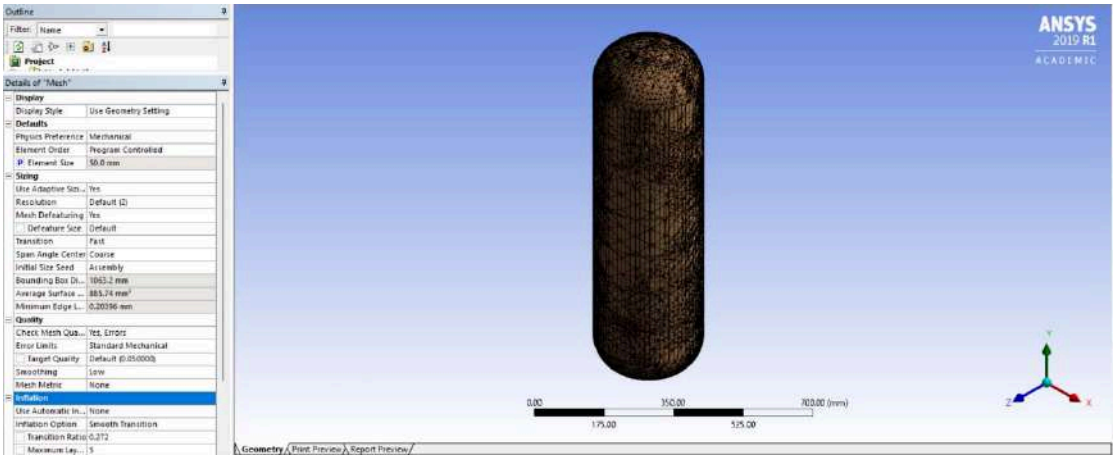

Figure 27: LH2 Tank Mesh Settings

- Boundary Conditions for FEA Analysis

Wind Force Calculation[36]

Highest Temperature in Cornwall = 34°C
Wind Speed in Cornwall = 22 MPH = 9.835 m/s
Density of air at sea level = 1.229 kg/m^3
Area of the plate hitting by air = 1603.89 m^2
Mass of the air = Density x Area = 1.229 x 1603.89
Mass of the air = 1971.18 kg/m
Acceleration = (Windspeed)^2 = (9.835)^2 = 96.727 m/s^2
Force = Mass x Acceleration
Wind Force = 1971.18 x 96.727
Wind Force = 190666.41 N
Due to the RAM limitations and the massive size of the model, it has been scaled down by 1:30.
Wind Force = 190666.41 / 30
Wind Force = 6355.547 N

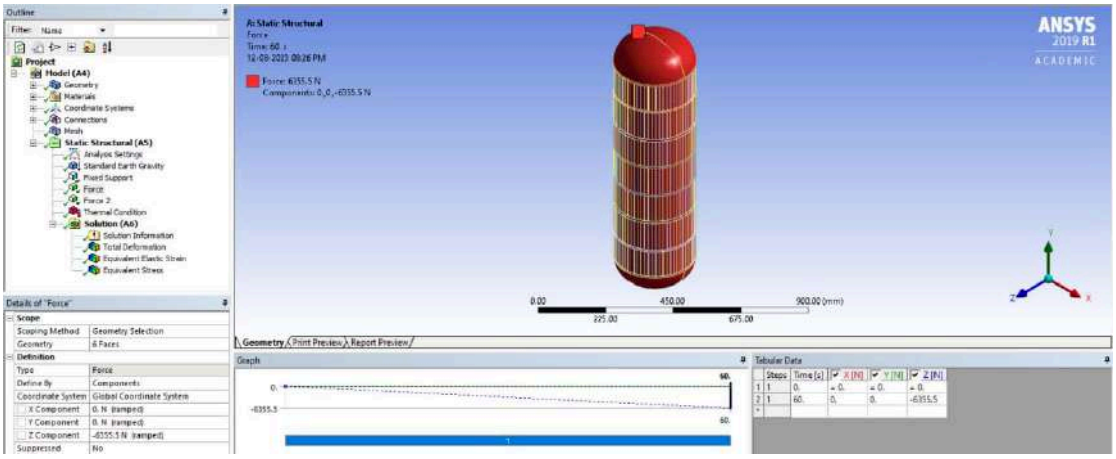

Figure 28: Wind Force on LH2 Tan

Fuel Weight Calculation
The density of Liquid Oxygen = 0.07085kg/L = 0.07085 g/mL[40]
Amount of Liquid Oxygen in Tank = 390000 Gallons[39]

Kilograms = Gallons x 3.7854 x Density
Kilograms = 390000 x 3.7854 x 0.07085
Fuel Force = 1042420.41 N
Fuel Force = 1042420.41 / 30
Fuel Force = 34747.347 N
Fuel temperature = - 253^{o}C

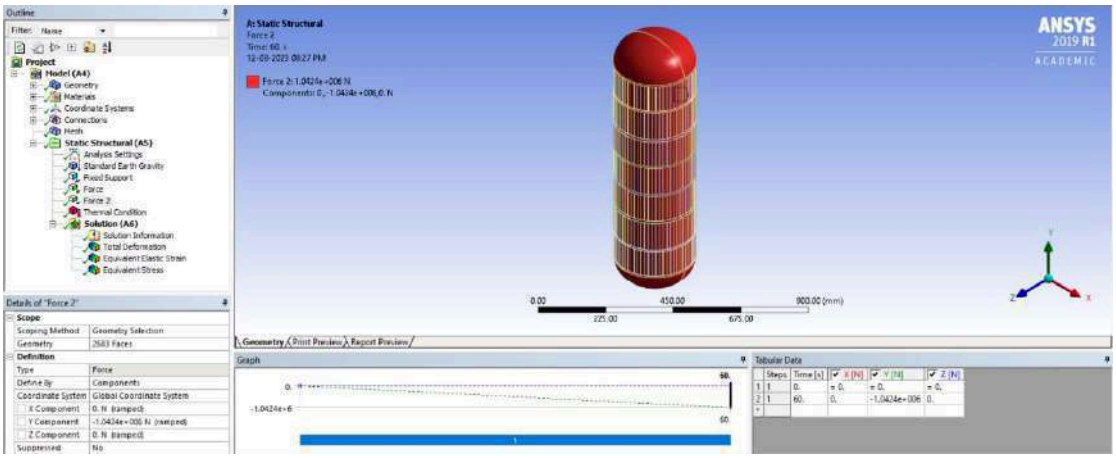

Figure 29: Fuel Force on LH2 Tank

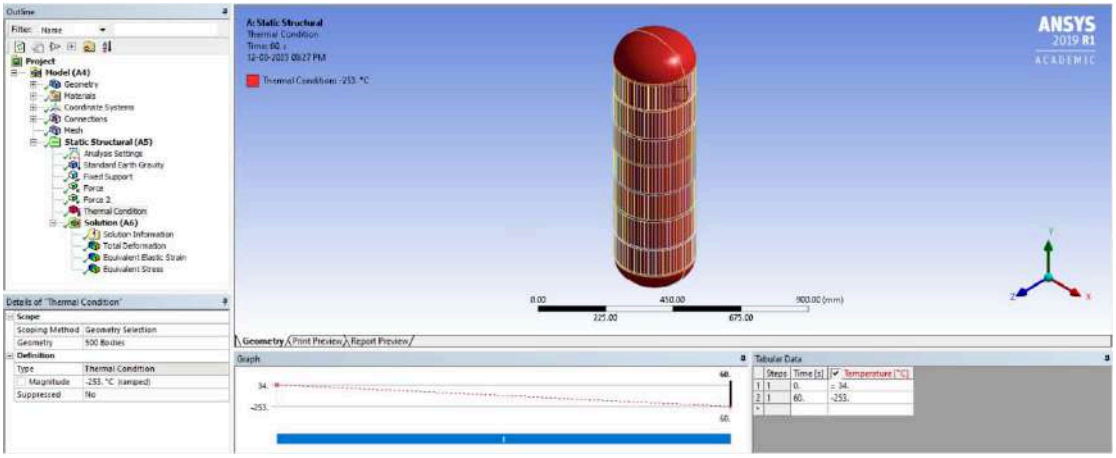

Figure 30: LH2 Fuel Temperature

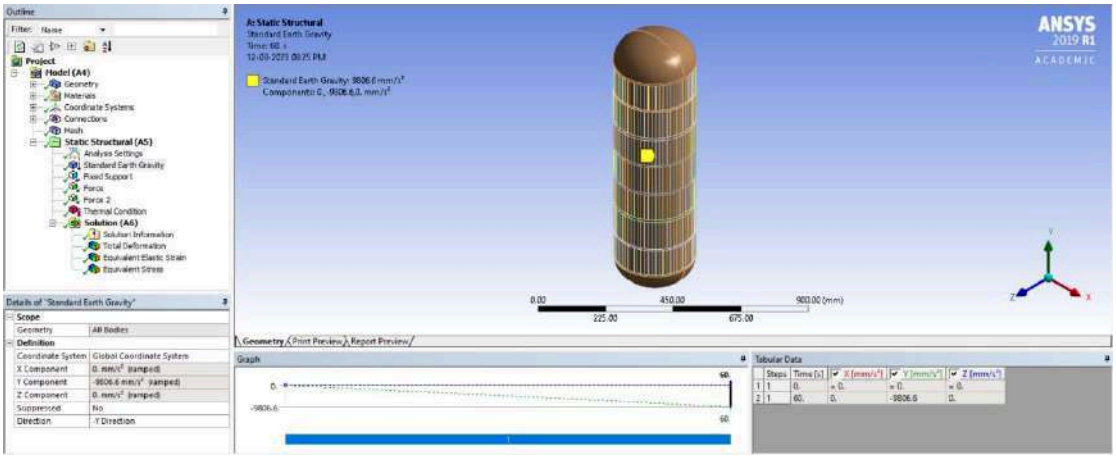

Figure 31: Earth Gravity on LH2 Tank

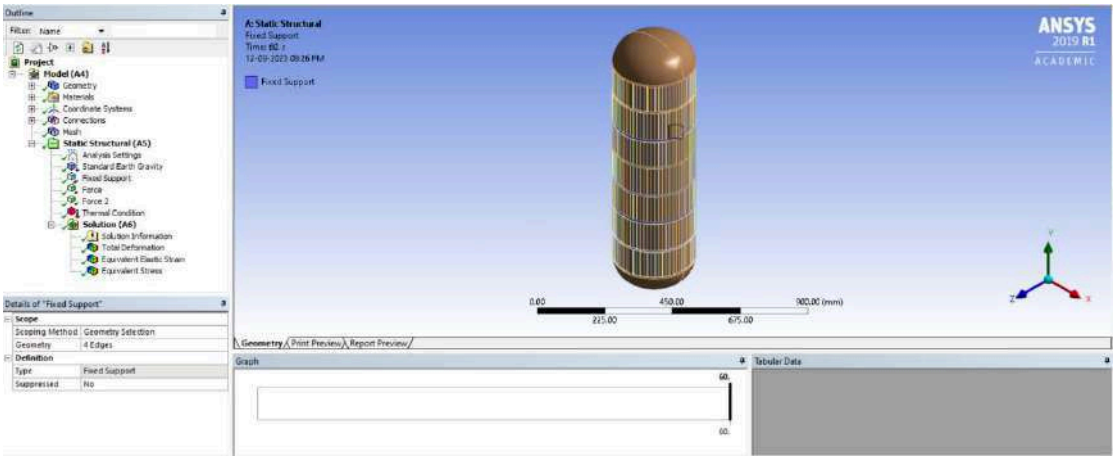

Figure 32: Fixed Support for LH2 Tank

4.5.4 External Fuel Tank of Launch Vehicle

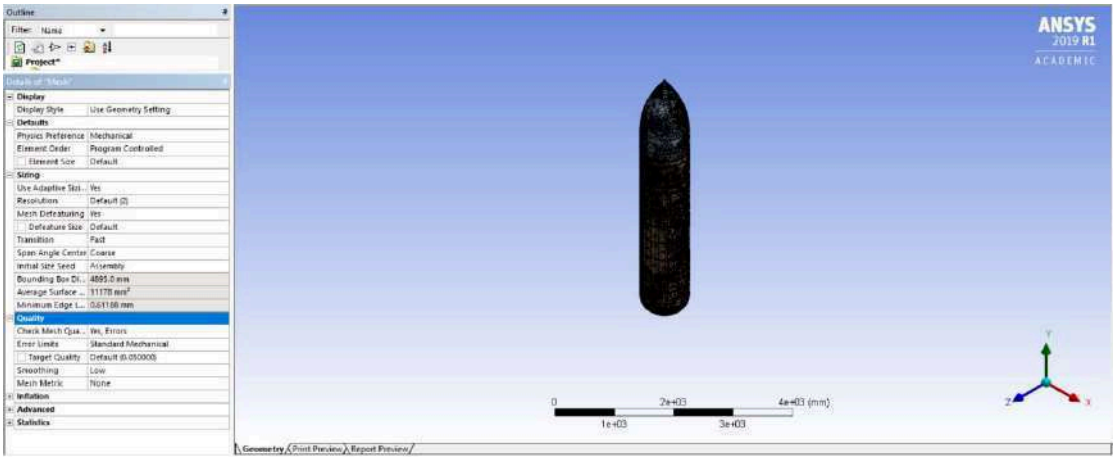

Figure 33: EFT Mesh Settings

- Boundary Conditions for FEA Analysis

Wind Force Calculation[36]

It is assumed that the launch will happen in Cornwall City, and wind will flow in the -Z Direction as the geometry is symmetric.
Highest Temperature in Cornwall = 34°C
Wind Speed in Cornwall = 22 MPH = 9.835 m/s
Density of air at sea level = 1.229 kg/m^3
Area of the plate hitting by air = 3872.0835 m^2
Mass of the air = Density x Area = 1.229 x 3872.0835
Mass of the air = 4758.7906 kg/m
Acceleration = (Windspeed)^2 = (9.835)^2 = 96.727 m/s^2
Force = Mass x Acceleration
Wind Force = 4758.7906 x 96.727
Wind Force = 331816.1937 N
Due to the RAM limitations and the massive size of the model, it has been scaled down by 1:10.
Wind Force = 331816.1937 / 10
Wind Force = 33181.61937 N

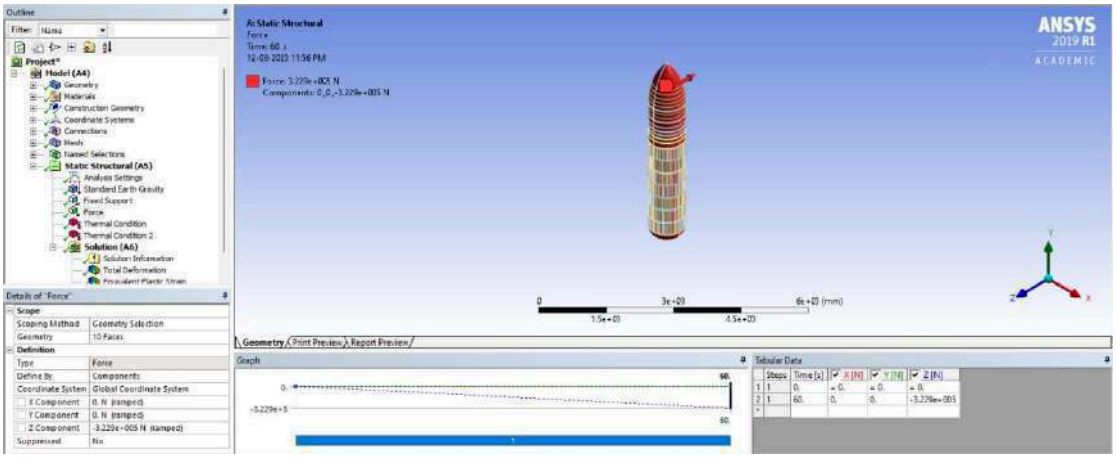

Figure 34: Wind Force on EFT

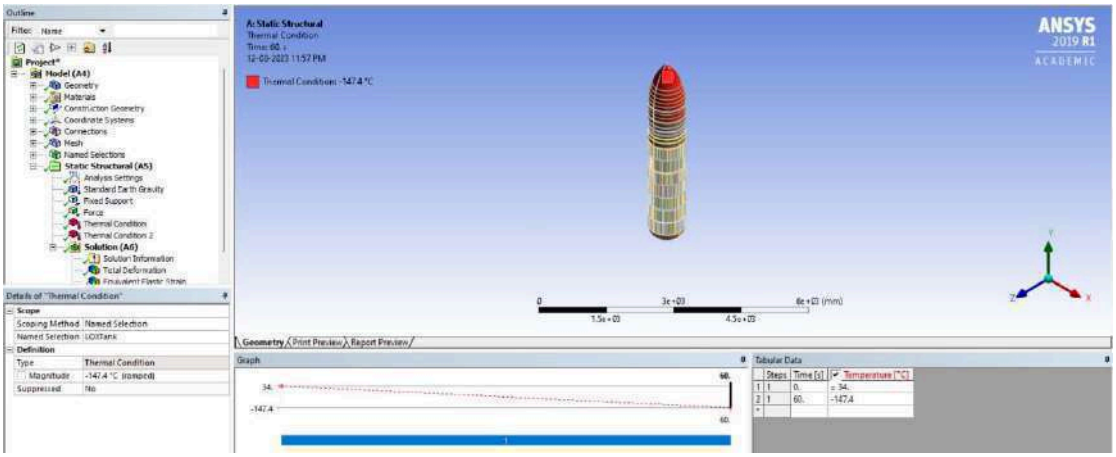

Figure 35: LOX Fuel Temperature

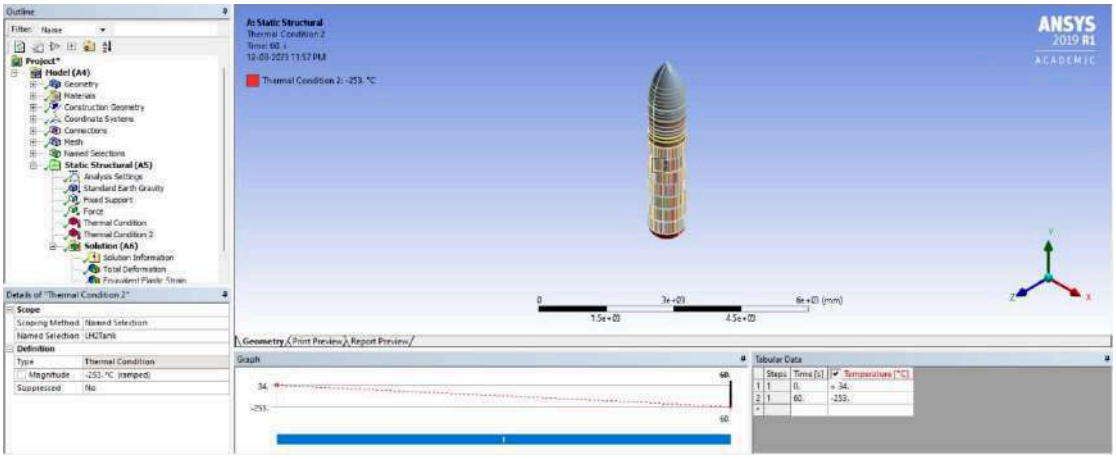

Figure 36: LH2 Fuel Temperature

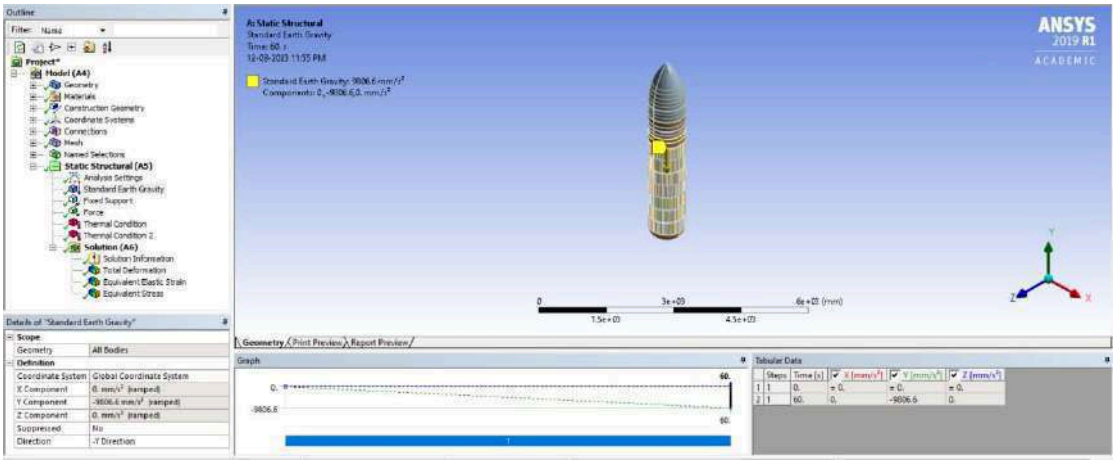

Figure 37: Earth Gravity on EFT

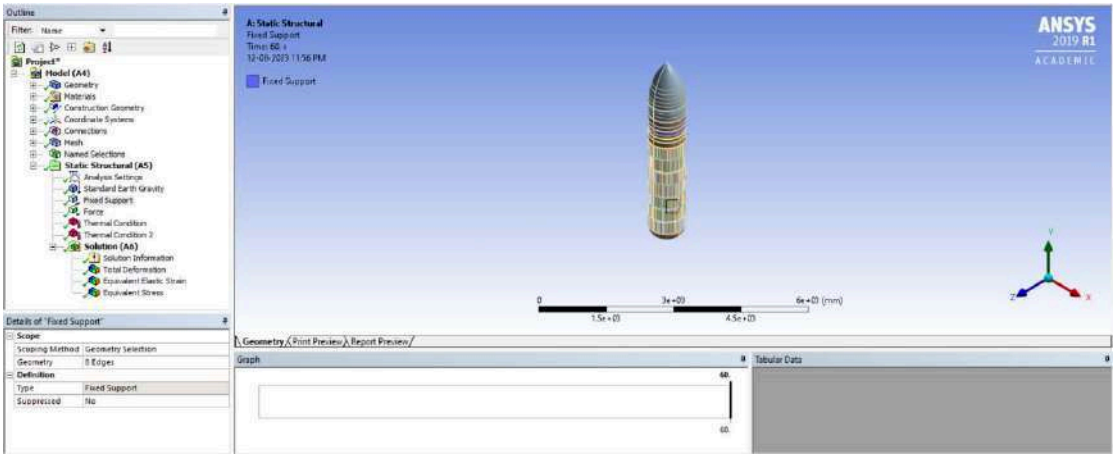

Figure 38: Fixed Support for EFT

V. RESULTS

5.1 500x500x25 mm Plate

Deformation outcomes in ANSYS Workbench may often be represented as total or directed deformation. Both of these methods are used to derive displacements based on the analysis of stresses. In this particular instance, the overall distortion has been duly considered. The observed maximum deformation was 0.00051977 mm, indicating a very modest magnitude.

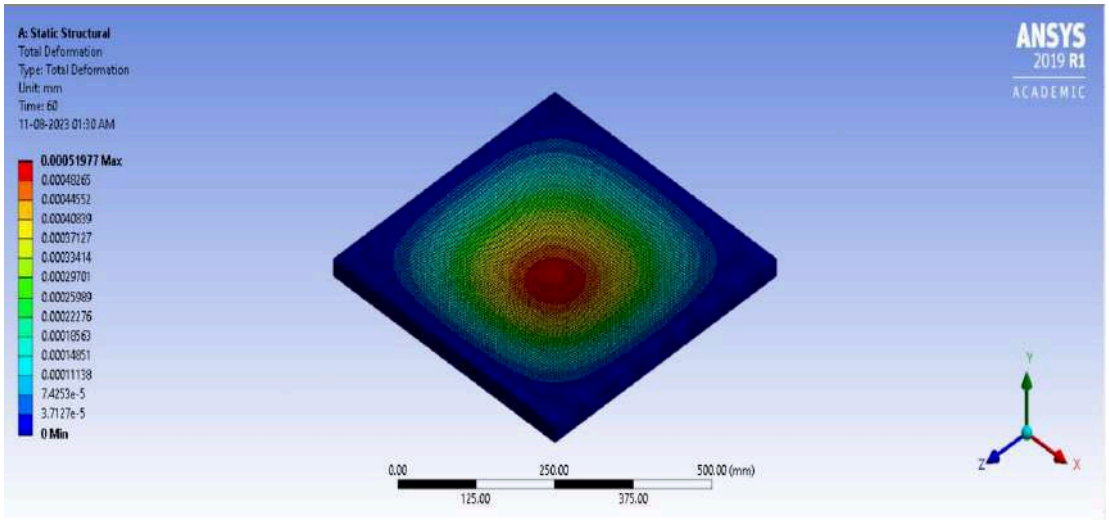

Figure 39: 500x500x25 mm Plate's Total Deformation

According to the data shown in Figure 40, the highest equivalent stress observed on the plate is determined to be 0.07055 Mpa. The yield strength of aluminium alloy 2195 is measured to be 230 megapascals (MPa). The most incredible equivalent stress experienced by the plate is determined to be 0.07 MPa, a value far lower than the yield strength.

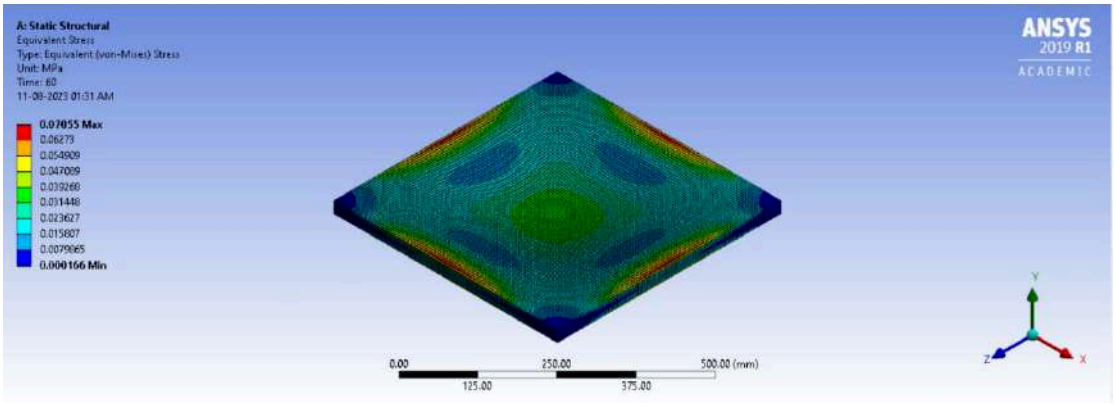

Figure 40: 500x500x25 mm Plate's Equivalent Stress

Figure 41 depicts the Equivalent elastic strain acting on the plate. The maximum strain that has been acting on the plate is 9.95 e^{-7}.

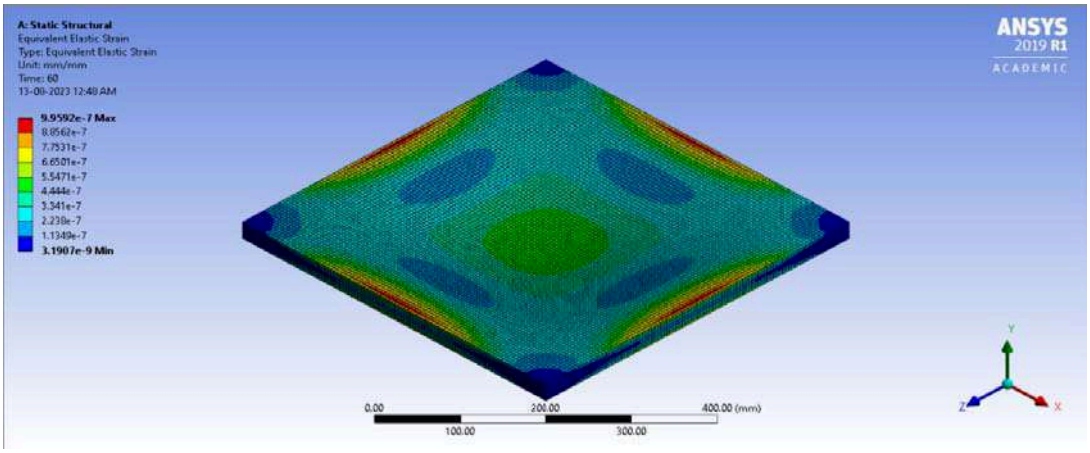

Figure 41: 500x500x25 mm Plate's Equivalent Elastic Strain

5.2 Liquid Oxygen Tank

Figure 42 and Figure 43 represent the total deformation of the LOX Tank as well as a sectional view of the LOX Tank's total deformation, respectively. It was determined that the tank had a maximum distortion of 12.354 millimetres. The model is scaled down by 1:10, so the maximum deformation is 123.54 mm. In addition, the precise position of the highest deformation created is shown in Figure 43. Even if the degree of deformation is rather significant, fatigue is still possible with repeated use; this will need to be investigated.

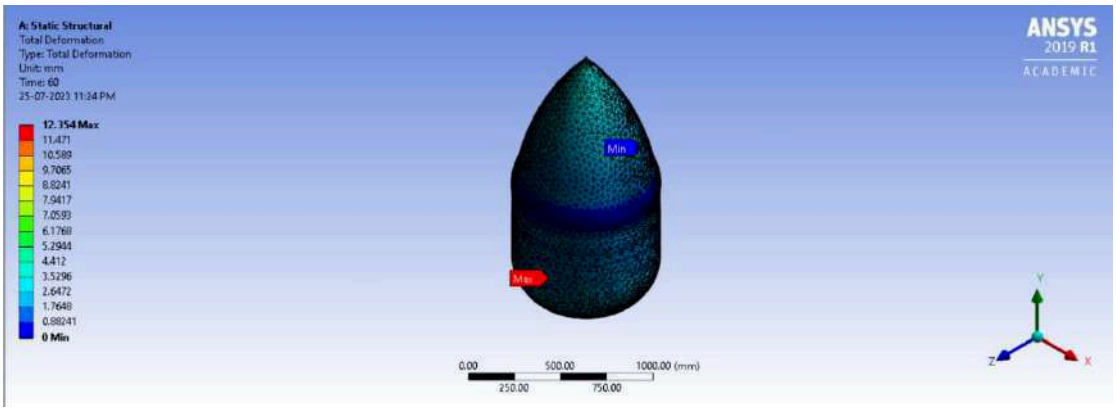

Figure 42: LOX Tank's Total Deformation

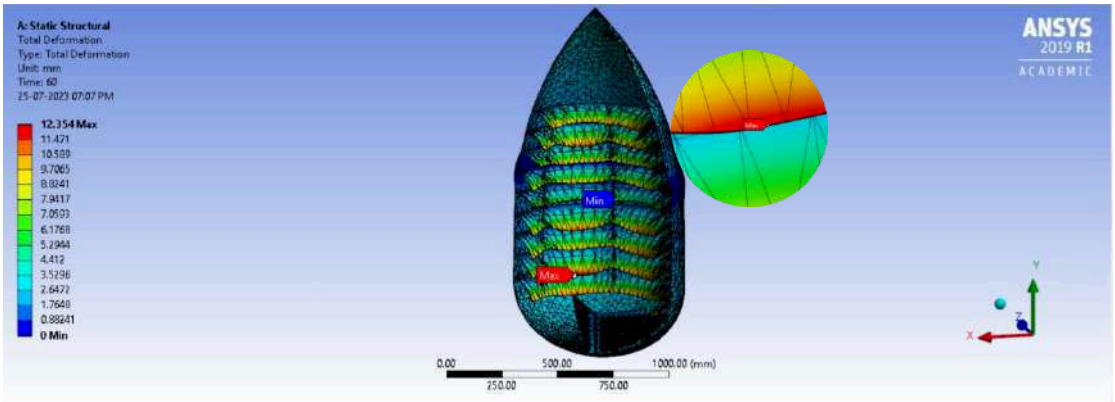

Figure 43: Sectional View of LOX Tank's Total Deformation

Figures 44 and 45 show the equivalent stress on the LOX Tank. The maximum stress was found to be 14898.0 MPa. Although most of the tanks had equivalent stress between 1.9758 MPa and 1657.1 Mpa,there have been very few points on the LOX tank's surface where the stresses reached up to 14898.0 MPa. This will lead to the tank breaking as it exceeds the yield stress point.

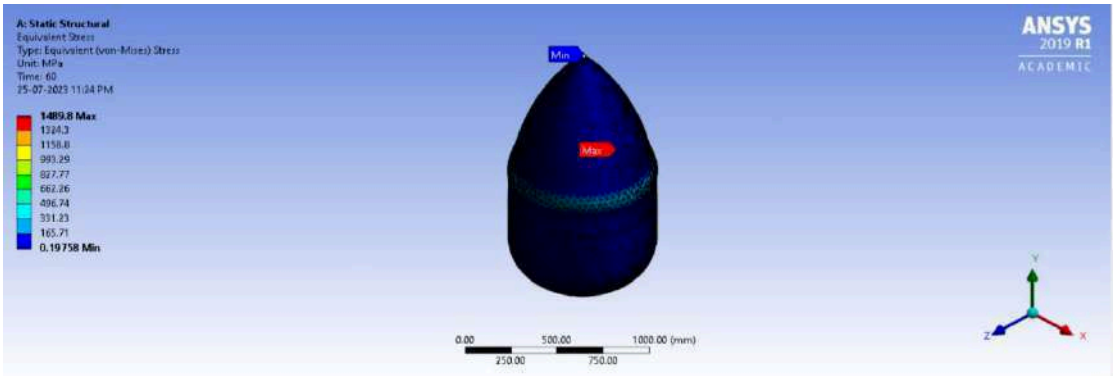

Figure 44: LOX Tank's Equivalent Stress

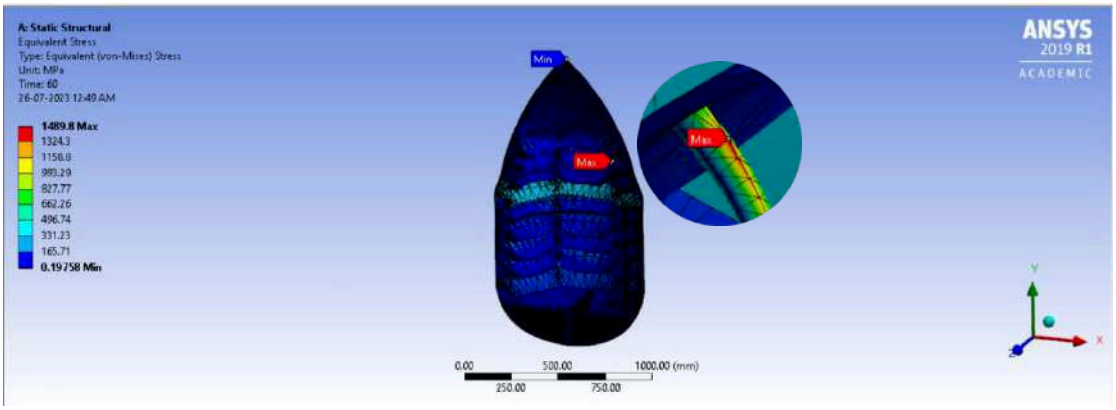

Figure 45: Sectional View of LOX Tank's Equivalent Stress

Figures 46 and 47 show the Equivalent elastic strain of the fuel tank. The maximum strain on the fuel tank is found to be 0.21081.

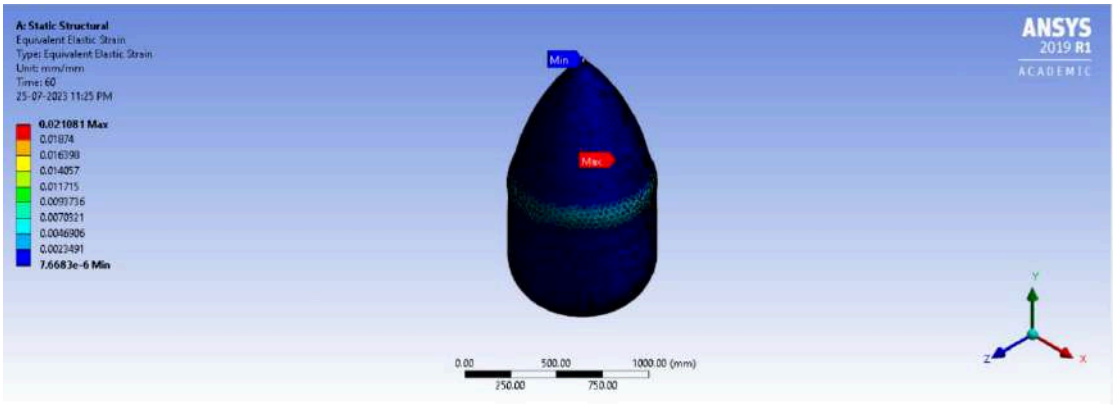

Figure 46: LOX Tank's Equivalent Elastic Strain

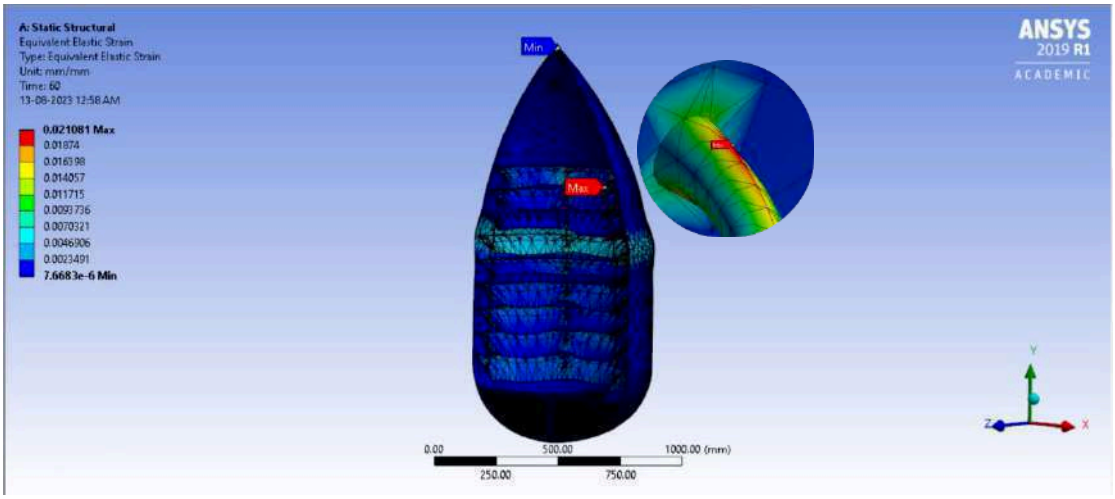

Figure 47: Sectional View of LOX Tank's Equivalent Elastic Strain

5.3 Intertank

Figure 48 illustrates the total deformation of the Intertank, while Figure 49 presents a sectional view of the total deformation of the Intertank. The investigation revealed that the tank had a maximum deformation of 0.022 mm. The model is scaled down by 1:10. The maximum deformation is 0.22508

mm. Figure 49 depicts the precise spot where the most significant degree of deformation has been generated as an outcome of the loads acting. Despite the negligible magnitude of distortion, which may not need explicit acknowledgement, there is no possibility that prolonged use might result in fatigue.

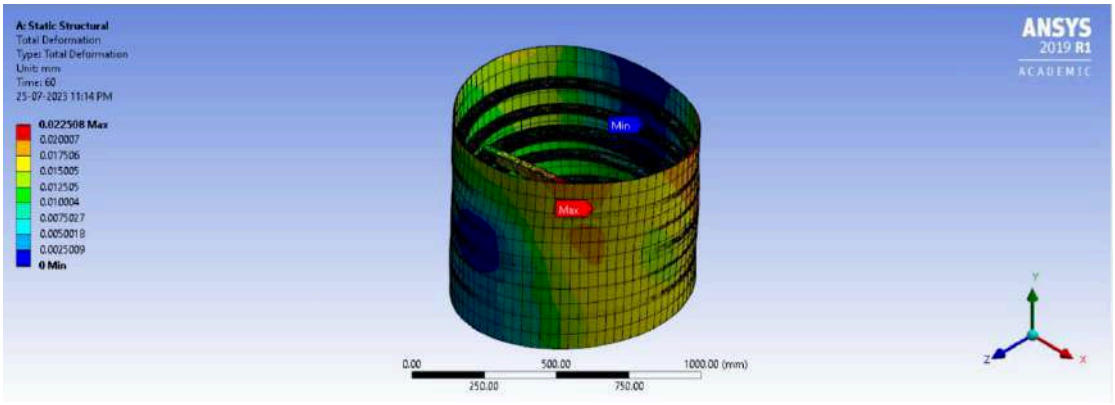

Figure 48: Intertank's Total Deformation

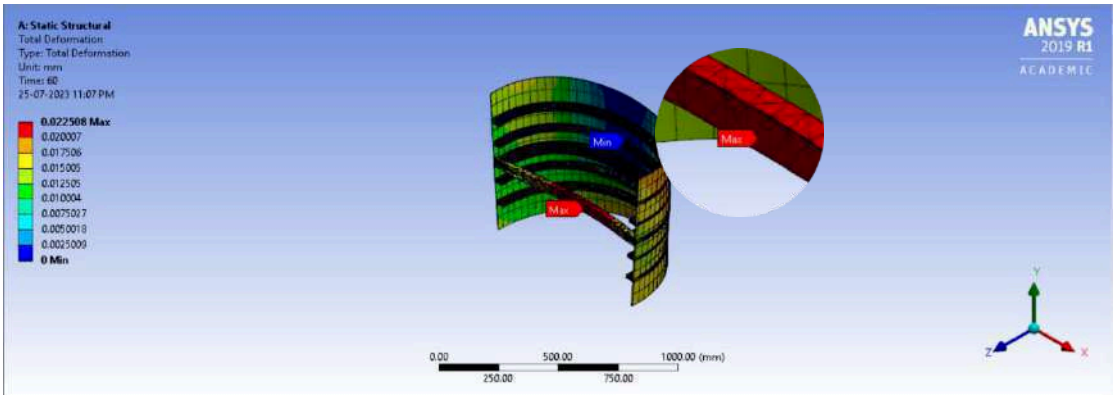

Figure 49: Sectional View of Intertank's Total Deformation

Figures 50 and 51 depict the similar stress experienced by the Intertank. The investigation determined that the most significant stress observed was 31.246 MPa. The majority of the tank's surface exhibited deficient levels of stress. There is no potential for fatigue in this particular circumstance, unlike the scenario described in section 4.2.

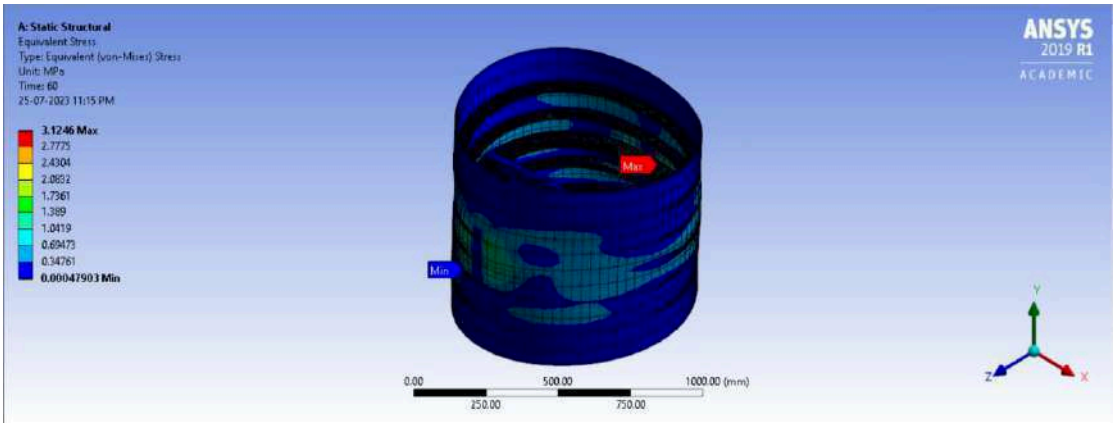

Figure 50: Intertank's Equivalent Stress

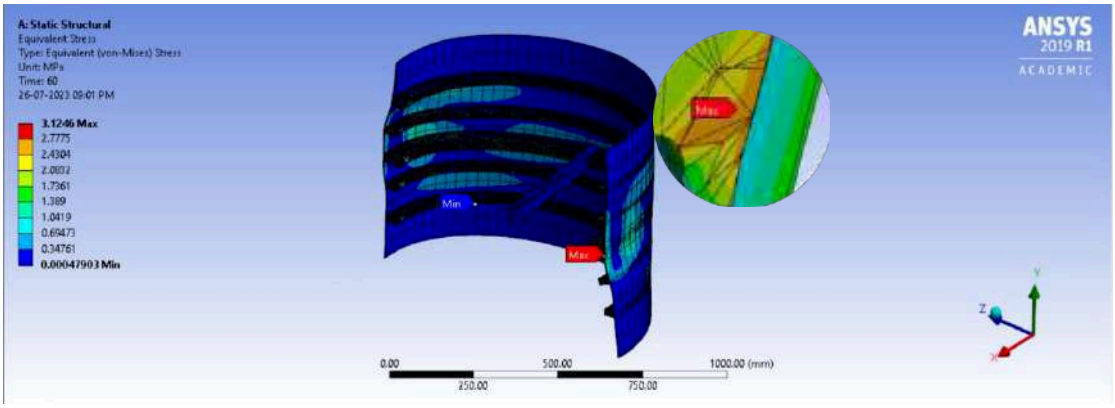

Figure 51: Sectional View of Intertank's Equivalent Stress

Figure 52 and 53 shows the Equivalent elastic strain of the fuel tank. The maximum strain on the fuel tank is found to be 4.65 e^{-4}.

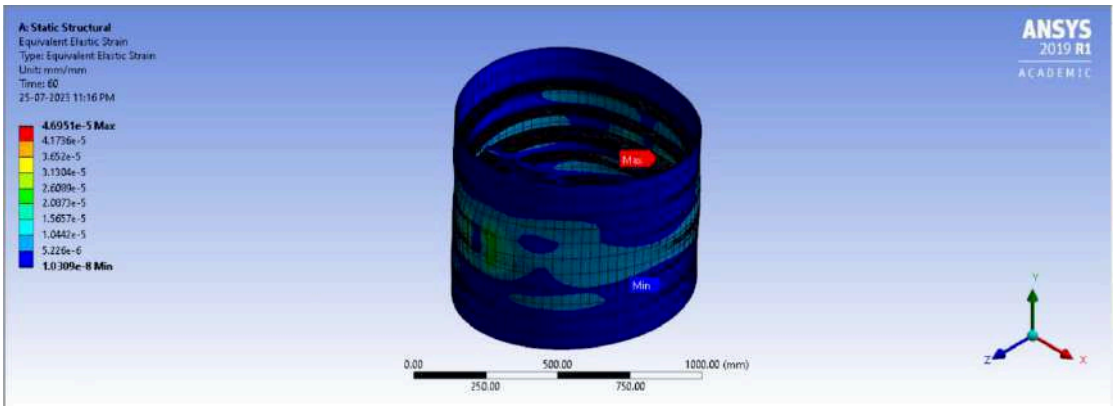

Figure 52: Intertank's Equivalent Elastic Strain

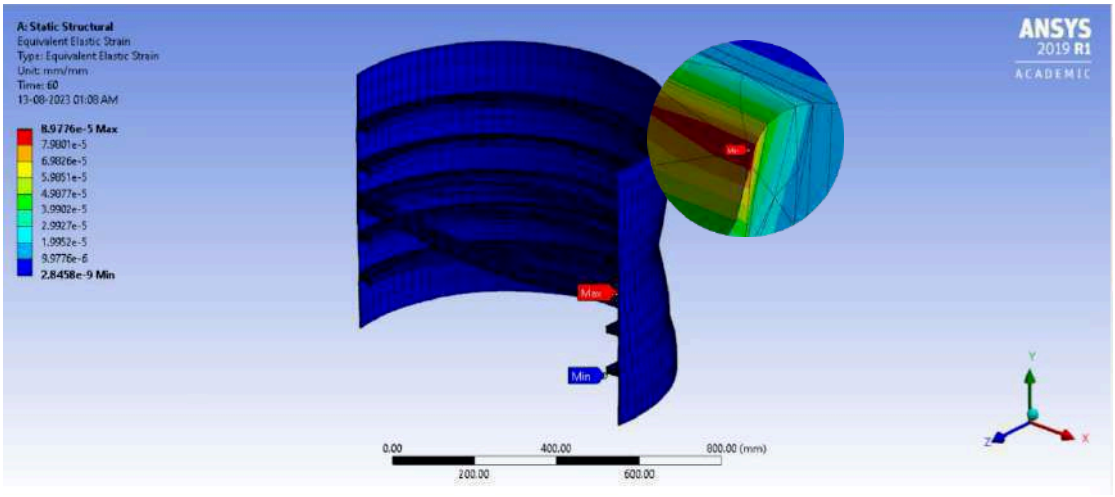

Figure 53: Sectional View of Intertank's Equivalent Elastic Strain

5.4 Liquid Hydrogen Tank

Figure 54 depicts the total deformation of the Liquid Hydrogen Tank, while Figure 55 provides a cross-sectional perspective of the overall deformation of the Liquid Hydrogen Tank. The examination findings indicated that the tank exhibited a maximum deformation of 3.6 mm. This model is scaled

down by 1:30. Maximum deformation is 108 mm. Figure 55 illustrates the specific location where the most amount of deformation has been created as a result of the applied loads.

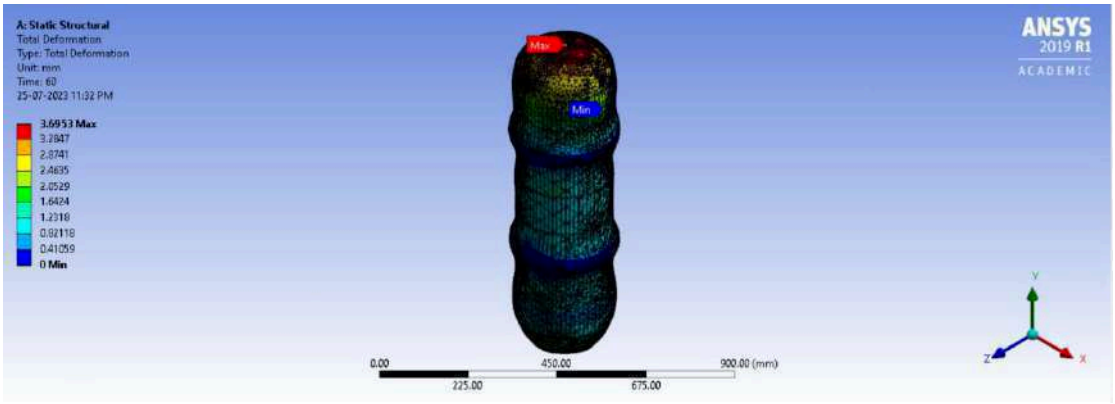

Figure 54: LH2's Total Deformation

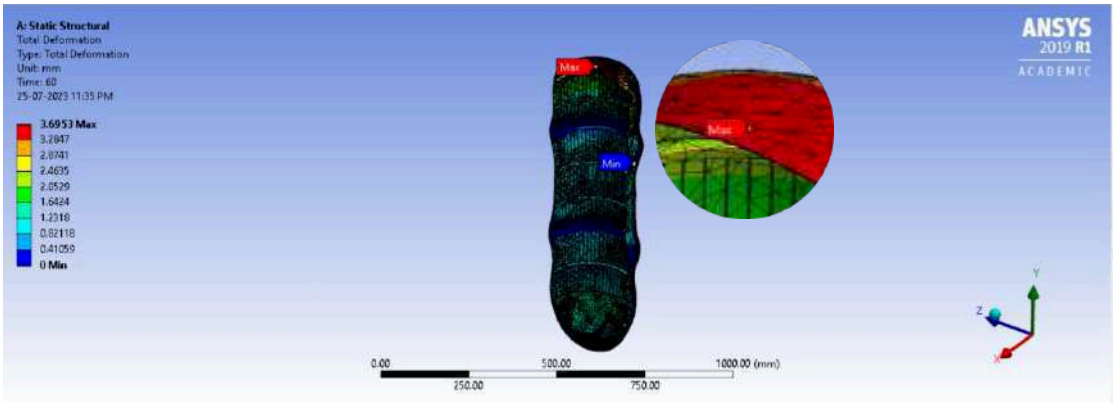

Figure 55: Sectional View of LH2's Total Deformation

Figures 56 and 57 depict the equivalent stress experienced by the LH2 Tank. The experimental analysis yielded a maximum stress value of 2706.9 MPa. So, the model is scaled down by 1:30. Maximum stress is 81270 MPa.

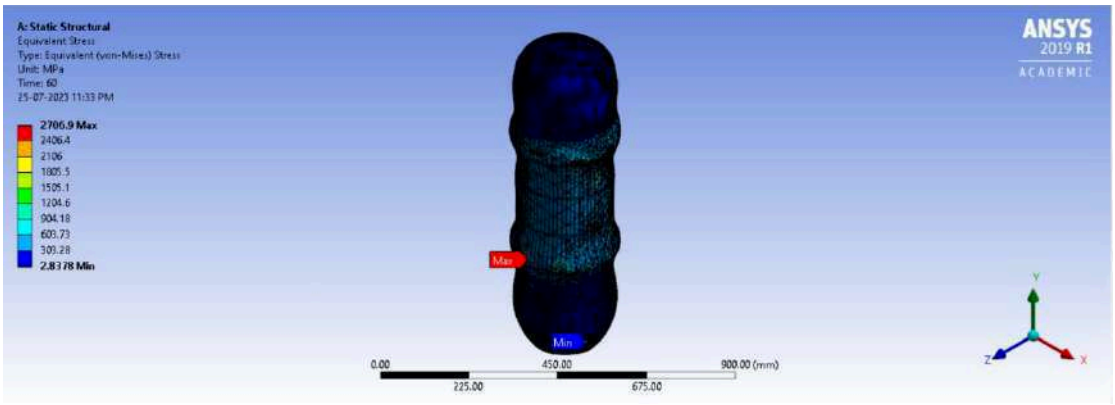

Figure 56: LH2's Equivalent Stress

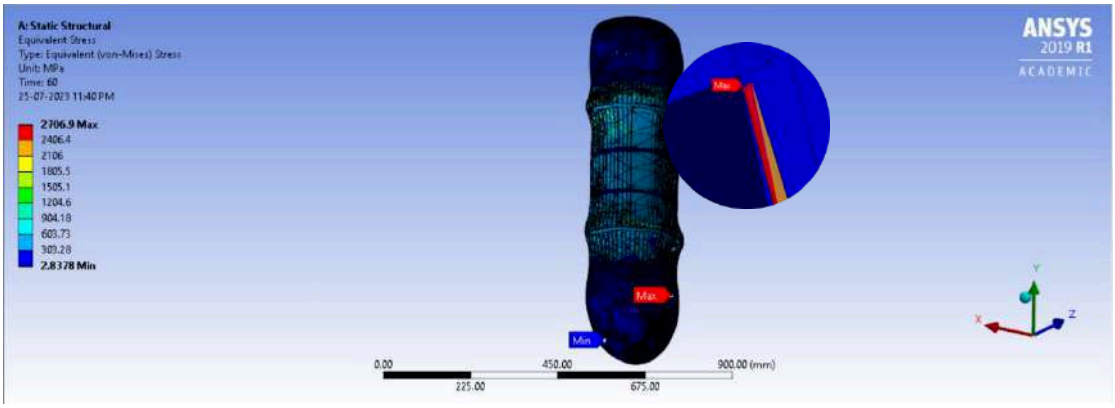

Figure 57: Sectional View of LH2's Equivalent Stress

Figures 58 and 59 show the Equivalent elastic strain of the fuel tank. The maximum strain on the fuel tank is found to be 1.1437.

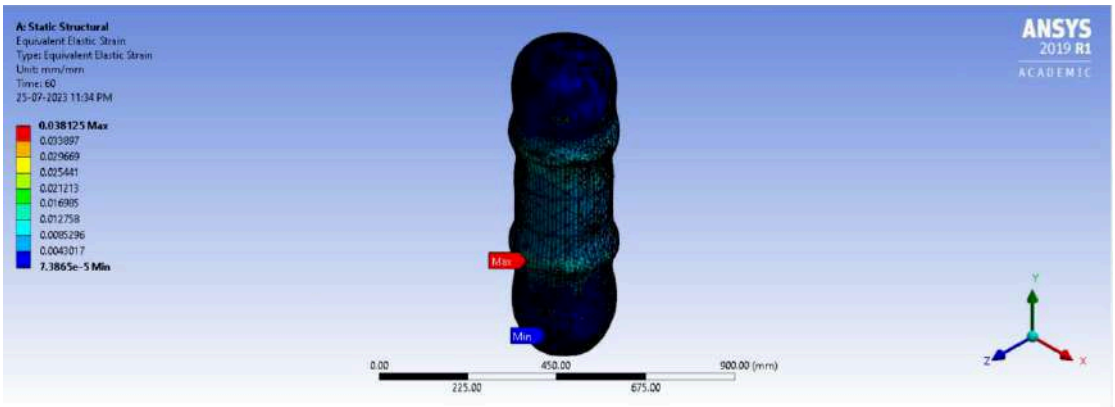

Figure 58: LH2's Equivalent Elastic Strain

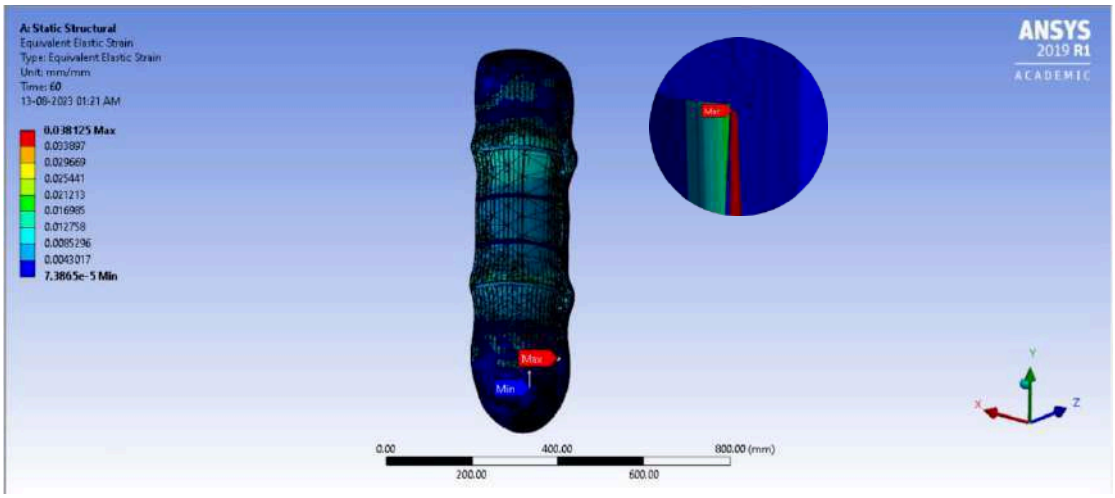

Figure 59: Sectional View of LH2's Equivalent Elastic Strain

5.5 External Fuel Tank of Launch Vehicle

Figure 60 illustrates the total deformation of the External Fuel Tank, while Figure 55 presents a cross-sectional view of the total deformation of the External Fuel Tank. According to the results of the investigation, it was seen that the tank had a maximum distortion of 6.7 mm. However, the model is scaled down by 1:10. So the maximum deformation is 67.602 mm. Figure 49 depicts the precise place

where the highest level of deformation has been generated due to the exerted loads. The potential for significant deformation is noteworthy, given the inherent risk of tank collapse.

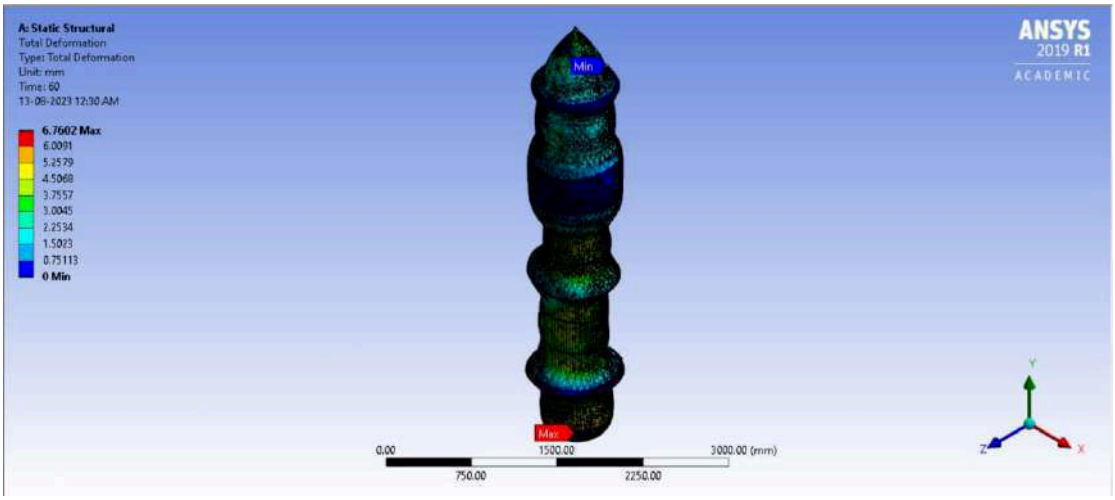

Figure 60: EFT's Total Deformation

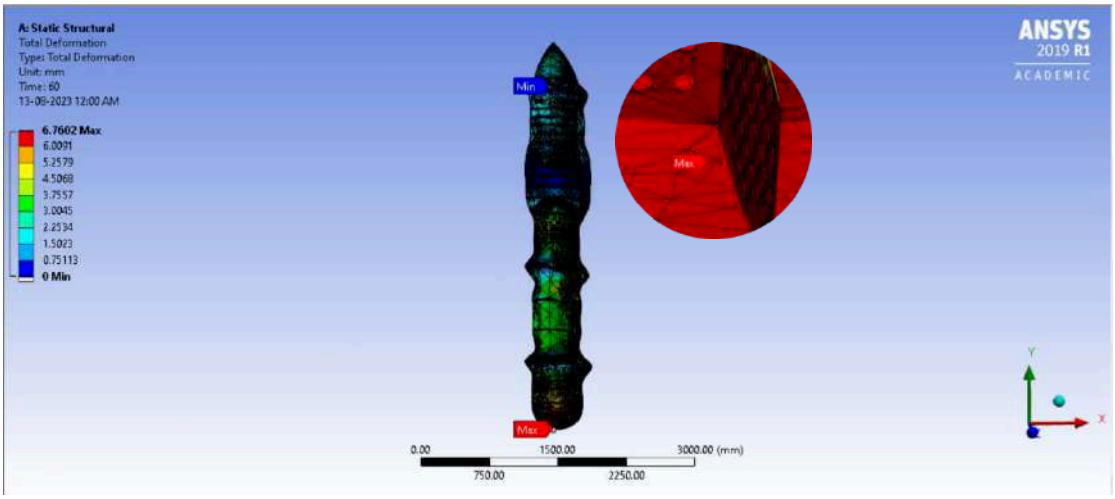

Figure 61: Sectional View of EFT's Total Deformation

Figures 62 and 63 illustrate the equivalent stress encountered by the EF Tank. The experimental study resulted in a maximum stress value of 427130 MPa. The stress levels observed in the tank were mainly within the range of 0.128 MPa to 2000 MPa. However, a few particular spots on the surface of the EF tank revealed much higher stress values, reaching up to 427130 MPa. The tank's structural integrity will be compromised due to exceeding its yield stress limit.

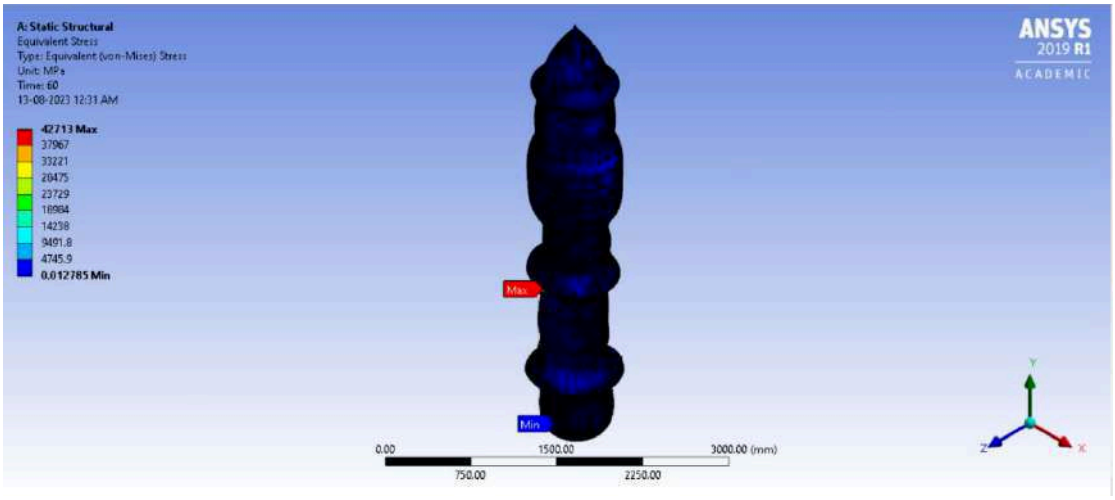

Figure 62: EFT's Equivalent Stress

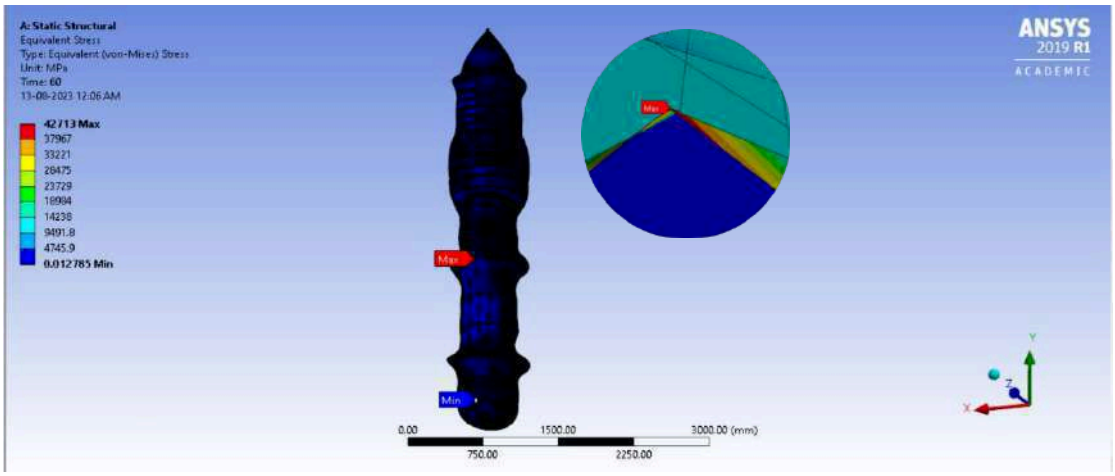

Figure 63: Sectional View of EFT's Equivalent Stress

Figures 64 and 65 show the Equivalent elastic strain of the fuel tank. The maximum strain on the fuel tank is found to be 6.6593.

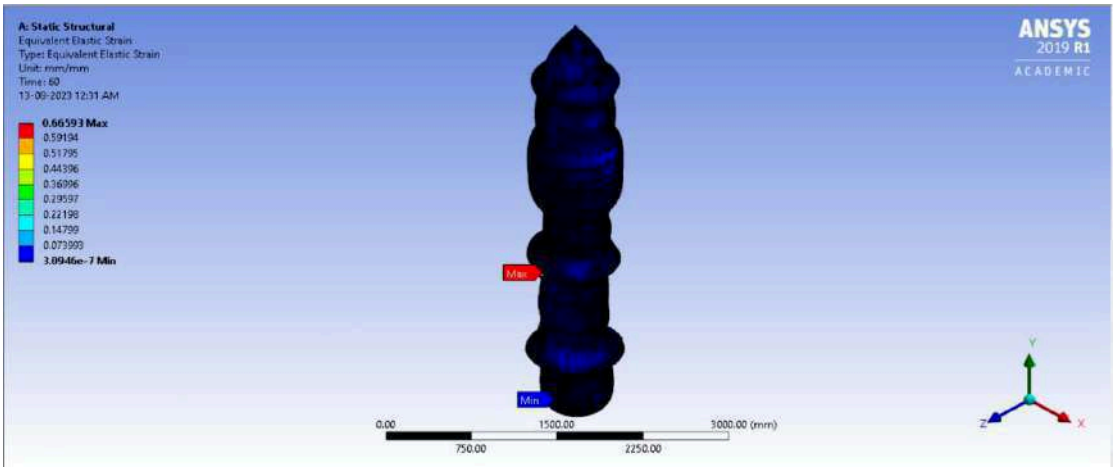

Figure 64: EFT's Equivalent Elastic Strain

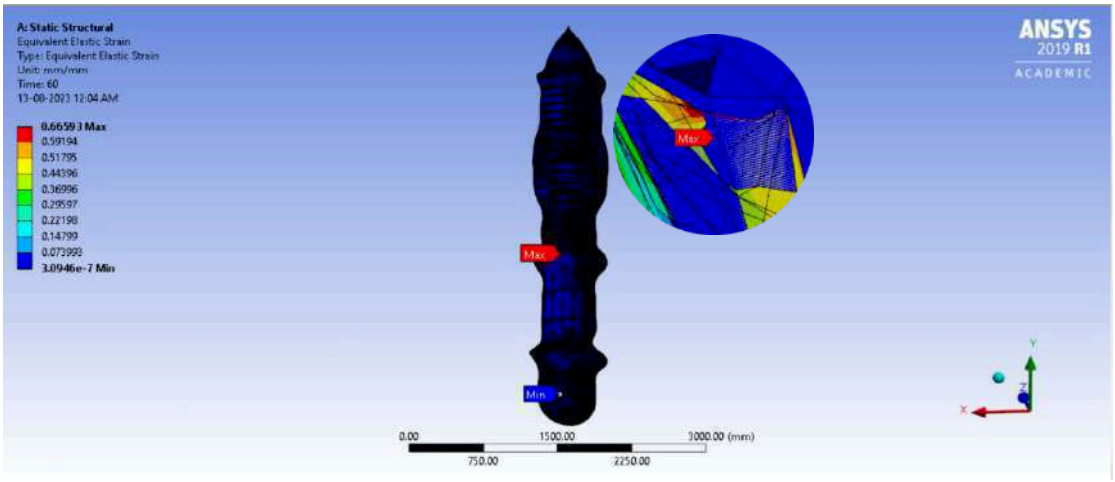

Figure 65: Sectional View of EFT's Equivalent Elastic Strain

VI. CONCLUSION

To summarise, this report presents and discusses the findings of the deformation study conducted on many components of the launch vehicle, including the 500x500x25 mm plate, Liquid Oxygen (LOX) tank, Intertank, Liquid Hydrogen (LH2) tank, and External Fuel Tank (EFT). The study encompassed the assessment of total deformation, equivalent stress, and equivalent elastic strain for every component.

The 500x500x25 mm plate exhibited a maximum measured deformation of 0.00051977 mm, suggesting a relativelylow level of distortion. The magnitude of the stress sustained by the plate was far below the yield strength h of the material. Concerns were raised over probable fatigue due to prolonged usage of the LOX tank since it exhibited a maximum deformation of 12.354 millimetres, a significant value warranting attention. The stress levels hit a crucial threshold beyond the material's yield stress, posing a tank failure risk.

In the case of the Intertank, it was seen that the most significant deformation experienced was measured to be 0.022 mm. The corresponding stress levels were relatively low, indicating a lower likelihood of encountering fatigue-induced problems. The LH2 tank demonstrated a notable maximum distortion of 3.6 mm, which, when extrapolated, amounted to 108 mm. The stress level of 2706.9 MPa is considerable, potentially jeopardising the tank's structural integrity.

A maximum deformation of 67.602 mm was found in the External Fuel Tank (EFT) instance. The stress equivalent exhibited localised regions with very elevated stress levels, potentially jeopardising the tank's integrity.

In general, several elements had minor distortions and stress levels below acceptable thresholds, while others gave rise to apprehension regarding possible fatigue and structural soundness concerns. The findings above underscore the significance of continuous inquiry and assessment to guarantee these components' safety and dependability throughout operating circumstances.

REFERENCES

1. Mohan, Velram Balaji, Kin-tak Lau, David Hui, and Debes Bhattacharyya. 2018. "Graphene-Based Materials and Their Composites: A Review on Production, Applications and Product Limitations." Composites Part B: Engineering 142 (June): 200–220. https://doi.org/10.1016/j.compositesb.2018.01.013

2. Jayaseelan, Joel, Ashwath Pazhani, Anthony Xavior Michael, Jeyapandiarajan Paulchamy, Andre Batako, and Prashantha Kumar Hosamane Guruswamy. 2022. "Characterization Studies on Graphene-Aluminium Nano Composites for Aerospace Launch Vehicle External Fuel Tank Structural Application." Materials 15 (17): 5907. https://doi.org/10.3390/ma15175907
3. "Pin on Space // Free Photos from Nasa." n.d. Pinterest. Accessed September 12, 2023. https://www.pinterest.com/pin/439663982371779097/
4. Samal, Priyaranjan, Pandu R. Vundavilli, Arabinda Meher, and Manas M. Mahapatra. 2020. "Recent Progress in Aluminum Metal Matrix Composites: A Review on Processing, Mechanical and Wear Properties." Journal of Manufacturing Processes 59 (November): 131–52. https://doi.org/10.1016/j.jmapro.2020.09.010
5. Pazhani, Ashwath, M. Venkatraman, M. Anthony Xavior, Arivarasu Moganraj, Andre Batako, Jeyapandiarajan Paulsamy, Joel Jayaseelan, Arivazhagan Anbalagan, and Jayesh Shanthi Bavan. 2023. "Synthesis and Characterisation of Graphene-Reinforced AA 2014 MMC Using Squeeze Casting Method for Lightweight Aerospace Structural Applications." Materials & Design 230 (June): 111990. https://doi.org/10.1016/j.matdes.2023.111990
6. Afifah Md Ali, Mohd Zaidi Omar, Hanizam Hashim, Mohd Shukor Salleh, and Intan Fadhlina Mohamed. 2021. "Recent Development in Graphene-Reinforced Aluminium Matrix Composite: A Review." Reviews on Advanced Materials Science 60 (1): 801–17. https://doi.org/10.1515/rams-2021-0062
7. Iqbal, AKM Asif, Nazmus Sakib, A. K. M. Parvez Iqbal, and Dewan Muhammad Nuruzzaman. 2020. "Graphene-Based Nanocomposites and Their Fabrication, Mechanical Properties and Applications." Materialia 12 (August): 100815. https://doi.org/10.1016/j.mtla.2020.100815
8. Xie, Yuming, Xiangchen Meng, Yuexin Chang, Dongxin Mao, Yuchen Yang, Yanli Xu, Long Wan, and Yongxian Huang. 2022. "Ameliorating Strength-Ductility Efficiency of Graphene Nanoplatelet-Reinforced Aluminum Composites via Deformation-Driven Metallurgy." Composites Science and Technology 219 (March): 109225. https://doi.org/10.1016/j.compscitech.2021.109225
9. Pu, Bowen, Xiang Zhang, Dongdong Zhao, Chunnian He, Chunsheng Shi, Enzuo Liu, Junwei Sha, and Naiqin Zhao. 2021. "Achieving Prominent Strengthening Efficiency of Graphene Nanosheets in Al Matrix Composites by Hybrid Deformation." Carbon 183 (October): 530–45. https://doi.org/10.1016/j.carbon.2021.07.042
10. Hanizam, Hashim, Mohd Shukor Salleh, Mohd Zaidi Omar, and Abu Bakar Sulong. 2019. "Optimisation of Mechanical Stir Casting Parameters for Fabrication of Carbon Nanotubes–Aluminium Alloy Composite through Taguchi Method." Journal of Materials Research and Technology 8 (2): 2223–31. https://doi.org/10.1016/j.jmrt.2019.02.008.
11. Liu, Wanying, Ying Liu, Yuanhua Lin, Zhi Zhang, Shiyu Feng, Mohd Talha, Yufan Shi, and Tao Shi. 2019. "Effects of Graphene on Structure and Corrosion Resistance of Plasma Electrolytic Oxidation Coatings Formed on D16T al Alloy." Applied Surface Science 475 (May): 645–59. https://doi.org/10.1016/j.apsusc.2018.12.233.
12. Jiang, Tao, Tao Jiao, Guoqing Dai, Zhikang Shen, Yanhua Guo, Zhonggang Sun, and Wenya Li. 2022. "Microstructure Evolution and Mechanical Properties of 2060 Al-Li Alloy via Friction Stir Additive Manufacturing" 935 (November): 168019–19. https://doi.org/10.1016/j.jallcom.2022.168019.
13. Taher El-Bitar, Fathei Nouh, Omayma A Elkady, and Hossam M Yehia. 2022. "Impact of Graphene and Hot-Rolling on the Microstructure and Mechanical Properties of Aluminum Matrix Nano-Composite." Research Square, February. https://doi.org/10.21203/rs.3.rs-1258597/v1
14. Nithesh, K., M.C. Gowrishankar, Rajesh Nayak, and Sathyashankara Sharma. 2021. "Effect of Light Weight Reinforcement and Heat Treatment Process Parameters on Morphological and Wear Aspects of Hypoeutectic Al-Si Based Composites - a Critical Review." Journal of Materials Research and Technology 15 (November): 4272–92. https://doi.org/10.1016/j.jmrt.2021.10.019

15. Edward, Kaamil, K A Mamun, Sumesh Narayan, Mansour H Assaf, David Rohindra, & Upaka Rathnayake. (2023). "State-of-The-Art Graphene Synthesis Methods and Environmental Concerns." Applied and Environmental Soil Science 2023 (February): 1–23. https://doi.org/10.1155/2023/8475504.
16. Yadav, Aanchal, R. K. Godara, G. Bhardwaj, R. U. Patil, S. K. Singh, and Kishore Khanna. 2021. "A Review on Fracture Analysis of CNT/Graphene Reinforced Composites for Structural Applications." Archives of Computational Methods in Engineering 29 (1): 545–82. https://doi.org/10.1007/s11831-021-09650-2.
17. [Harichandran, R., R. Vignesh Kumar, and M. Venkateswaran. 2022. "Experimental and Numerical Evaluation of Thermal Conductivity of Graphene Nanoplatelets Reinforced Aluminium Composites Produced by Powder Metallurgy and Hot Extrusion Technique." Journal of Alloys and Compounds 900 (April): 163401. https://doi.org/10.1016/j.jallcom.2021.163401
18. M C, Gowrishankar, Pavan Hiremath, Manjunath Shettar, Sathyashankara Sharma, and Satish Rao U. 2020. "Experimental Validity on the Casting Characteristics of Stir Cast Aluminium Composites." Journal of Materials Research and Technology 9 (3): 3340–47. https://doi.org/10.1016/j.jmrt.2020.01.028.
19. Pérez-Bustamante, R., D. Bolaños-Morales, J. Bonilla-Martínez, I. Estrada-Guel, and R. Martínez-Sánchez. 2014. "Microstructural and Hardness, Behavior of Graphene-Nanoplatelets/Aluminum Composites, Synthesized by Mechanical Alloying." Journal of Alloys and Compounds 615 (December): S578–82. https://doi.org/10.1016/j.jallcom.2014.01.225
20. Yan, Shi-Ping, Shi Dai, X Y Zhang, Chih-Chung Yang, Q Z Hong, J C Chen, and Zhihong Lin. 2014. "Investigating Aluminum Alloy Reinforced by Graphene Nanoflakes." Materials Science and Engineering A-Structural Materials Properties Microstructure and Processing 612 (August): 440–44. https://doi.org/10.1016/j.msea.2014.06.077.
21. Tabandeh-Khorshid, Meysam, J.B. Ferguson, Benjamin F. Schultz, Chang-Soo Kim, Kyu Cho, and Pradeep K. Rohatgi. 2016. "Strengthening Mechanisms of Graphene- and Al2O3-Reinforced Aluminum Nanocomposites Synthesized by Room Temperature Milling." Materials & Design 92 (February): 79–87. https://doi.org/10.1016/j.matdes.2015.12.007.
22. Hassan Ahmed Hassan, Ahmed, and Naci Kurgan. 2019. "Modeling and Buckling Analysis of Rectangular Plates in ANSYS." International Journal of Engineering & Applied Sciences 11 (1): 310–29. https://doi.org/10.24107/ijeas.531011.
23. Rajendran, S, and D Song. 1998. "Finite Element Modelling of Delamination Buckling of Composite Panel Using ANSYS." https://citeseerx.ist.psu.edu/document?repid=rep1&type=pdf&doi=4387b147786c9d1b59dedd3b2d7e99da2d9ef695
24. Gomez, Arturo, and Howard Smith. 2019. "Liquid Hydrogen Fuel Tanks for Commercial Aviation: Structural Sizing and Stress Analysis." Aerospace Science and Technology 95 (December). https://doi.org/10.1016/j.ast.2019.105438
25. Nemeth, Michael, Vicki Britt, Timothy Collins, and James Starnes. 1996. "NASA Nonlinear Analysis of the Space Shuttle Superlightweight External Fuel Tank." https://ntrs.nasa.gov/api/citations/19970010449/downloads/19970010449.pdf
26. Chiesa, Sergio, Marco Di Sciuva, and Luca Testore. 1999. "Launch Vehicles Conceptual Design and Structural Analysis: An Integrated Approach via FEM." Aircraft Design 2 (3): 117–45. https://doi.org/10.1016/s1369-8869(99)00011-7
27. Kumar, KS. 2015. "Heat Transfer Analysis of Light Weight Cryogenic Tank for Space Vehicles." Indian Journal of Science and Technology, February. https://doi.org/10.17485/ijst/2015/v8i4/62291
28. "External Tank | Encyclopedia.com." n.d. Www.encyclopedia.com. Accessed September 12, 2023. https://www.encyclopedia.com/science/news-wires-white-papers-and-books/external- tank

29. Review of FACT SHEET SPACE SHUTTLE EXTERNAL TANK. 2008. New Orleans, LA: Lockheed Martin Space Systems Company. http://www.nasa-klass.com/Curriculum/Get_Training%201/ET/RDG_ET-Additional/ETFactSheet.pdf
30. Nayan, Niraj, Nilesh P. Gurao, S.V.S. Narayana Murty, Abhay K. Jha, Bhanu Pant, S.C. Sharma, and Koshy M. George. 2015. "Microstructure and Micro-Texture Evolution during Large Strain Deformation of an Aluminium–Copper–Lithium Alloy AA 2195." Materials & Design (1980-2015) 65 (January): 862–68. https://doi.org/10.1016/j.matdes.2014.09.037
31. Dursun, Tolga, and Costas Soutis. 2014. "Recent Developments in Advanced Aircraft Aluminium Alloys." Materials & Design (1980-2015) 56 (April): 862–71. https://doi.org/10.1016/j.matdes.2013.12.002
32. Rao, Venkateswara, W Yu, and Robert O Ritchie. 1989. "Cryogenic Toughness of Commercial Aluminum-Lithium Alloys: Role of Delamination Toughening." Metallurgical Transactions 20 (3): 485–97. https://doi.org/10.1007/bf02653929
33. Thomas, T. Y. 1955. "COMBINED ELASTIC and von MISES STRESS-STRAIN RELATIONS." Proceedings of the National Academy of Sciences of the United States of America 41 (11): 908–10. https://doi.org/10.1073/pnas.41.11.908
34. Wodo, Olga, and Baskar Ganapathysubramanian. 2011. "Computationally Efficient Solution to the Cahn–Hilliard Equation: Adaptive Implicit Time Schemes, Mesh Sensitivity Analysis and the 3D Isoperimetric Problem." Journal of Computational Physics 230 (15): 6037–60. https://doi.org/10.1016/j.jcp.2011.04.012
35. "What Are the Best Conditions for Launching Model Rockets?" n.d. Accessed September 11, 2023. https://www.acsupplyco.com/what-are-the-best-conditions-for-launching-model-rockets
36. "Annual Average Weather for Cornwall, United Kingdom." n.d. BeachWeather. Accessed September 11, 2023. https://beach-weather.com/Northern-Europe/United-Kingdom/England/Cornwall/averages/#:~:text=The%20most%20windy%20month%20in
37. "NASA - Amazing Facts: Space Shuttle External Tank." n.d. https://www.nasa.gov/centers/marshall/about/star/et_11.html
38. "Liquid Oxygen." 2023. Wikipedia. August 11, 2023. https://en.wikipedia.org/wiki/Liquid_oxygen#cite_note-2
39. "NASA - the External Tank." 2019. Nasa.gov. 2019. https://www.nasa.gov/returntoflight/system/system_ET.html
40. "Liquid Hydrogen." 2020. Wikipedia. April 27, 2020. https://en.wikipedia.org/wiki/Liquid_hydrogen

This page is intentionally left blank

The Solution of the 3 Dimensional Navier-Stokes Momentum Equations (A 3 Dimensional Integral Equation Approach)

Andrés Boldori & Dr. A. D. Barbour

University of Zurich

ABSTRACT

This paper provides the solution of the classical navier stokes mo mentum equations within the common three dimensional and euclidean space. The ”function variable” of the equations, w:= (p, v) taking values in R^4, con sists of a skalar field ”pressure” p and a vector field ”velocity” v, where both, p and v depend on the same four variables (x, y, z, t) (space and time). Moreover, the solution space $L \subset \{(v, p) =: w \in C(R^4, R^4)$ (the continuous differentiable functions from $R^4$to R^4) $v \in C^2(R^4, R^3)$ (the twice continuous differentiable functions from $R^4$to R^3) }. The navier-stokes equation system, as we will show, is underspecified in the sense that infinitly many and ”arbitrary” solutions exist. We will show smoothness and existence of the general solution of the navier stokes equations. We deal with fluid dynamics and their boundary conditions within the incompressible and the compressible (the general) case.

Keywords: Claude-Luis Navier and George Gabriel Stokes; Navier-Stokes equations; 3- dimensional Navier-Stokes equations; Fluid dynamics; Compressible and incompressible fluids; Differential geometry and analysis.

Classification: DDC Code: QA377

Language: English

Great Britain Journals Press

LJP Copyright ID: 392955
Print ISSN: 2631-8474
Online ISSN: 2631-8482

London Journal of Engineering Research

Volume 24 | Issue 7 | Compilation 1.0

The Solution of the 3 Dimensional Navier-Stokes Momentum Equations (A 3 Dimensional Integral Equation Approach)

André́s Boldori[α] & Dr. A. D. Barbour[σ]

ABSTRACT

This paper provides the solution of the classical navier stokes mo mentum equations within the common three dimensional and euclidean space. The "function variable" of the equations, w := (p, v) taking values in R^4, con sists of a skalar field "pressure" p and a vector field "velocity" v, where both, p and v depend on the same four variables (x, y, z, t) (space and time). Moreover, the solution space L $\subset$ {(v, p) =: w $\in$ C(R^4, R^4) (the continuous differentiable functions from $R^4$to R^4) v $\in$ C^2(R^4, R^3) (the twice continuous differentiable functions from $R^4$to R^3) }. The navier-stokes equation system, as we will show, is underspecified in the sense that infinitly many and "arbitrary" solutions exist. We will show smoothness and existence of the general solution of the navier stokes equations. We deal with fluid dynamics and their boundary conditions within the incompressible and the compressible (the general) case.

Keywords: Claude-Luis Navier and George Gabriel Stokes; Navier-Stokes equations; 3- dimensional Navier-Stokes equations; Fluid dynamics; Compressible and incompressible fluids; Differential geometry and analysis.

Author α: Departement of Mathematics, University of Z¨urich. e-mail: a.d.barbour@math.uzh.ch
σ: Departement of Mathematics, University of Z¨urich. e-mail:boldori084@gmail.com

I. INTRODUCTION

The general form of the well known navier stokes (momentum) equations (compare to [6]) in three dimensions for compressible fluids in space and time reads as follows:

$$\rho\left(\frac{\partial \vec{v}}{\partial t} + (\vec{v}\cdot\nabla)\vec{v}\right) = -\nabla p + \mu\Delta\vec{v} + (\lambda+\mu)\nabla(\nabla\cdot\vec{v}) + \vec{f} \qquad (1)$$

where its elements are:

- The laplace operator Δ
- The gradient operator ∇
- The parameters of the equation: the "Volume-force" density vector field $\vec{f} : R^3 \to R$ (in Newton/m^3), the viscosity $(\lambda+\mu)$ and the density of the viscosity ρ. We denote the set of function pairs $w = (p, v)$ for which the navier stokes equation system holds by L.

We will show that the four dimensional solution field of this system of differential equations is underspecified and possesses a solution for almost any arbitrary $v \in C^2(\mathbb{R}^4, \mathbb{R}^3)$, the twice differentiable functions from $\mathbb{R}^4$ to $\mathbb{R}^3$. A comparison to the well known transport equation from which the navier stokes equation system is constructed of, or maybe to the known laplace and poisson

equations which are already solved (explicitly in three dimensions, see [7]) or certainly to the one and two dimensional navier stokes equations systems leads unfortunately not to new methods for solving our equations. Those will certainly not be solvable without any notion of lebesgue integration. We will therefore try to invert the (functional) operators within the compressible momentum equations as still, a good notion of understanding is provided by using the three dimensional lebesgue integral (since the "household" of the chemical entropy of the equations must be fullfilled at each point in time within incompressible fluid dynamics). As well one could compare to the case of the stochastic navier stokes equations in one, two or three dimensions (see [2] and [5]). Moreover and specifically, to any two or three dimensional stochastic partial differential equation using a probabilistic measure, the set of Lebesgue integration zerosets in three (space) or four (space and time) dimensions does differ in general from the set of probabilistic zerosets of the probability measure of the stochastic integration which is used to construct the stochastic equations and which gives the probability densities of the possible and probable solution paths of the equations. (see literature of the theory of stochastic integration, stochastic differential/integral equations (SDE) and stochastic partial differential equations in more than one dimension (SPDE)). Indeed, our experience shows that the methods obtained from the mentioned related equations are not directly relevant to the three dimensional case (see also [4]). In this work, we show smoothness and existence of the solution of the navier stokes equations in three dimensions, (even though the time variable makes it a four dimensional equation) as required internationally from the CMI in Oxford and provide it in the form of the largest set of functions solving the equations, depending on the given parameters $(\vec{f}, \rho, \lambda+\mu)$. As a well known and so called "millenium riddle" (see also [8], Andrés Boldori, 2024, as well as [3]), its solution is also expected to be humanistic! But must we necessarily deal with fluid dynamics if we want to solve the 3-dimensional navier stokes equations from above? And if we do, does the solution of the general case, within compressible fluid dynamics, differ from the solution of the particular incompressible case? The ideas of this chapter do in any case not replace any mathematical proof.

II. NECESSARY SMOOTHNESS CONDITIONS OF A SOLUTION PATH (VECTOR FIELD) OF THE 3 DIMENSIONAL COM PRESSIBLE NAVIER STOKES MOMENTUM EQUATIONS.

2.1 Particular Special Cases of the Navier Stokes Equations

(see also: [1]) The navier stokes equations are by far not just an "artificial" system of equations having no meaning, but exist within many specified contexts of real nature environnements. They arise from physical laws and can be combined with other equations. One could observe that it is not possible to fail the navier stokes equations without failing any physical law in addition. As a mathematical equation, at least the following four particular special cases must be taken into account:

1. $v \equiv 0$ (identical) and $p \equiv 0$ fullfills the equations if and only if $f \equiv 0$.
2. $v \equiv 0$ fullfills the equations for: $p(x,y,z,t) = -\int_{-\infty}^{x} f_1(x_0,y,z,t)dx_0 + \int_{-\infty}^{y}(-f_2(x,y_0,z,t))dy_0 - \int_{-\infty}^{x}(d(\int_{-\infty}^{y}(-f_2(x_0,y_0,z,t))dy_0)/dx_0)dx_0 + \int_{-\infty}^{z}(-f_3(x,y,z_0,t))dz_0 - \int_{-\infty}^{x}(d(\int_{-\infty}^{z}(-f_3(x_0,y,z_0,t))dz_0)/dx_0)dx_0 + c(t)$ by "inserting" since of $-\vec{f} = \nabla p$. (Notice that the expression of p is no solution if we take indefinite integrals since of possibly differing integration constants)

3. The mathematical and overall theoretical case of :
$\frac{1}{\rho}\int_0^t f(x,y,z,t_0)dt_0 = v(x,y,z,t)$ with $f(t) = \partial v(x,y,z,t)/\partial t = 0$, outside a finite nonemp-ty domain D (usually the volume of a viscosity). This case must be solved like the ordinary compressible momentum navier stokes equations. Then, inside D :

$$\rho\left((\vec{v}\cdot\nabla)\vec{v}\right) = -\nabla p + \mu\Delta\vec{v} + (\lambda+\mu)\nabla(\nabla\cdot\vec{v})$$

4. In this case, in addition to the momentum equations, newtons second law is holding: $F = m\cdot a(x,y,z,t) = m\cdot\partial v(x,y,z,t)/\partial t$. And the external force field f as a parameter of the equations is a part of the overall force field F. See sections 3.2 and 3.3 for compressible and incompressible fluid dynamics of the momentum equations and their solutions.

2.2 A Solution of the Navier Stokes Equation for Which V is Not in $C^3(R^4, R^3)$

Taking "cm" and "s" (second) as "standard" units during the following theoretical experiment, a vertical pipe of diameter $d = 5$, length $l = 1000$ and the z-axis as main axis within a standard coordinate system (3-dimensional euclidean space), starting at $z = 950$ and ending at $z = -50$ which possesses a "bottom" of plastic or gum, is filled with water and contains a "wedge" of shape and location so that the water flow velocity v along it takes the form $v(x,y,z,t) = (0, v_2, v_3)(x,y,z,t)$:

$v_2(z) := z^3$ and $v_3^2 = \left|v(x,y,z,t)\right|^2 - z^6$, $0 < y < 1$, $-0.1 \le x \le 0.1$
$v_2(z) := -z^3$ and $v_3^2 = \left|v(x,y,z,t)\right|^2 - z^6, -1 \le y < 0$, $-0.1 \le x \le 0.1$

with v having a constant lenght along the wedge. $v_2(z)$ as a function of z is not 3 times differentiable at the edge of the wedge $(0,0,0,t)$. Neglecting the friction of the wedge and the water flowing out the pipe if opening its bottom, a velocity field is created by the acceleration (gravity) of the water within the pipe obtaining a constant velocity after the initial acceleration. The acceleration of the water within can as well be used to create a constant velocity along the wedge: The hight $h(t)$ of the water level within the pipe while opening its bottom in the form of a hole of variable diameter $d_0(t)$ is:

$$h(t) = (V_{pipe} \text{ - } Volume_{out}(t))/d = (V_{pipe} \text{ - } \sqrt{2g\cdot h(t)}\cdot Area_{hole}(d_0(t)))/d$$

$$h(t) = ((\sqrt{2g}/d)\cdot Area_{hole}(d_0(t)) - \sqrt{((\sqrt{2g}/d)\cdot Area_{hole}(d_0(t)))^2 - 4\cdot V_{pipe}/d})/(-2)$$

$$Area_{hole}(d_0(t)) = (d\cdot h(t) - V_{pipe})/\sqrt{2g\cdot h(t)}$$

III. EXISTENCE OF A SOLUTION OF THE 3 DIMENSIONAL NAVIER STOKES MOMENTUM EQUATION

3.1 Boundary Conditions

The system of compressible navier stokes equations is a differential equation in the variable p, which is easily solvable as soon as v is given. Even though the compressible navier stokes momentum equation (system) differs (slightly) from the imcompressible one, our attempt here to solve the equations does not include any of the classical initial value problems of differential equations. Not mathematically, but from physics, the theory of the navier stokes equations may be connected to the theory of fluid dynamics.

3.2 Compressible Fluid Dynamics

The momentum equation in three dimensions (equation (1)) can be written as follows:

$$-\rho\left(\frac{\partial\vec{v}}{\partial t}+(\vec{v}\cdot\nabla)\vec{v}\right)+\mu\Delta\vec{v}+(\lambda+\mu)\nabla(\nabla\cdot\vec{v})+\vec{f}=\nabla p \quad (=\vec{grad}(p)) \tag{2}$$

where the equation:

$$\vec{grad}(p)=\vec{f} \tag{3}$$

can easily be solved since of:

$$p=c(y,z,t)+\int f_1dx=c(x,z,t)+\int f_2dy=c(x,y,t)+\int f_3dz \tag{4}$$

and the expression of section 2.1 (particular special case 2.) follows by setting $\vec{f}:=-\vec{f}$ within equation (3). If we went a step further ahead and now replaced $-\vec{f}$ from the expression of the particular special case of section 2.1 again by $-\vec{f}_{new}:=\vec{g}:=-\rho\left(\frac{\partial\vec{v}}{\partial t}+(\vec{v}\cdot\nabla)\vec{v}\right)+\mu\Delta\vec{v}+(\lambda+\mu)\nabla(\nabla\cdot\vec{v})+\vec{f}$, we'd get an expression for p:

$p(x,y,z,t)=\int_{-\infty}^{x}g_1(x_0,y,z,t)dx_0+\int_{-\infty}^{y}(g_2(x,y_0,z,t))dy_0-$
$\int_{-\infty}^{x}(d(\int_{-\infty}^{y}(g_2(x_0,y_0,z,t))dy_0)/dx_0)dx_0+\int_{-\infty}^{z}(g_3(x,y,z_0,t))dz_0$
$-\int_{-\infty}^{x}(d(\int_{-\infty}^{z}(g_3(x_0,y,z_0,t))dz_0)/dx_0)dx_0+c(t)$

The solution space L for the navier stokes equations with the definition of $\vec{g}$ from above, is:

$L:=\{\big(v(x,y,z,t),\int_{-\infty}^{x}g_1(x_0,y,z,t)dx_0+\int_{-\infty}^{y}(g_2(x,y_0,z,t))dy_0-$
$\int_{-\infty}^{x}(d(\int_{-\infty}^{y}(g_2(x_0,y_0,z,t))dy_0)/dx_0)dx_0+\int_{-\infty}^{z}(g_3(x,y,z_0,t))dz_0$
$-\int_{-\infty}^{x}(d(\int_{-\infty}^{z}(g_3(x_0,y,z_0,t))dz_0)/dx_0)dx_0+c(t)\big)\mid$ The second component of the pair does exist and $c(t):\mathbb{R}_{\geq 0}\to\mathbb{R}\}$

The arbitrary shift $c(t)$ applies to the entire vector field (to any v which is "integrable enough", the expression within the solution set is a solution of the three dimensional navier stokes momentum equation, for any arbitrary $c(t):\mathbb{R}_{\geq 0}\to\mathbb{R}$). The domain of definition of the velocity vector field v should not be the empty set.

3.3 Incompressible Fluid Dynamics

A Fluid in physics is said to be incompressible if its velocity vector field $v(x,y,z,t)$has zero divergence everywhere in the sense of differential geometry: $div(v)\equiv 0$. The solution space of the incompressible navier stokes momentum equations must simply be restricted to functions and vector fields having divergence zero everywhere:

$L_{incompressible}:=\{\big(v(x,y,z,t),\int_{-\infty}^{x}g_1(x_0,y,z,t)dx_0+\int_{-\infty}^{y}(g_2(x,y_0,z,t))dy_0-$
$\int_{-\infty}^{x}(d(\int_{-\infty}^{y}(g_2(x_0,y_0,z,t))dy_0)/dx_0)dx_0+\int_{-\infty}^{z}(g_3(x,y,z_0,t))dz_0$
$-\int_{-\infty}^{x}(d(\int_{-\infty}^{z}(g_3(x_0,y,z_0,t))dz_0)/dx_0)dx_0+c(t)\big)\mid$ The second component of the pair does exist, $c(t):\mathbb{R}_{\geq 0}\to\mathbb{R}$ and $div(v)\equiv 0\}$

again by setting $\vec{g}$:

$$\vec{g} :\equiv -\rho\left(\frac{\partial \vec{v}}{\partial t} + (\vec{v}\cdot\nabla)\vec{v}\right) + \mu\Delta\vec{v} + (\lambda+\mu)\nabla(\nabla\cdot\vec{v}) + \vec{f}$$

3.4 Conclusion

For now we have shown smoothness and existence for the compressible and incompressible navier stokes momentum equation system in three dimensions.

REFERENCES

1. Skript zur Vorlesung: Die Navier-Stokes-Gleichungen fur kompressible Flüssigkeiten, Aachen De Prof. Dr. J. Lorenz, Dipl.Math. V. Reichelt, Institut für Geometrie und Praktische Mathematik, 1994.
2. Stochastic Navier-Stokes Equations and Related Models, Luigi Amedeo Byianchi and Franco Flandoli, Cornell University, 2020.
3. Navier Stokes Equations, An Introduction with Applications, Grzegorz Lukaszewicz , Piotr Kalita, Springer Editorial, 2016.
4. A Student's Guide to the Navier-Stokes Equations, Justin W. Garvin, University of Iowa, Cambridge university press, https://doi.org/10.1017/9781009236119, 2023.
5. Navier-Stokes equations in one and two dimensions, Jon Nerdal, Louisiana State University and Agricultural and Mechanical College, LSU Scholarly Repository, LSU Masters Theses Graduate School, 2022.
6. Existence and smoothness of the navier-stokes equation, Charles L. Feffer man, CMI Oxford, 2022.
7. Elektromagnetics I, Steven W. Ellingson, LibreTexts Engineering, Virginia Tech Libraries' Open Education Initiative, 2024.
8. p /= np: The Set of Deterministic Problems that are Solvable in Polynomial Time is Unequal to the Set of Non-Deterministic Problems that are Solv able in Polynomial Time, Andr´es Boldori, Science publications, Journal of computer science, open access, 2024.